HABILITATION THESIS

Temperature and atmosphere influence during combustion synthesis of metal oxide (nano)powders

IANOȘ Robert Gabriel

Politehnica University of Timișoara
Faculty of Industrial Chemistry and Environmental Engineering

2015

Table of content

1. Rezumat

Teza de abilitare cu titlul "*Influența temperaturii și atmosferei asupra sintezei (nano)pulberilor oxidice prin metoda combustiei*" prezintă în mod sintetic cele mai importante rezultate științifice publicate de candidat după obținerea titlului științific de Doctor, în anul 2008. Din punct de vedere al domeniul abordat, activitatea științifică a candidatului este preponderent centrată pe sinteza (nano)pulberilor oxidice prin metoda combustiei.

Prin soluțiile inovative de a regla temperatura și atmosfera din timpul reacțiilor de combustie dar și de a îndepărta carbonul rezidual prin tratare cu apă oxigenată, H_2O_2, candidatul a deschis noi perspective în sinteza (nano)pulberilor oxidice prin metoda combustiei. Fezabilitatea și eficiența soluțiilor propuse, prezentate în această teză de abilitare, au fost recunoscute și validate de comunitatea științifică internațională, rezultatele obținute fiind publicate în reviste cotate ISI de prestigiu.

Superioritatea soluțiilor propuse de candidat a permis obținerea prin metoda combustiei a unei game variate de materiale, de tipul oxizi metalici, compuși oxidici, soluții solide oxidice și chiar materiale compozite: γ-Fe_2O_3 (maghemit), Fe_3O_4 (magnetit), $LaAlO_3$ (aluminat de lantan), $CaZrO_3$ (zirconat de calciu), $ZnAl_2O_4$ (aluminat de zinc), $CoFe_2O_4$ (ferită de cobalt), $BaAl_2O_4$: Eu^{2+}, Dy^{3+} (aluminat de bariu dopat cu europiu și dysprosiu), Fe_3O_4/C (compozite de tip magnetit/carbon).

Spre deosebire de multe alte metode de sinteză, în care obținerea compusului cristalin dorit presupune în mod obligatoriu cel puțin o etapă de calcinare, metoda combustiei prezintă o serie de avantaje: nu necesită calcinare, este rapidă, este eficientă din punct de vedere energetic, și nu în ultimul rând este ecologică. Un atuu suplimentar este reprezentat de faptul că, caracteristicile pulberilor (suprafață specifică, dimensiunea cristalitelor și dimensiunea granulelor) preparate prin metoda combustiei pot fi ajustate în mod corespunzător prin schimbarea condițiilor de sinteză.

Din acest punct de vedere, candidatul semnalează faptul că cei mai importanți parametrii și anume temperatura (mai ridicată sau mai scăzută) și atmosfera (oxidantă sau reducătoare) din timpul reacțiilor exoterme de combustie pot fi controlați, ceea ce este de o importanță decisivă mai ales în cazul oxizilor metalici care conțin cationi ce pot adopta mai multe cifre de oxidare.

Rolul major al temperaturii dezvoltate în timpul reacției de combustie este discutat în cazul obținerii pulberilor de $LaAlO_3$, $CaZrO_3$, $ZnAl_2O_4$ și $CoFe_2O_4$. O temperatură de combustie prea ridicată determină creșterea exagerată a dimensiunii particulelor și scăderea suprafeței specifice. Prin urmare, reducerea controlată a temperaturii – apreciată indirect, prin prisma caracteristicilor pulberilor rezultate – reprezintă una din direcțiile de cercetare abordate de candidat. Modul în care se poate realiza această reducere a temperaturii este corelat cu natura compusului țintă. De exemplu în cazul $ZnAl_2O_4$ și $CoFe_2O_4$ înlocuirea azotatului de zinc cu acetat de zinc, respectiv a azotatului de cobalt cu acetat de cobalt contribuie semnificativ la diminuarea temperaturii de combustie, reflectată atât de creșterea suprafeței specifice a pulberilor rezultate cât și de scăderea dimensiunii cristalitelor. Introducerea unor adaosuri suplimentare poate fi de asemenea o modalitate de a reduce exotermicitatea reacțiilor de combustie, care uneori este mult prea ridicată. În funcție de comportarea acestor adaosuri în timpul reacțiilor de combustie, ele pot fi active sau pasive. Adaosurile active participă la procesele de combustie și se consumă în timpul reacției (Ex. $H_2C_2O_4$). Pe de altă parte, adaosurile pasive sunt inerte (Ex. NaCl), nu participă la procesele de combustie și în consecință

se regăsesc la final în amestec cu produsul dorit. În această situație, separarea celor două componenți se poate realiza prin spălare, mizând pe solubilitatea ridicată a NaCl.

Importanța desfășurării reacțiilor de combustie într-o atmosferă reducătoare este una majoră în cazul pulberilor de Fe_3O_4 și $BaAl_2O_4$: Eu^{2+}, Dy^{3+}. Aceste două cazuri, prezentate în detaliu, necesită însă abordări esențial diferite prin prisma temperaturii necesare dezvoltării structurii cristaline dorite. Dacă în cazul magnetitului, Fe_3O_4, este necesară o temperatură de combustie relativ mică, pentru a menține dimensiunea particulelor în domeniul nanometric, în cazul aluminatului de bariu dopat cu europiu dysprosiu, $BaAl_2O_4$: Eu^{2+}, Dy^{3+}, este necesară o temperatură cât mai ridicată, pentru a îmbunătăți proprietățile optice ale luminoforilor respectivi.

În partea finală a secțiunii principale este prezentată o soluție eficientă de îndepărtare a impurităților de carbon din probele de $ZnAl_2O_4$ sau γ-Fe_2O_3 obținute prin metoda combustiei, și anume oxidarea chimică cu apă oxigenată, H_2O_2. Sunt prezentate în antiteză consecințele oxidării chimice cu H_2O_2 comparativ cu oxidarea termică bazată pe calcinare. Din punct de vedere al influenței modalității de eliminare a carbonului rezidual asupra caracteristicilor principale ale pulberilor de $ZnAl_2O_4$ și γ-Fe_2O_3 adică dimensiunea particulelor și suprafața specifică, îndepărtarea carbonului rezidual prin tratare cu apă oxigenată este o tehnică superioară calcinării tradiționale.

În partea finală a tezei sunt prezentate planul de evoluție și dezvoltare a carierei, respectiv principalele direcții de cercetare viitoare.

1. Abstract

The habilitation thesis titled "*Temperature and atmosphere influence during combustion synthesis of metal oxide (nano)powders*" summarizes the most important scientific achievements published by the candidate after defending his PhD thesis in 2008. The research activity conducted by the candidate is mainly focused on the preparation of metal oxide (nano)powders via solution combustion synthesis.

Within this research field, the candidate has opened new perspectives by suggesting a number of innovative solutions to adjust and control the temperature and the atmosphere during combustion reactions, but also to remove the residual carbon by hydrogen peroxide, H_2O_2, treatment. The feasibility and the efficiency of these approaches, presented in this habilitation thesis, have been recognized and validated by the international scientific community, as the obtained results have been published in prestigious ISI-ranked journals.

The superiority of the solutions suggested by the candidate enabled the combustion synthesis of a wide variety of materials, such as metal oxides, oxide compounds, oxide solid solutions and even composite materials: γ-Fe_2O_3 (maghemite), Fe_3O_4 (magnetite), $LaAlO_3$ (lanthanum aluminate), $CaZrO_3$ (calcium zirconate), $ZnAl_2O_4$ (zinc aluminate), $CoFe_2O_4$ (cobalt ferrite), $BaAl_2O_4$: Eu^{2+}, Dy^{3+} (barium aluminate doped with europium and dysprosium), Fe_3O_4/C (magnetite/carbon composites).

Unlike many of the synthesis methods, which require an annealing step in order to obtain the desired crystalline compound, combustion synthesis has several advantages: it doesn't require annealing, is time and energy efficient, and last but not least is environmentally friendly. An additional advantage is that powder characteristics (surface area, crystallite size and grain size) prepared by combustion synthesis can be properly adjusted by changing the synthesis conditions.

From this point of view, the candidate points out that the most important parameters, namely temperature (higher or lower) and atmosphere (oxidizing or reducing) during the exothermic combustion reactions can be controlled, which is of vital importance especially in the case of metal oxides containing cations which may adopt several numbers of oxidation.

The major role of temperature developed during the combustion reaction is discussed in the case of $LaAlO_3$, $CaZrO_3$, $ZnAl_2O_4$ and $CoFe_2O_4$ powder preparation. An exceedingly high combustion temperature causes a significant growth of the particle size and the decrease of specific surface area. Therefore, the controlled decrease of the temperature – which is indirectly estimated, based on the resulting powder characteristics point of view – is one of the research directions approached by the candidate. The solution adopted for this temperature decrease is related to the nature of the target compound. For instance, in the case of $ZnAl_2O_4$ and $CoFe_2O_4$ replacing zinc nitrate by zinc acetate, and cobalt nitrate by cobalt acetate respectively, significantly decreases the combustion temperature, as reflected by the increase of the specific surface area of the resulted powders as well as by the decrease of crystallite size. The addition of various supplementary additives can also be a way to decrease the exothermicity of combustion reactions, which sometimes is too high. Depending on the behavior of these additions during combustion reactions, they can be active or passive. Active additions partake the combustion processes and are consumed during the reaction (Ex. $H_2C_2O_4$). On the other hand, passive additions are inert (Ex. NaCl), do not involve in the combustion processes and therefore are found mixed with the final desired product. In this situation, the separation of the two components can be achieved by washing, counting on the high solubility of NaCl.

The importance of carrying out combustion reactions under reducing atmosphere is a major key in the case of Fe_3O_4 and $BaAl_2O_4$: Eu^{2+}, Dy^{3+} powders. Yet, in terms of the temperature needed for the development of the desired crystalline structure, these two cases, presented in detail, require essentially different approaches. If in the case of magnetite, Fe_3O_4, a relatively low combustion temperature is required, in order to preserve the particle size in the nanometer range, in the case of europium and dysprosium-doped barium aluminate, $BaAl_2O_4$: Eu^{2+}, Dy^{3+}, the temperature should be as high as possible to improve the optical properties of the respective phosphors.

The final part of the main section presents an efficient solution to remove the carbon impurities from $ZnAl_2O_4$ or γ-Fe_2O_3 samples prepared by combustion synthesis, namely chemical oxidation with hydrogen peroxide, H_2O_2. The consequences of the chemical oxidation with H_2O_2 are discussed in contrast with the thermal oxidation based on annealing. From the point of view of the influence of the procedure followed for residual carbon elimination on the main characteristics of $ZnAl_2O_4$ and γ-Fe_2O_3 powders, namely particle size and specific surface area, the removal of the residual carbon by hydrogen peroxide treatment is a superior technique to the conventional annealing.

At the end of the thesis the carrier evolution and the development plan are presented, as well as the main research directions for the future.

2. Scientific – professional achievements. Carrier evolution and development plan

2.1. Main scientific, professional and academic achievements

The most important scientific achievements of the candidate, after defending his PhD thesis (MECTS order no. 5837 of 04.11.2008) are related to the preparation of metal oxide (nano)powders with adjustable properties using one of the most spectacular synthesis methods namely solution combustion synthesis, discovered in 1988 in India by Kashinath C. Patil [1-3].

In principle, this synthesis method exploits the energy resulting from the self-propagating highly exothermic redox reaction that occurs during heating metal nitrates (oxidizers) and various organic compounds or fuels (reducing agents). The ignition of the combustion reaction is achieved by rapidly heating the mixture of raw materials at relatively low temperatures, usually below 500 °C [4-6].

At the same time, when synthesis conditions are properly selected, the temperature reached in the reaction system (1500 °C) is high enough to facilitate the formation of the desired compound without any other heat treatment. It should be noted that the whole process takes a few seconds only and the reaction byproducts (N_2, H_2O, CO_2) are compatible with the environment. All these remarkable advantages determined material scientists to use more and more frequently combustion synthesis for the preparation of a wide range of materials [1-22].

However, there are many cases reported in the literature, in which the advantages of the combustion synthesis are not fully exploited due to the use of template recipes that are not designed according to the desired product and targeted specifications. Therefore a better understanding and control of the combustion reaction parameters, such as temperature and atmosphere, is mandatory. In this context the candidate and his coworkers developed three major research directions, which address the difficulties concerning the influence and the control of temperature, atmosphere and the presence of undesirable organic residues (carbon):

- **Temperature control during combustion reactions**: the synthesis of mixed metal oxides or oxide solid solutions is carried out at different temperatures, depending on the desired compound. Therefore, the maximum actual temperature reached during the combustion reaction (known as the *combustion temperature*) and the energy supplied by the exothermic reaction must ensure the occurrence of the solid state reactions required for the formation of the desired compound. Sometimes, as in the case of phosphor materials, it is necessary to maximize the exothermic effect and to increase the combustion temperature. However, in other cases (E.g. (nano)powders with large surface area), the combustion temperature must be properly decreased. From this point of view, the results published by the candidate and included in this habilitation thesis showed that:

  a) the increase of the combustion temperature can be achieved by:
    - ↑   using fuel mixtures (E.g. $LaAlO_3$ [23], $BaAl_2O_4$: Eu^{2+}, Dy^{3+} [24]),
    - ↑   using a suitable fuel (E.g. $CaZrO_3$ [25]),
    - ↑   adding an extra-energetic material (E.g. NH_4NO_3) to the reaction mixture (E.g. $ZnAl_2O_4$ [26]).

  b) the decrease of the combustion temperature can achieved by:
    - ↓   using an appropriate fuel (E.g. Fe_3O_4 [27], Fe_3O_4/C [28], γ-Fe_2O_3 [29]),
    - ↓   adding passive (E.g. NaCl) or active (E.g. $H_2C_2O_4$) retarding agents (E.g. $LaAlO_3$ [23], $CoFe_2O_4$ [30]) to the reaction mixture.

↓ using metal acetates instead of metal nitrates (E.g. $CoFe_2O_4$ [31]).

- **Atmosphere control during combustion reactions**: often in the case of oxide materials which contain metal ions having several oxidation numbers (Eg. transition and lanthanide metal ions), in addition to the combustion temperature the working atmosphere must be controlled as well. Conducting the combustion reactions under an oxidizing atmosphere is relatively an easy task, since in most of the cases the development of the combustion reaction in the presence of air leads to positive results. The situation becomes much more complicated when reducing atmosphere is required, because the use of a controlled-atmosphere furnace is not a viable option from the economic point of view. The results obtained by the candidate and reported in this habilitation thesis emphasize that a reducing atmosphere can be in situ created during the combustion reaction by a suitable control of synthesis conditions, such as:
  a) using fuel-reach compositions (E.g. $BaAl_2O_4$: Eu^{2+}, Dy^{3+} [24]),
  b) conducting the combustion reaction in the absence of air using a simple yet original solution (inside a flask) suggested by the candidate (E.g. Fe_3O_4 [27], Fe_3O_4/C [28]).

- **Hydrogen peroxide treatment – an effective method for carbon removal**: the presence of residual carbon originating from the incomplete combustion of organic compounds is a significant problem regardless of the preparation method, mainly because the carbon removal by annealing (thermal oxidation) adversely affects the size and morphology of the nanoparticles. Therefore, the candidate developed an innovative solution that relies on the chemical oxidation of residual carbon by hydrogen peroxide treatment. The efficiency of the suggested solution (chemical oxidation instead of thermal oxidation) was tested and confirmed in the case of $ZnAl_2O_4$ [32] and γ-Fe_2O_3 [29] nanopowders.

Some of the results included in this habilitation thesis, were obtained during the implementation of 2 research grants, while others were obtained during the collaboration with 2 PhD students, namely Alina (Tăculescu) Moacă [27,29] and Georgeta Mihoc [28] under the supervision of Prof. Cornelia Păcurariu.

For instance, temperature increase/decrease by using fuel mixtures and passive retarding salt (NaCl) additions – $LaAlO_3$ [23], temperature decrease by using metal (Eg. Zinc) acetate instead of metal nitrate – $ZnAl_2O_4$ [26] and chemical oxidation of residual carbon by hydrogen peroxide – $ZnAl_2O_4$ [32] were issues addressed in the framework of a CNCS – UEFISCDI grant devoted to the formation of young independent research teams (*Innovative solutions in the field of large surface area ceramic nanopowder preparation via combustion synthesis*, 740.000 RON, 2011–2014, PN-II-RU-TE-2011-3-0024, project number TE 18/05.10.2011). The candidate was the **project leader** (principal investigator) of this grant and coordinated a team of four members.

On the other hand, temperature decrease by using active retarding additions of oxalic acid – $CoFe_2O_4$ [30], temperature decrease by using metal (Eg. Cobalt) acetate instead of metal nitrate – $CoFe_2O_4$ [31]) and generating elevated combustion temperature under reducing atmosphere – $BaAl_2O_4$: Eu^{2+}, Dy^{3+} [24] were research topics addressed in the framework of a SOP HRD grant (*Development and implementation of master programs in the field of Micro and*

Nanomaterials, 1.829.940 RON, 2010–2013, SOP HRD, project number 86/1.2./S/58146). The candidate was involved in this project as a **long-term expert**.

The candidate has a sound international scientific activity in his field of research, as he published overall 40 peer-reviewed papers in ISI ranked journals (Fig. 1), 5 books, 1 Romanian OSIM patent and 1 Romanian OSIM patent application. According to Scopus, 24.04.2015 (Fig. 2), the papers of the candidate received a total number of 304 citations, 249 citations (self-citations and the citations of all co-authors excluded) and a Hirsch index h of 9 (self-citations and the citations of all co-authors excluded). The large number of received citations (249) suggests that the ISI papers published by the candidate have a significant contribution to the field of metal oxide (nano)powder preparation via combustion synthesis.
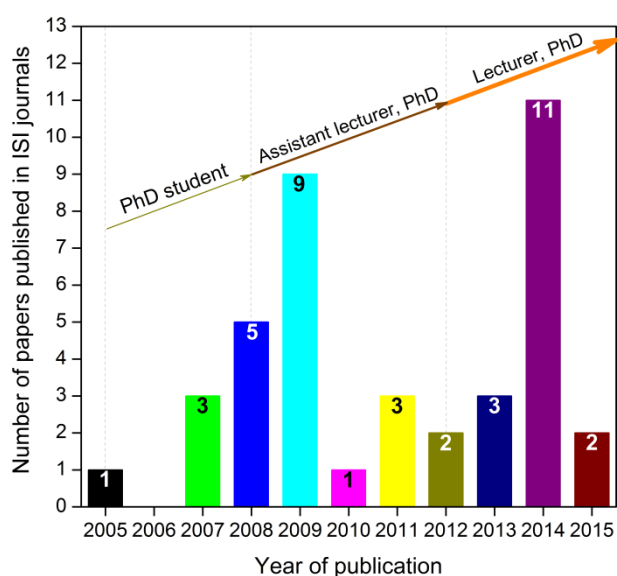
Fig. 1. Timeline / number of the ISI papers.   Fig. 2. Number of citations received over time.
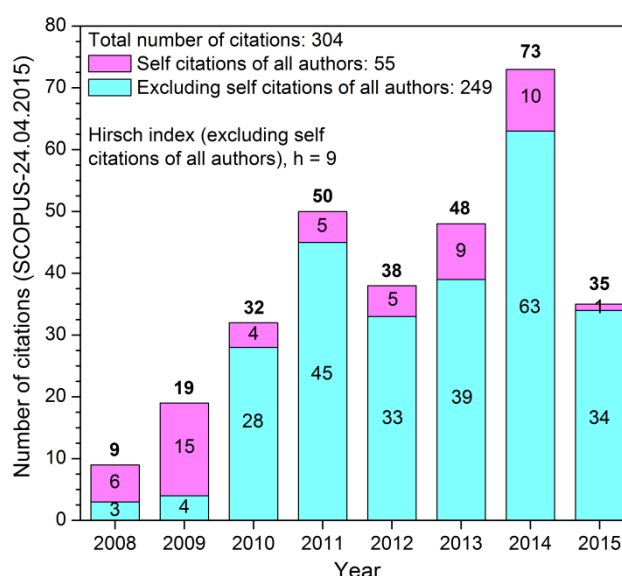
The quality of the ISI published papers is underlined by the high impact factor of the journals in which the candidate has published. More than half (62.5 %) of the papers were published in ISI journals with an impact factor ranging from 2 to 3 and 12.5 % papers were published in ISI journals with impact factor larger than 3 (Fig. 3). Among the 40 ISI articles, the candidate is the main author of 26 ISI articles (65 % of the total number of published ISI articles - Fig. 4), which reflects the high degree of autonomy of the candidate.
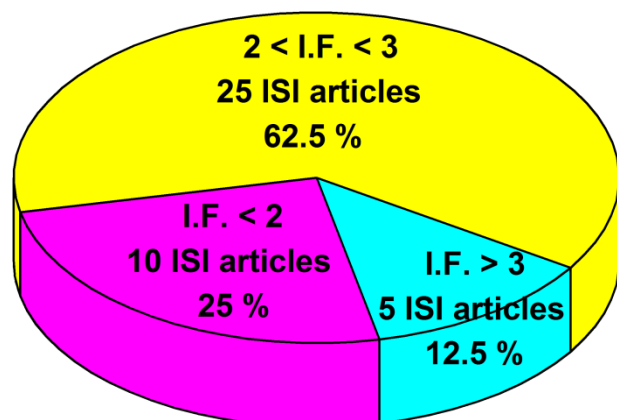
Fig. 3. Impact factor of the published articles.   Fig. 4. Main author and co-author articles share.
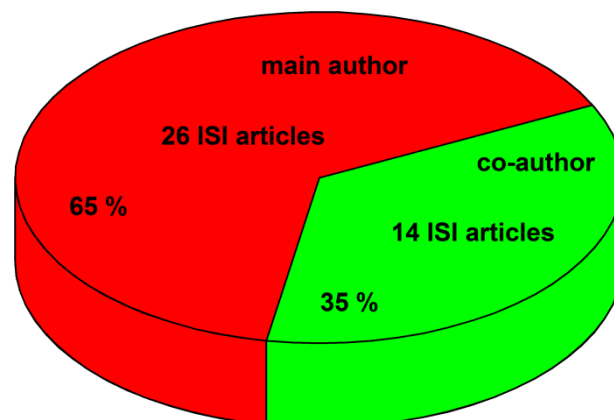
In 2010 the candidate was awarded the "IN HOC SIGNO VINCES" prize (distinction Magna cum Laude) for *outstanding achievements in scientific research*, by the CNCSIS – National Council for Scientific Research in Higher Education. In the same year the candidate was awarded the "EMINENT RESEARCHER" prize for *outstanding results in teaching and research activity*, by the Academic Horizons Association.

Based on his expertise, the candidate was invited to join the reviewer team of 22 prestigious ISI-ranked journals (Fig. 5), having reviewed more than 30 manuscripts.
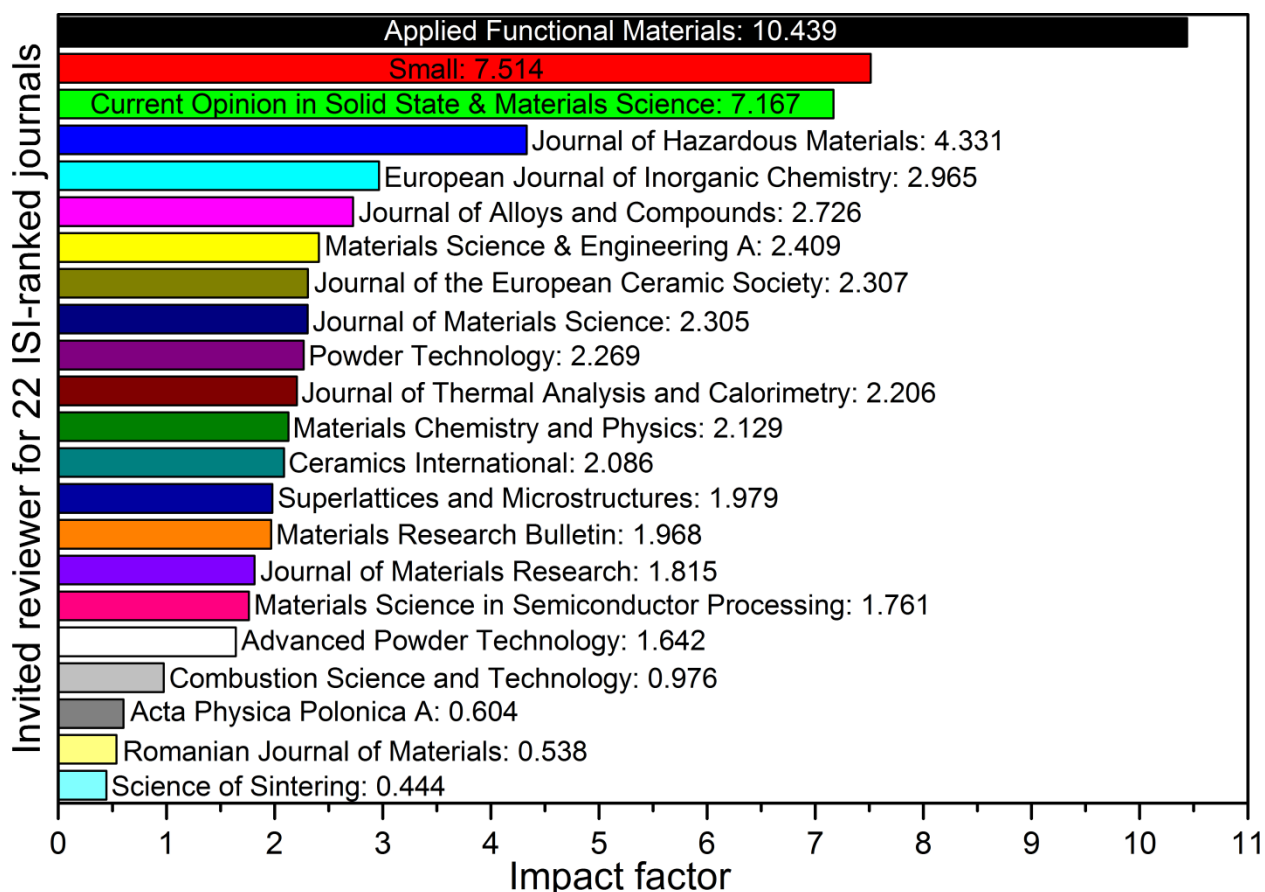
Fig. 5. 22 ISI-ranked journals have invited the candidate to join their reviewer team.

The ability of the candidate to coordinate research activities is also reflected by his presence as a member of the mentoring committees of four PhD students (namely Roxana Băbuță, Alina (Tăculescu) Moacă, Mihoc Georgeta and Oana Paşka), which have defended their PhD theses.

2.1.1. Temperature control during combustion reactions

The preparation of mixed metal oxides using conventional or non-conventional synthesis methods relies on the development of solid state reactions, which are primarily influenced by temperature. In the case of most chemical synthesis methods the energy (temperature) input necessary to carry out solid state reactions is often provided by an external heat source, typically from a furnace. On the other hand, combustion synthesis reactions, which are highly exothermic redox process, are able to self-generate (in situ) enough heat to facilitate the occurrence of solid state reactions and the formation of designed crystalline compounds, without the need of an external heat source. From this point of view, in this section of the thesis several case studies are presented ($LaAlO_3$, $CaZrO_3$, $ZnAl_2O_4$, $CoFe_2O_4$), describing a number of ways in which the combustion temperature (*the real maximum temperature developed during combustion reaction*) can be increased or decreased, depending on the targeted compound and required specifications.

2.1.1.1. Single-step combustion synthesis of LaAlO₃ powders

Chemical preparation of $LaAO_3$ via solution combustion synthesis is a typical example which highlights the need for increasing the combustion temperature developed during the self-propagating redox reaction. The candidate has shown that single-phase nanocrystalline $LaAlO_3$ powders can be prepared directly from the combustion reaction using a new cost effective, time saving and environmentally friendly version of the solution combustion synthesis [23]. Instead of using a single fuel, there has been used a fuel mixture of urea and β-alanine, considering the different reactivity of lanthanum and aluminum nitrates with respect to urea and β-alanine. It was this new version of the solution combustion synthesis that allowed the maximization of the exothermic effect associated to the combustion reaction. The addition of NaCl to the reaction mixture decreased the combustion temperature, promoting the increase of the BET surface area (8.5 m^2/g) and the decrease of $LaAlO_3$ crystallite size (36 nm). This work was supported by a grant of the Romanian National Authority for Scientific Research, CNCS – UEFISCDI, project number PN-II-RU-TE-2011-3-0024 (18/05.10.2011).

General context: perovskite structured $LaAlO_3$ has recently attracted considerable attention due to its remarkable properties: high melting point (2100 ºC), high quality factor, high dielectric constant, low toxicity, zero temperature coefficient of resonant frequency, chemical resistance [33]. Therefore, in the past few years $LaAlO_3$ has gained great importance in a wide variety of applications: electrically insulating buffer layer for the deposit of superconducting or ferroelectric materials [34,35], dielectric resonators, high frequency capacitors, sensors [36], microwave dielectrics, crystalline host for phosphor materials [37,38], SOFC electrolyte and electrode material [39,40], catalyst [41-45], ceramic pigments [46] etc.

Typically, $LaAlO_3$ is prepared by mixing La_2O_3 and Al_2O_3 powders, followed by solid-state reaction at high temperature, usually above 1500 ºC for several hours. This method presents a number of drawbacks, such as: high reaction temperature, long soaking time, large particle size, limited chemical homogeneity and low sinterability. In order to overcome these drawbacks, different soft chemical synthesis routes have been developed. Koc et al. prepared $LaAlO_3$ powders via sol-gel method after annealing the precursor gel at 1000 ºC for 3 hours [39].

According to Behera et al., pure $LaAlO_3$ could be prepared after annealing at 600 ºC for 4 hours the precipitate resulted from the destabilization of metal chlorides solutions with ammonia [41]. Spinicci et al. prepared $LaAl_{0.9}M_{0.1}O_3$ (M = Li^+, Mg^{2+}) by annealing the citrate precursors at 800 ºC for 5 hours and they reported an increasing of the catalytic activity and selectivity in

comparison to pure $LaAlO_3$ [42]. Making use of the Pechini method, Kakihana and Okubo synthesized $LaAlO_3$ powders after annealing the amorphous precursor at 700 ºC for 8 hours [43]. Kuo et al. prepared $LaAlO_3$ powders by chemical coprecipitation after annealing at 700 ºC for 6 hours [47]. Sahu et al. found that the use of gelation-precipitation technique and chloride-free precipitates led to the formation of pure $LaAlO_3$ perovskite phase at 600 ºC [48]. Li et al. synthesized pure $LaAlO_3$ powders via coprecipitation route after the heat treatment of the precursor at 800 ºC for 2 hours [49].

Several authors reported the synthesis of single-phase $LaAlO_3$ powders after annealing at 750-800 ºC for 2 hours the precursor resulted via ethylenediaminetetracetic acid precursor route [50,51]. Adak et al. obtained pure $LaAlO_3$ powder by heating a mixture of polyvinyl alcohol and a mixed metal nitrate solution at 675 ºC for 2 hours [52]. Li et al. prepared single-phase $LaAlO_3$ powder using equimolecular La_2O_3 and Al_2O_3 as reactants in a molten KF-KCl eutectic salt for 3 hours between 630 ºC and 800 ºC [53].

In the last years, combustion synthesis has become a fast, eco-friendly and energy-efficient route for the preparation of various oxide powders [5]. However, several authors failed to achieve single-phase $LaAlO_3$ powders directly from the combustion reaction. For instance, Taspinar and Tas reported that combustion synthesis with urea yields a foamy amorphous precursor, which turns into crystalline $LaAlO_3$ only after annealing at 650 ºC for 16 hours [33]. Tian et al. obtained similar results, showing that glycine leads to single-phase $LaAlO_3$ powders only after annealing the combustion residue at 700 ºC for 2 hours [54].

Experimental: in this case study $La(NO_3)_3 \cdot 6H_2O$ (Merck), $Al(NO_3)_3 \cdot 9H_2O$ (Merck), urea (CH_4N_2O, Merck), β-alanine ($C_3H_7NO_2$, Merck) and NaCl (Merck) were used as starting materials. Molar compositions of the designed samples are shown in Table 1. The first two samples were designed using a single fuel, urea (sample 1) or β-alanine (sample 2), whereas sample 3 involves the use of urea and β-alanine fuel mixture. Sample 4 derives from sample 3, having an addition of NaCl (50 weight % with respect to theoretical yield of $LaAlO_3$). Batches were calculated for 0.06 moles of $LaAlO_3$.

Table 1. Molar compositions of the investigated samples.

No.	Oxidizing agent		Reducing agent (fuel)		Salt retardant
	$La(NO_3)_3$	$Al(NO_3)_3$	CH_4N_2O	β-$C_3H_7NO_2$	NaCl
1.	2	2	10	-	-
2.	2	2	-	4	-
3.	2	2	5	2	-
4.	2	2	5	2	50 wt.% with respect to $LaAlO_3$

Stoichiometric metal nitrate/fuel molar ratios were used in all samples. It was assumed that the combustion reaction by-products are: CO_2, H_2O and N_2. The required amounts of metal nitrates (and NaCl) were dissolved in 20.0 mL of distilled water in a porcelain-evaporating dish (Fig. 6). Subsequently, the appropriate amount of fuel was added according to each recipe: sample 1 (urea), sample 2 (β-alanine), samples 3 and 4 (urea and β-alanine). The resulting clear solution was rapidly heated to 300 ºC inside a heating mantle causing water evaporation and the ignition of a self-sustaining combustion reaction, except for sample 1 which failed to ignite. The

time span between the initiation of the combustion reaction and its finalization was measured. The resulted powders were hand grounded, washed with distilled water and then dried (Fig. 6).
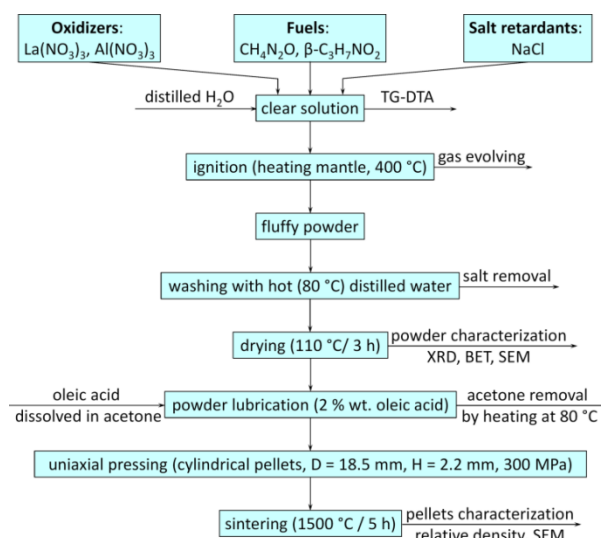

Fig. 6. Flowchart of $LaAlO_3$ preparation, sintering and characterization.

Heating behavior of the precursor solutions were monitored by thermal analysis, using a Netzsch 449 C instrument. TG-DTA curves were recorded over the interval 25-800 °C using Pt crucibles, under an artificial air flow of 20 mL/min, at a heating rate of 10 °C/min.

In order to estimate the combustion reaction completeness, "loss on ignition" (LOI) parameter was used as an indicator of the amount of residual gasifiable components in the obtained powders. For a complete combustion, the "loss on ignition" of the resulted powder should be zero. LOI was determined by weighing the obtained samples before and after annealing at 800 ºC for 2 hours.

The phase composition of the samples was studied by X-ray diffraction (XRD), using a Rigaku Ultima IV instrument ($Cu_{K\alpha}$ radiation) operating at 40 kV and 40 mA. The average crystallite size was determined based on the XRD patterns using the PDXL 2.0 software.

BET (Brunauer, Emmett and Teller) surface area measurements were performed at 77 K using a Micromeritics ASAP 2020 instrument and N_2 as the adsorption gas.

In order to investigate the sintering behavior, $LaAlO_3$ powders were lubricated with 2 % oleic acid dissolved in acetone. Cylindrical pellets of 2.2 mm height x 18.5 mm diameter were obtained by uniaxial pressing at 300 MPa. Pellets were sintered at 1500 °C for 5 hours (Fig. 6).

The particle size and morphology were explored by scanning electron microscopy, using a FEI Quanta FEG 250 microscope.

Results and discussion: no visible combustion reaction could be observed in the case of sample 1, where urea was used as fuel. Instead, large amounts of reddish-brown gases (NOx) evolved. The resulted product was a white material. XRD analysis evidenced that the obtained material is amorphous, which agrees with the results reported by Taspinar and Tas [33]. Small peaks of $LaO(NO_3)$ could be identified on the XRD pattern (Fig. 7). The absence of the combustion reaction is also confirmed by the large value of loss on ignition (Table 2).

In the case of β-alanine (sample 2) a smoldering combustion reaction took place, leading to the formation of a gray powder, which suggests the presence of carbon impurities. In this case, the energy released during the combustion reaction enabled the formation of $LaAlO_3$ that had an

average crystallite size of 33 nm. The XRD pattern of sample 2 revealed that the combustion reaction product also contains small traces of La_2O_3 (Fig. 7).

Table 2. Characteristics of the samples prepared in different combustion synthesis conditions.

No.	Reaction time (s)	Sample color	XRD phase composition	D_{XRD} (nm)	L.O.I. (%)
1.	no combustion	White	$LaO(NO_3)$	-	33.1
2.	45	Grey	$LaAlO_3 + La_2O_3$	33	3.0
3.	40	White	$LaAlO_3$	46	0.2
4.	65	White	$LaAlO_3$	36	0.3

Loss on ignition of sample 2 is much lower compared to sample 1 (Table 2), which might be explained by the different heating behavior of the two precursors. Although, β-alanine seems to be a better fuel than urea, none of the two fuels is able to yield single-phase $LaAlO_3$ directly from the combustion reaction.

On the other hand, urea and β-alanine fuel mixture (sample 3) triggered a vigorous combustion reaction, which was accompanied by the presence of flames, lasting for 40 seconds. Thermal analysis of the aqueous solution of $La(NO_3)_3$, $Al(NO_3)_3$, urea and β-alanine (precursor 3) is shown in Fig. 8. The DTA curve presents an endothermic effect (117 °C) which is accompanied by a mass loss which can be assigned to water removal. At 281 °C an intense exothermic effect appears on the DTA curve, which can be associated to the combustion reaction. This process is accompanied by a sharp mass loss on the TG curve. Above 300 °C neither thermic effects nor mass variation processes can be seen on TG-DTA curves.
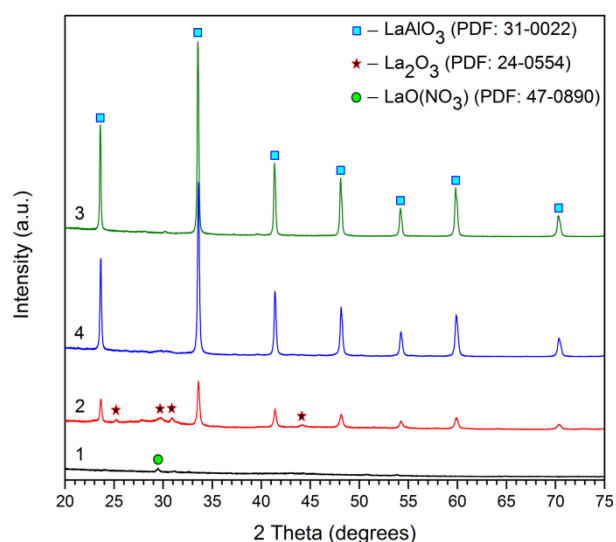
Fig. 7. XRD patterns of the samples 1-4.   Fig. 8. TG-DTA curves of precursor solution 3.
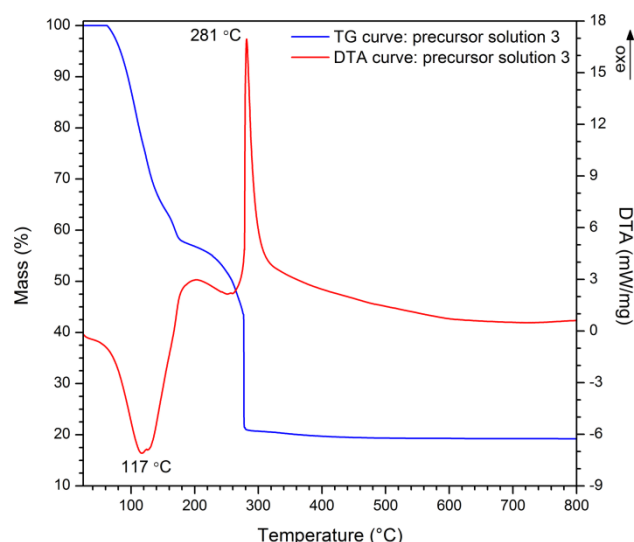
XRD analysis conducted on the combustion synthesized white powder indicates that $LaAlO_3$ is the single crystalline phase. The resulted $LaAlO_3$ powder had an average crystallite size of 46 nm and a BET surface area of 3.0 m^2/g. The relatively low surface area is the result of the intense heat released during the combustion process.

In order to increase the BET surface area of $LaAlO_3$ powder, the combustion temperature had to be decreased. Therefore NaCl was added to the starting aqueous solution (sample 4). Due to the presence of NaCl, which acted as a retardant, the combustion reaction was less vigorous

and lasted a little bit longer, for 65 seconds. The presence of NaCl did not change the phase composition but decreased the $LaAlO_3$ crystallite size to 36 nm. At the same time, the BET surface area increased to 8.5 m^2/g.

By comparison to single fuel recipes (samples 1 and 2), fuel mixture recipes (samples 3 and 4) exhibit considerably lower losses on ignition, which is in agreement with the combustion reaction evolution (Table 2). Compared with the results reported by other authors [33,54,55] who used the single fuel combustion approach followed by supplementary annealing, one may notice that our new [23] solution of using urea and β-alanine fuel mixture enabled the formation of $LaAlO_3$ directly from the combustion reaction. Therefore, there was no need for an additional annealing step (Table 3). Moreover, the average crystallite size of $LaAlO_3$ obtained in this study is smaller than the one reported in the literature (Table 3).

Table 3. Comparison of the results reported hereby [23] with other results from the literature.

Fuel	Annealing conditions	Crystallite size (nm)	Relative density (%)	References
Urea	650 °C / 16 h	-	99 (1500 °C / 6 h)	[33]
Glycine	700 °C / 2 h	78	95 (1550 °C / 12 h)	[54]
Glycine	800 °C / 4 h	60	-	[55]
Urea + β-alanine	No annealing	36	94 (1500 °C / 5 h)	[23]

SEM image of sample 4 (Fig. 9) shows that the $LaAlO_3$ powder resulted from the combustion reaction consists of highly porous agglomerates of round shaped particles. The porous structure could be caused by the large volume of gases (CO_2, H_2O, N_2) released during the combustion reaction. On the other hand, the round shape of the particles (Fig. 9 inset) might be related to the presence of NaCl, which melts during the combustion process and forces $LaAlO_3$ particles to adopt a spherical shape.

This type of particle morphology had a positive influence during the pressing and sintering stage. After sintering at 1500 ºC for 5 hours, sample 4 reached a relative density of 94 % of the theoretical density, which is quite a reasonable value given the difficulty of $LaAlO_3$ sintering (Table 3). The resulting microstructure of the sintered pellet consists of fine cubic $LaAlO_3$ particles having particle size less than 5 μm (Fig. 10).
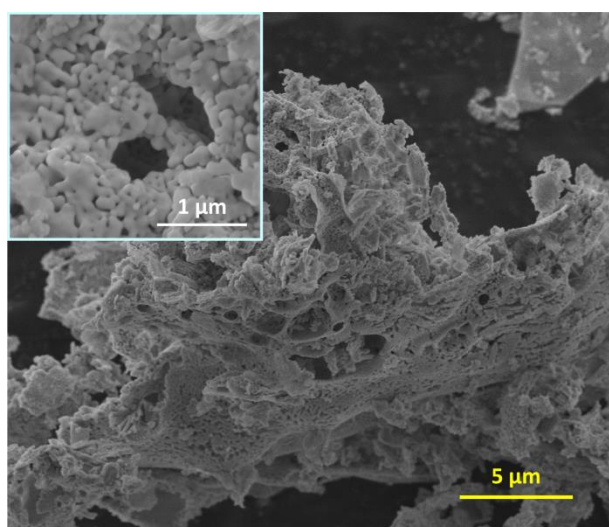

Fig. 9. SEM image of sample 4, resulted from the combustion reaction.
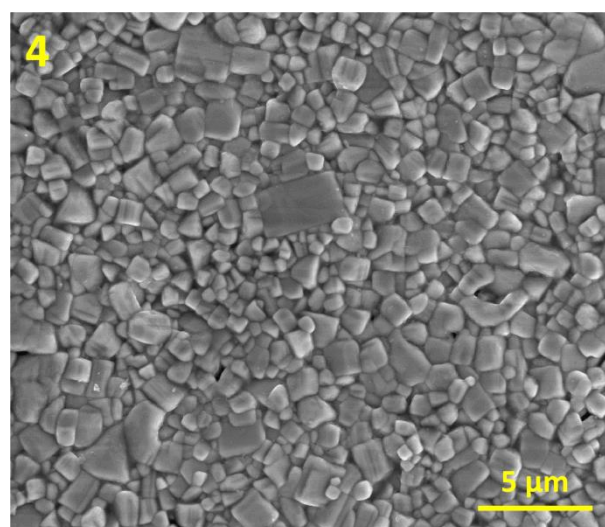
Fig. 10. SEM image of sample 4 after sintering at 1500 ºC for 5 hours.

Key findings

✓ Single-phase $LaAlO_3$ was prepared by a simple combustion synthesis procedure, which relies on using urea and β-alanine fuel mixture, instead of a single fuel.

✓ The use of urea and β-alanine fuel mixture increases the combustion temperature promoting the formation of $LaAlO_3$ directly from the combustion reaction – without the need of supplementary annealing. The combustion synthesized $LaAlO_3$ had an average crystallite size of 46 nm and a BET surface area of 3.0 m^2/g.

✓ The addition of NaCl retarding agent to the precursor solution decreased the combustion temperature achieved within the reaction mixture. Consequently, the BET surface area of $LaAlO_3$ powder almost tripled (8.5 m^2/g), whilst the average crystallite size decreased to 36 nm. After sintering at 1500 °C for 5 hours, $LaAlO_3$ pellets developed a fine uniform microstructure reaching 94 % of the theoretical density.

✓ Single fuels recipes (urea, β-alanine) failed to yield single-phase $LaAlO_3$ directly from the combustion reaction. Under these circumstances, additional annealing was mandatory for the development of crystalline $LaAlO_3$.

2.1.1.2. Solution combustion synthesis of calcium zirconate, CaZrO₃, powders

Solution combustion synthesis of calcium zirconate is another example which emphasizes the need for an elevated combustion temperature. Since both, $Ca(NO_3)_2$ and $ZrO(NO_3)_2$, have the similar reactivity with respect to β-alanine and both of them do not react with urea, a different approach has been used, namely single-fuel recipes based on β-alanine, $β-C_3H_7NO_2$ [25]. TG-DTA analysis indicated that a stoichiometric mixture of $Ca(NO_3)_2$, $ZrO(NO_3)_2$ and $β-C_3H_7NO_2$ (molar ratio = 3:3:4) undergoes an intense exothermic reaction at 255 °C, which lead to the formation of single-phase nanocrystalline $CaZrO_3$ powder (23.9 nm).

General context: the $CaO-ZrO_2$ system is one of the main research topics material scientists are focused on. However, most of the investigations aimed the synthesis and characterization of CaO stabilized ZrO_2 solid solutions and little attention has been paid to the study of $CaZrO_3$ phase. Although the existence of $CaZrO_3$ in the $CaO-ZrO_2$ equilibrium diagram is known for several decades, it was only in 2008 this mineral has been identified in nature in the North Caucasus, Kabardino-Balkaria region, Russia [56].

Calcium zirconate, $CaZrO_3$, also known as lakargiite is a refractory compound, which congruently melts at 2340 °C [56]. In terms of crystalline structure, $CaZrO_3$ is an orthorhombic perovskite consisting of slightly deformed $[ZrO_6]$ octahedra and $[CaO_8]$ [57,58]. At 1750 °C $CaZrO_3$ undergoes polymorph transformation: orthorhombic $CaZrO_3$ → cubic $CaZrO_3$. Due to its valuable properties, $CaZrO_3$ is a ceramic material which is currently being used in a wide range of applications: multilayer ceramic capacitors [59], solid electrolyte [60], crystalline host for phosphor materials [61] and ceramic pigments [62], moderate temperature thermal barrier [63], catalyst [64] etc. According to Azimov et al. [62], in many aspects $CaZrO_3$ shows better properties than the solid solutions of CaO stabilized ZrO_2. The same authors emphasized that the sintering process, as well as the mechanical, electrical and chemical properties of $CaZrO_3$ products are negatively affected by presence of traces of free CaO and ZrO_2 [65].

The preparation of $CaZrO_3$ powders via ceramic route involves annealing a mixture of $CaCO_3$ and ZrO_2 at elevated temperature for several hours, followed by an intensive milling operation to reduce the grain size. For instance, Wang et al. [66] reported the preparation of single-phase $CaZrO_3$ powders by annealing stoichiometric mixtures of $CaCO_3$ and ZrO_2 in the temperature range of 1000÷1400 ºC for 12 hours. Similar results were presented by Hwang and Choi [67], who prepared $CaZrO_3$ from $CaCO_3$ and ZrO_2 after a heat treatment of 4 h at 1350 °C.

The $CaZrO_3$ powders obtained by the ceramic method present several major drawbacks (large particle size, wide grain size distribution, low surface area, high agglomeration degree, lack of chemical homogeneity etc.), which are detrimental to the sintering process. Róg et al. [57] prepared dense $CaZrO_3$ with a relative density higher than 95 % after annealing at 1600 °C for 12 hours. Wang et al. [66] managed to obtain 95 % of the theoretical density of $CaZrO_3$ after sintering the cold-pressed specimens at 1550 ºC for 48 hours. In order to overcome the disadvantages of the ceramic method, new chemical preparation methods have been tested.

Zhang et al. [61] synthesized $CaZrO_3$:Eu red phosphor at 1000 °C by the polymerization complex method based on the Pechini-type reaction. Gonenli and Tas [68] reported the preparation of pure $CaZrO_3$ powders by annealing at 1200 ºC for 17 hours the amorphous precursor obtained from the combustion reaction of corresponding metal chlorides with urea. Prasanth et al. [69] synthesized pure $CaZrO_3$ powders with crystallite size of 33 nm by annealing at 700 ºC the amorphous powder resulted from the reaction of calcium nitrate, zyrconil oxy-

chloride, citric acid and urea. Yu et al. [70] applied the sol-gel method for the preparation of thin films and concluded that pure $CaZrO_3$ films could be obtained at 1000 °C.

Experimental: $CaZrO_3$ powders were prepared by using two different synthesis methods: the solution combustion synthesis and the ceramic method, which was used for comparison. Table 4 shows the starting raw materials as well as the molar ratio of the investigated samples. In both synthesis routes recipes were designed in order to obtain 0.06 moles of $CaZrO_3$.

Table 4. Molar composition of the designed samples.

Sample	$Ca(NO_3)_2 \cdot 4H_2O$ Merck, pro analysi	ZrO_2 Carlo Erba, pro analysi	$ZrO(NO_3)_2$ Fluka, purum	β-$C_3H_7NO_2$ Merck, pro analysi
1 (ceramic method)	1	1	-	-
2 (combustion synthesis)	3	-	3	4

Since the general procedure for the synthesis of $CaZrO_3$ via ceramic route is widely known (Fig. 11), only the solution combustion synthesis of $CaZrO_3$ is described in detail below. According to the thermo-chemical concepts from propellants chemistry the energy released by a combustion reaction is maximum when the total oxidizing and reducing valences of metal nitrates and fuel reach unity, which corresponds to a $Ca(NO_3)_2$:$ZrO(NO_3)_2$:$C_3H_7NO_2$ molar ratio of 3:3:4. An aqueous solution of β-alanine was initially prepared by dissolving 0.24 moles of β-$C_3H_7NO_2$ in 30 mL of distilled water (Fig. 12). 0.18 moles of $ZrO(NO_3)_2$ and 0.18 moles of $Ca(NO_3)_2 \cdot 4H_2O$ were subsequently added to the solution of β-alanine under continuous stirring.

Fig. 11. The preparation of $CaZrO_3$ powder via ceramic route (sample 1).
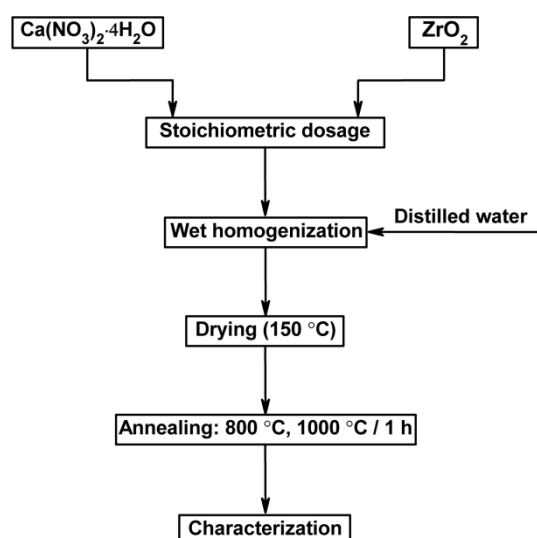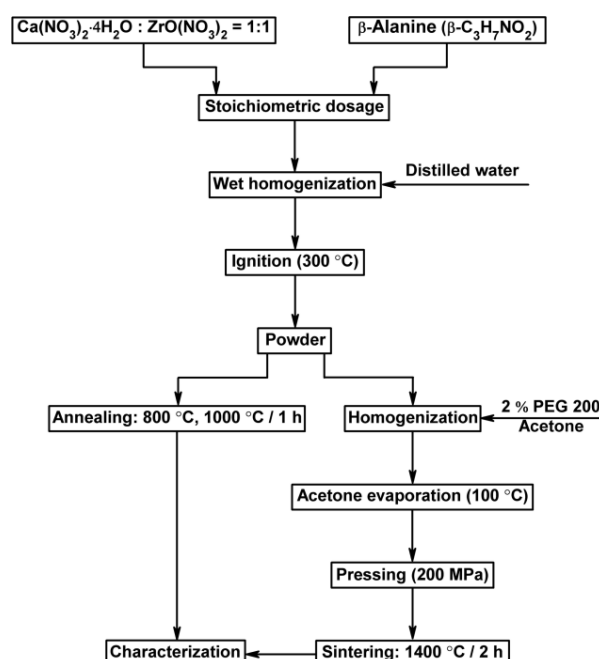
Fig. 12. The preparation of $CaZrO_3$ powder via solution combustion synthesis (sample 2).

The porcelain evaporating dish containing the clear solution was then placed in a heating mantle preheated at 300 °C. In the beginning the solution boils, foams and undergoes intense flaming combustion, yielding a very voluminous white powder. The resulting powder was

uniaxial pressed at 200 MPa into pellets of 2 mm height and 25 mm diameter in order to investigate the sintering behavior of $CaZrO_3$. 2 weight % polyethylene glycol (PEG 200) was added as plasticizer. In order to achieve a better distribution of the plasticizer, the necessary amount of PEG 200 was initially dissolved in acetone and the acetone was subsequently removed by evaporation (Fig. 12). The green pellets were annealed at 1400 °C for 2 hours. Water absorption, open porosity and apparent density of the sintered pellets were determined using the Archimedes principle. Small portions of the powders prepared using the two synthesis routes were annealed at 800 °C and 1000 °C for 1 hour in a muffle furnace.

Heating behavior of the precursor mixture containing $Ca(NO_3)_2$, $ZrO(NO_3)_2$ and β-$C_3H_7NO_2$ (sample 2) was investigated by thermal analysis using a Netzsch STA 449 C instrument equipped with alumina crucibles. The TG and DTA curves were recorded under N_2 atmosphere over the interval 25÷700 °C at a heating rate of 10 °C/min. The phase composition of the powders was determined by XRD, using a Bruker D8 Advance System (monochromatic $Cu_{K\alpha}$ radiation) operating at 40 kV and 40 mA. The average crystallite size was calculated based on the XRD patters using the Sherrer's equation (1).

$$D_{XRD} = \frac{0.9 \cdot \lambda}{\beta \cdot \cos\theta} \tag{1}$$

where: D_{XRD} is the crystallite size (nm), λ is the radiation wavelength ($Cu_{K\alpha}$, 0.15406 nm), β is the full width at half of the maximum (radians) and θ is the Bragg-angle.

The peaks used for the crystallite size calculation were the ones corresponding to 101 and 202 hkl planes. BET (Brunauer, Emmett and Teller) surface area measurements were performed using a Micromeritics ASAP 2020 instrument and nitrogen as adsorption gas. The grain size, D_{BET}, was calculated using equation (2):

$$D_{BET} = \frac{6000}{\rho \cdot S_{BET}} \tag{2}$$

where: D_{BET} is the grain size (nm), ρ is the theoretical density of $CaZrO_3$ (4.78 g/cm^3), S_{BET} is the BET surface area (m^2/g).

The morphology of the powders was investigated by SEM using a FEI Inspect S scanning electron microscope. The SEM images were acquired after the powder has been fixed to the aluminum support using a double-faced carbon tape. Elemental analysis was performed by Energy Dispersive X-ray Analysis (EDAX) using the same instrument.

Using the thermodynamic data available in [71-73] and assuming that combustion reaction is complete (that is to say that the reaction by-products are N_2, CO_2 and H_2O), the standard enthalpy of reaction as well as and the adiabatic temperature, T_{ad}, were calculated (3).

$$T_{ad} = T_0 + \frac{\Delta H^0_{f,r} - \Delta H^0_{f,p}}{C_p} \tag{3}$$

where: T_{ad} is the adiabatic temperature (K); T_0 is 298 K; $\Delta H^0_{f,r}$ and $\Delta H^0_{f,p}$ are the standard enthalpies of formation of reactants and reaction products (kJ/mol), respectively; C_p is the heat capacity of reaction products at constant pressure in (kJ/molK).

Results and discussion: *in the case of the ceramic method* the formation of $CaZrO_3$ could be described by reaction (4). The standard enthalpy of reaction (4) is 142 kJ/mol, which indicates that under standard conditions reaction (4) is an endothermic process.

$$Ca(NO_3)_{2(c)} + ZrO_{2(c)} = CaZrO_{3(c)} + 2\ NO_{2(g)} + \tfrac{1}{2}\ O_{2(g)} \tag{4}$$
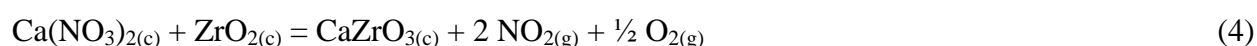
Experimental results revealed that during annealing an equimolecular mixture of $Ca(NO_3)_2$ and ZrO_2 (sample 1) the formation of $CaZrO_3$ begins at relatively low temperature, below 800 °C (Fig. 13). However, in order to achieve $CaZrO_3$ as a single phase a higher temperature is required. XRD analysis indicated that the powder obtained after annealing the mixture of $Ca(NO_3)_2$ and ZrO_2 (sample 1) at 800 °C for 1 hour is a mixture of three crystalline phases: $CaZrO_3$, unreacted ZrO_2 and free CaO, which originates from the thermal decomposition of $Ca(NO_3)_2$ (Fig. 13). In addition, the resulted powder has very low specific surface area (1.5 m^2/g) (Table 5). Since it is generally known that low surface area powders exhibit a poor sintering behavior, the solution of increasing furthermore the annealing temperature – in order to obtain pure $CaZrO_3$ – is a futile alternative. Indeed, raising the annealing temperature to 1000 °C has no positive effect on the phase composition of the powder, since alongside $CaZrO_3$, CaO and ZrO_2 (which still persist) a new crystalline phase appears: CaO stabilized ZrO_2 solid solution (Fig. 13).
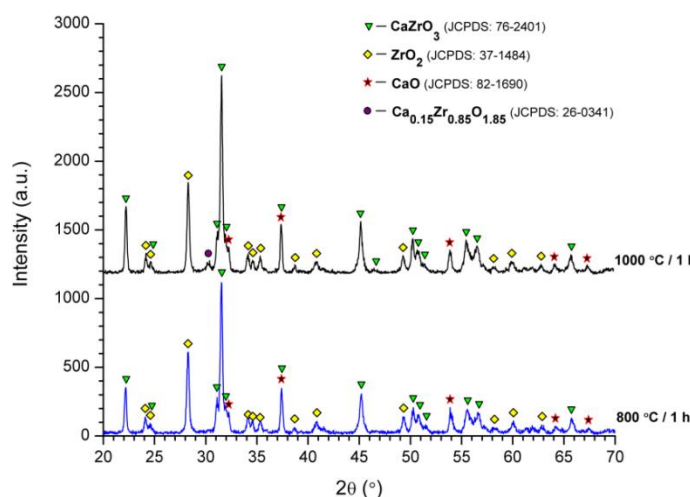
Fig. 13. XRD patterns of the powders prepared via ceramic method (sample 1), after annealing.
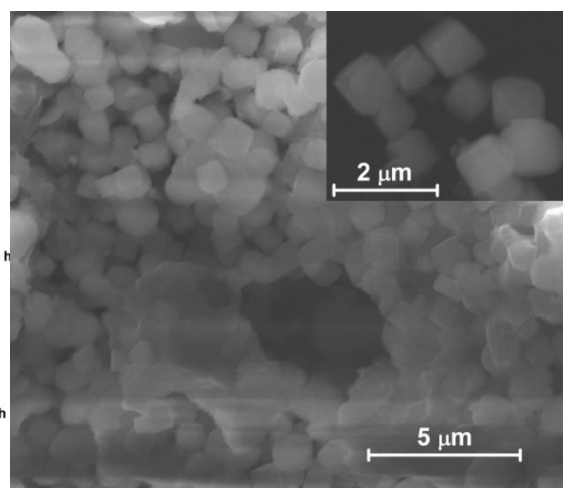
Fig. 14. SEM image of sample 1 after annealing at 1000 °C for 1 hour.

The presence of cubic CaO stabilized ZrO_2 solid solution is also confirmed by the SEM images of powder 1 annealed at 1000 °C (Fig. 14). At the same time, there is a slight increase of the $CaZrO_3$ crystallites from 28.4 nm to 28.7 nm, whereas the specific surface area decreases to 1.4 m^2/g (Table 5). The huge difference between D_{BET} and D_{XRD} in the case of powder 1 annealed at 800 °C and 1000 °C indicates that each grain contains a very large number of crystallites and the crystallites are highly agglomerated (Table 5).

Table 5. Average crystallite size (D_{XRD}), surface area (S_{BET}) and grain size (D_{BET}) of powders.

Sample	Before annealing			800 °C / 1 h			1000 °C / 1 h		
	D_{XRD} (nm)	S_{BET} (m²/g)	D_{BET} (nm)	D_{XRD} (nm)	S_{BET} (m²/g)	D_{BET} (nm)	D_{XRD} (nm)	S_{BET} (m²/g)	D_{BET} (nm)
1	-	-	-	28.4	1.5	836.8	28.7	1.4	896.6
2	23.9	21.5	58.4	25.3	20.1	62.4	28.1	13.5	93.0

The synthesis of $CaZrO_3$ via ceramic method takes place very difficult, at temperatures exceeding 1000 °C. Under these circumstances the obtained powders are highly agglomerated and have very low surface areas. These features point out that $CaZrO_3$ powders prepared by the ceramic method are very difficult to sinter, which is also confirmed by other papers [57,66].

The solution combustion synthesis: reaction (5) describes in a simplified manner the formation of $CaZrO_3$ via solution combustion synthesis – also known as low-temperature combustion synthesis. One should consider that the terminology "low-temperature combustion synthesis" does not refer to the maximum combustion temperature – which can easily exceed 1000 °C – but rather to the ignition temperature, which occurs at low temperature (< 300 °C).

$$3\ Ca(NO_3)_{2(aq)} + 3\ ZrO(NO_3)_{2(aq)} + 4\ C_3H_7NO_{2(aq)} =$$
$$= 3\ CaZrO_{3(c)} + 12\ CO_{2(g)} + 14\ H_2O_{(g)} + 8\ N_{2(g)} \quad (5)$$
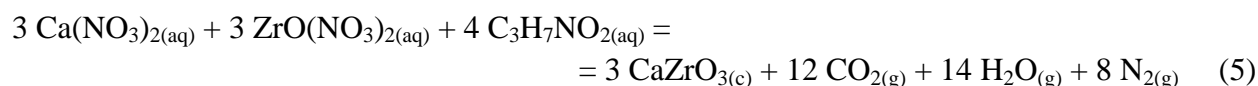
Basically, in the case of this method, the heat required for the $CaZrO_3$ formation is not supplied by an external source – as in the case of the ceramic method – but is self-generated by the exothermic reaction between $Ca(NO_3)_2$, $ZrO(NO_3)_2$ and β-alanine. The highly exothermic nature of this process is confirmed by the negative standard enthalpy of reaction (5), which is -947 kJ/mol. Fig. 15 depicts a series of successive digital images recorded during different stages of the combustion reaction (5). Numbers on each image represent the time (in seconds) when that frame was recorded. Time stamps are relative to the first frame in the series.
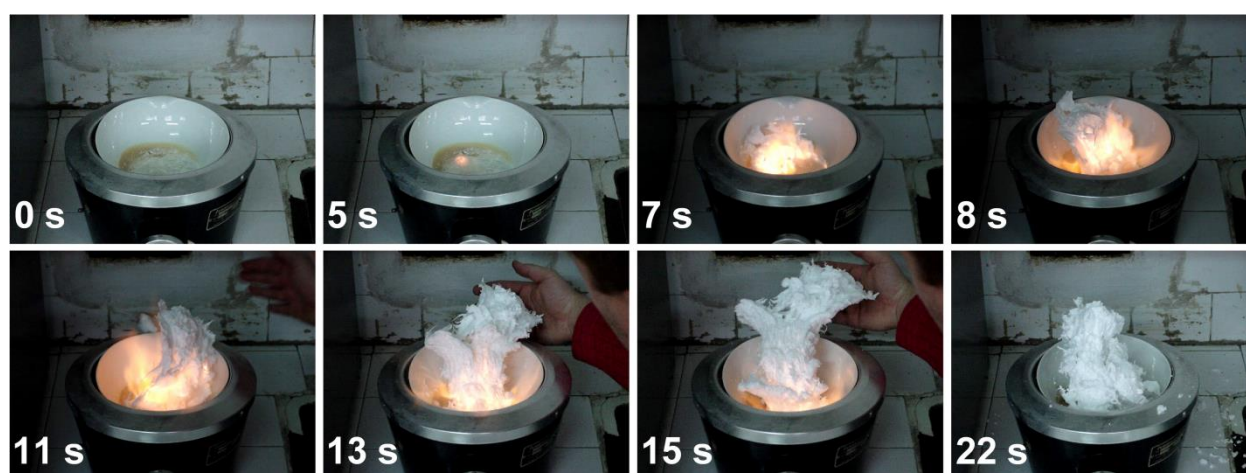

Fig. 15. Different stages of the combustion reaction (5).

Fig. 15 clearly indicates the ignition and the propagation of the reaction front evidenced as a highly incandescent area. The presence of glowing flames and the absence of reddish-brown gases (NO_x) could have also been noticed. During the combustion process – which takes 17

seconds – the sample undergoes huge expansion, generating a very fluffy white reaction product (Fig. 15), which was easily crumbled using a pestle and a mortar. Although no advanced milling operation was performed, the specific surface area of this powder was 21.5 m^2/g (Table 5).

The DTA curve of the precursor mixture 2 (Fig. 16) indicates that an endothermic process takes place at 111 °C, which could be assigned to water removal. The total mass loss assigned to this process is about 50 %, as seen on the TG curve.
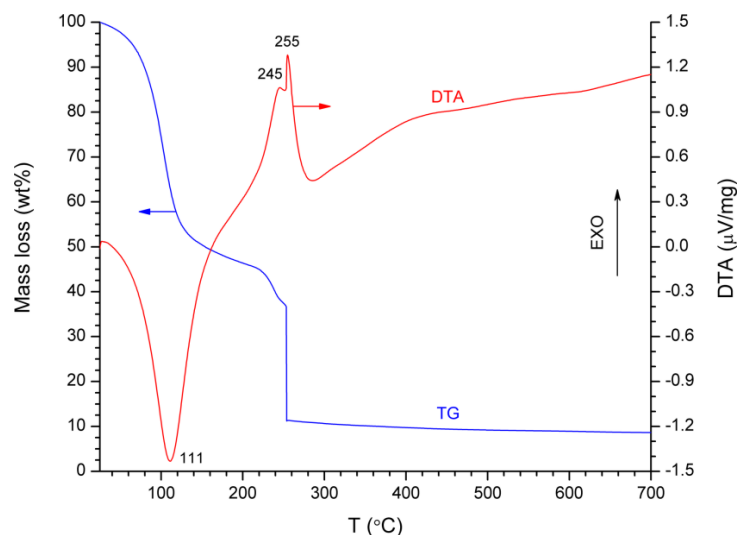
Fig. 16. TG-DTA curves of the precursor mixture 2 (solution combustion synthesis).

The ignition of the combustion process occurs at 245-255 °C. The exothermic peak is accompanied by a mass loss of about 40 % on the TG curve. Both, the exothermic peak on the DTA curve and the rapid and significant mass loss on the TG curve are typical for combustion reactions. After the combustion process reached to an end, the sample underwent no more transformations. The lack of other phenomena accompanied by mass loss is in agreement with the negligible loss on ignition (1.6 %) of powder 2. Actually, the elemental composition of combustion-synthesized powder (Fig. 17) – which contains no C or N – leads to the conclusion that the adsorbed moisture, H_2O, is solely responsible for this loss on ignition. It is also noteworthy that the elemental composition of the powder 2 expressed in atomic % (Fig. 17) is very close to the theoretical composition of pure $CaZrO_3$: 20 % Ca, 20 % Zr and 60 % O.
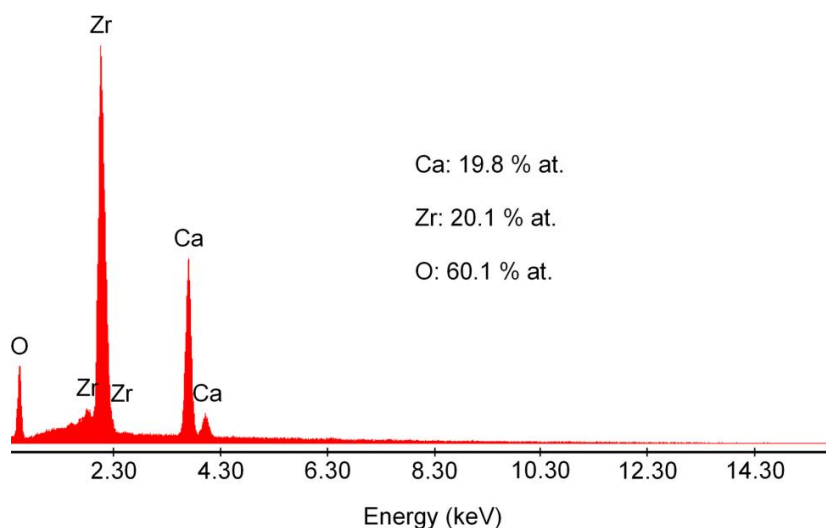
Fig. 17. X-ray emission spectra of powder 2, resulted from the combustion reaction.

The adiabatic temperature (*the maximum theoretical temperature reached during the combustion process, assuming that reaction is conducted under adiabatic conditions*) of combustion reaction (5) is 2262 K. Although in reality the combustion temperature is lower than the adiabatic temperature due to various factors (heat loss, incomplete combustion etc.) it seems that the $CaZrO_3$ formation requirements are met. XRD analysis revealed that the powder resulted from the combustion reaction consists of single-phase $CaZrO_3$ (Fig. 18) and has an average crystallite size of 23.9 nm (Table 5).

Fig. 18. XRD patterns of the powders prepared via solution combustion synthesis (sample 2), before and after annealing at 800 °C and 1000 °C for 1 hour.
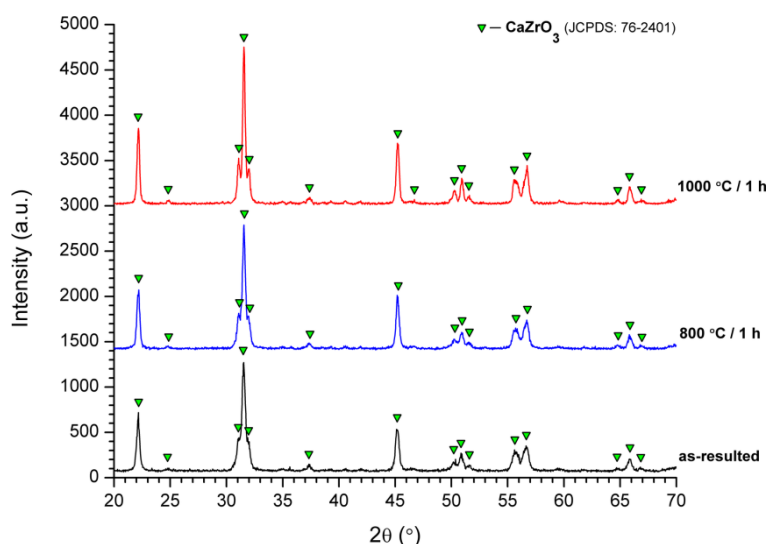
Unlike the powder prepared by the ceramic method where the D_{BET}/D_{XRD} ratio is about 30, in the case of the combustion synthesized powder, the grain size, D_{BET}, is only 2.4 times larger than the crystallite size, D_{XRD}, which reflects much smaller grains and lower agglomeration tendency (Table 5). Despite other reports, which indicate the an amorphous product results from the combustion reaction [68], it seems that under the right circumstances, the combustion method is able to ensure the formation of $CaZrO_3$ directly from the combustion reaction and no addition heat treatment is required. It is quite obvious that the reason for the difficult formation of $CaZrO_3$ – as Gonenli and Tas [68] have reported – is the lack of the combustion reaction caused by the inadequate choice of the starting raw materials (metal chlorides and urea). Given the fact that metal chlorides do not act as oxidizers, metal nitrates should have been used instead of metal chlorides. Moreover, since urea induces the precipitation of ZrO_2, which alters both the homogeneity of the raw material mixture and the redox balance of the combustion process, another fuel should have been used.

The heat treatment at 800 °C or 1000 °C for 1 hour does not change the phase composition of powder 2 (Fig. 18), but leads to the increase of the $CaZrO_3$ crystallites. At the same time, a significant decrease of the specific surface area occurs due to pore closure within $CaZrO_3$ grains (Table 5). The SEM image of powder 2 indicates that $CaZrO_3$ grains resulting from the combustion reaction have a scaly appearance similar to thin foils, which form a veil-like three-dimensional structure (Fig. 19). This microstructure is the result of the combustion reaction development, which involved the expansion of the sample (Fig. 15). After the preparation of $CaZrO_3$ by solution combustion synthesis, the next step was to investigate the sintering behavior of this powder. In this case, the main objective was to achieve a relative density as close to the

unit by sintering the $CaZrO_3$ green pellets below the melting temperature of Ni (1453 °C). This condition is imposed by the ceramic capacitor manufacturing technology, which involves the simultaneous sintering of $CaZrO_3$ and Ni [59]. The $CaZrO_3$ green pellets were uniaxial pressed at 200 MPa and then annealed at 1400 °C for 2 hours (Fig. 12), reaching 95 % of the theoretical density. Table 6 shows a comparison between the results of the sintering process reported hereby [25] and the results reported by other authors [57,66].
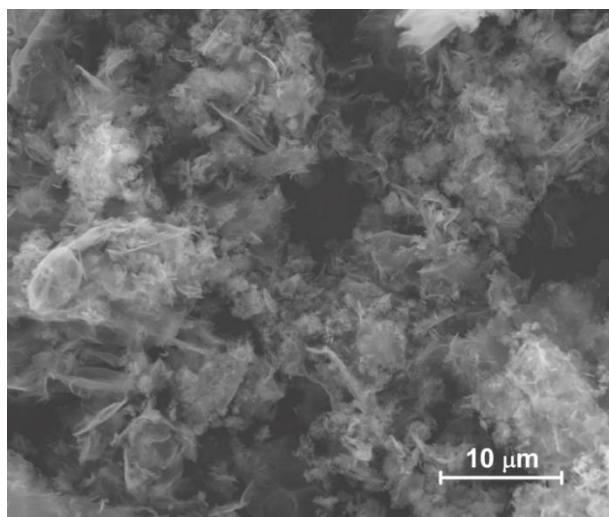
Fig. 19. SEM image of the powder prepared by solution combustion synthesis (sample 2).
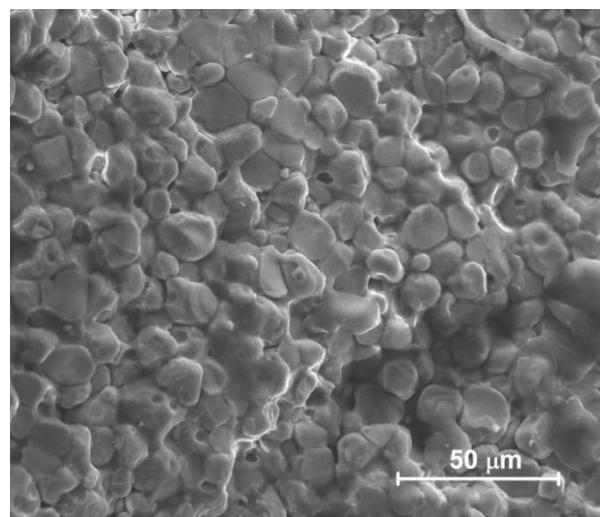
Fig. 20. SEM image of sample 2 after sintering at 1400 °C for 2 hours.

According to the literature data summarized in Table 6, $CaZrO_3$ powders prepared by the ceramic method are able to reach 95 % of the theoretical density only by performing the sintering stage at higher temperature (above 1550 °C) and using a much longer soaking time, more than 10 hours (Table 6). One should also consider that in the case of the ceramic method the preparation of $CaZrO_3$ powder requires additional heat treatments, whilst in the case of the combustion synthesis single-phase $CaZrO_3$ results directly from the combustion reaction.

Table 6. Comparison of the results reported hereby [25] with other results.

Synthesis method	Sintering conditions	Relative density (%)	Reference
Combustion synthesis	1400 °C / 2 h	95	[25]
Ceramic method	1600 °C / 12 h	>95	[57]
Ceramic method	1550 °C / 48 h	95	[66]

A more detailed analysis of sintered pellets revealed that the apparent porosity and water absorption are null, which indicates the absence of open pores. The visual inspection of the pellets showed they were slightly translucent, suggesting an advanced sintering stage. The microstructure of sample 2 after sintering at 1400 °C for 2 hours (Fig. 20) indicates that few closed pores exists and the size of the grains is less than 15 μm.

Key findings
- ✓ The formation of $CaZrO_3$ was investigated by using two different methods: solution combustion synthesis and the traditional ceramic method.

- ✓ In the case of the ceramic method – starting from a stoichiometric mixture of $Ca(NO_3)_2$ and ZrO_2 – a heat treatment of 1 hour at 1000 °C leads to the formation of several crystalline phases: $CaZrO_3$, CaO, ZrO_2 and CaO stabilized ZrO_2 solid solution. The formation of pure $CaZrO_3$ requires temperatures above 1000 °C. Due to the elevated temperature, the powder is highly agglomerated and has low surface area (1.4 m^2/g).

- ✓ Single-phase $CaZrO_3$ powder was prepared via solution combustion synthesis, by heating at 300 °C an aqueous solution of $Ca(NO_3)_2$, $ZrO(NO_3)_2$ and β-$C_3H_7NO_2$ (molar ratio = 3:3:4). As a result of the elevated self-generated temperature, pure $CaZrO_3$ resulted from the combustion reaction, so that no additional annealing was required.

- ✓ Although no advanced milling was performed, the as-prepared $CaZrO_3$ powder had large surface area (21.5 m^2/g) and small crystallite size (23.9 nm). The $CaZrO_3$ powder resulted from the combustion reaction was uniaxial pressed into pellets (200 MPa) and then sintered at 1400 °C for 2 hours, reaching 95 % of theoretical density.

- ✓ The excellent sintering behavior of $CaZrO_3$ powder prepared by solution combustion synthesis suggests that this method represents a rapid, cheap and economical solution for $CaZrO_3$ powder preparation.

2.1.1.3. Large surface area ZnAl$_2$O$_4$ powders prepared by combustion synthesis
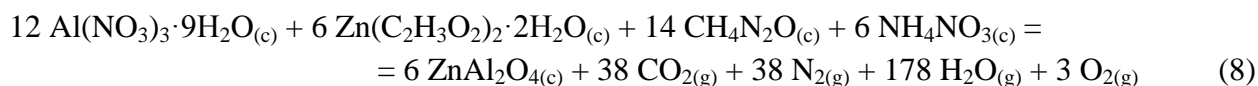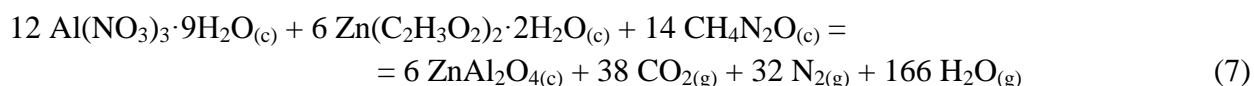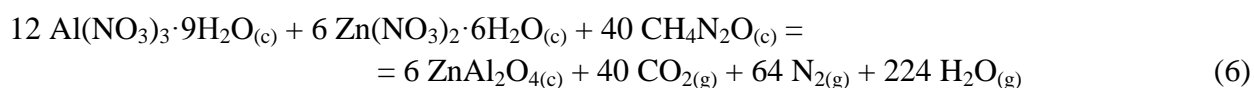
In order to prepare ZnAl$_2$O$_4$ powders with large surface via combustion synthesis, the combustion temperature must be decreased. From this point of view the candidate suggested an original combustion technique which relies on using zinc acetate instead of zinc nitrate [26]. This work was supported by a grant of the Romanian National Authority for Scientific Research, CNCS – UEFISCDI, project number PN-II-RU-TE-2011-3-0024 (18/05.10.2011). Properties of the resulted ZnAl$_2$O$_4$ powders were discussed in relation to the synthesis conditions, standard enthalpy of reaction and the total amount of gases released in each case. ZnAl$_2$O$_4$ powder resulted from the classical combustion synthesis (metal nitrates and urea) had larger crystallite size (23 nm) and small BET surface area (20 m^2/g), due to the large amount of heat (-10099 kJ/mol) released during the combustion reaction. The replacement of zinc nitrate by zinc acetate decreased the amount of heat released during the combustion reaction (-7743 kJ/mol), so that the resulted ZnAl$_2$O$_4$ powder had larger BET surface area (127 m^2/g) and smaller crystallite size (6 nm). The addition of NH$_4$NO$_3$ increased furthermore the BET surface area of ZnAl$_2$O$_4$ powder (201 m^2/g) as the volume of gases released during combustion increased. At the same time the ZnAl$_2$O$_4$ crystallite size decreased to 2 nm.

General context: zinc aluminate, ZnAl$_2$O$_4$, also named gahnite, is a rare mineral that belongs to the spinel group having a normal spinel structure. Zinc aluminate presents a unique combination of properties such are: high mechanical strength, high thermal and chemical stability, low sintering temperature, high quantum yields and excellent optical properties [74,75] with various applications. It is currently being used as optical material [76,77], high temperature material [78], catalysts and catalyst support [79-81].

Since the traditional ceramic process [81] leads to ZnAl$_2$O$_4$ powders with large particle size, many other techniques have been tested for the preparation of ZnAl$_2$O$_4$: hydrothermal synthesis [82-85], citrate [80], sol-gel [86-88], combustion synthesis [89,32], pyrolysis [90], co-precipitation [91] etc. The most common drawback of the ZnAl$_2$O$_4$ particles prepared by these methods is the low surface area, bellow 80 m^2/g. Therefore, the synthesis of ZnAl$_2$O$_4$ powders with large surface area is still an issue that needs to be addressed.

Among the above mentioned synthesis routes, solution combustion synthesis seems to be the most promising one, due to its simplicity, energy efficiency, environmentally friendliness and fast processing time. However, in order to benefit from all these advantages, the synthesis conditions must be properly selected. From this point of view, the candidate reports a modified combustion technique that enables the single-step formation of nanocrystalline ZnAl$_2$O$_4$ powders, with large BET surface area [26].

Experimental: three different ZnAl$_2$O$_4$ powders were prepared by solution combustion synthesis. Al(NO$_3$)$_3$·9H$_2$O (Merck), Zn(NO$_3$)$_2$·6H$_2$O (Merck), Zn(CH$_3$COO)$_2$·2H$_2$O (Merck), NH$_4$NO$_3$ (Reactivul Bucureşti) and urea – CH$_4$N$_2$O (Merck) were used as starting materials. Zinc acetate was used for the first time as fuel, as well as an alternate source of zinc oxide. The influence of ammonium nitrate (as pore generator) addition was also investigated. The recipes were calculated for obtaining 0.05 moles of ZnAl$_2$O$_4$. Considering the propellant chemistry, where the typical reactions byproducts are CO$_2$, N$_2$ and H$_2$O [1], the redox processes that are taking place during combustion reactions can be written according to equations (6-8):

$$12\ Al(NO_3)_3 \cdot 9H_2O_{(c)} + 6\ Zn(NO_3)_2 \cdot 6H_2O_{(c)} + 40\ CH_4N_2O_{(c)} =$$
$$= 6\ ZnAl_2O_{4(c)} + 40\ CO_{2(g)} + 64\ N_{2(g)} + 224\ H_2O_{(g)} \tag{6}$$

$$12\ Al(NO_3)_3 \cdot 9H_2O_{(c)} + 6\ Zn(C_2H_3O_2)_2 \cdot 2H_2O_{(c)} + 14\ CH_4N_2O_{(c)} =$$
$$= 6\ ZnAl_2O_{4(c)} + 38\ CO_{2(g)} + 32\ N_{2(g)} + 166\ H_2O_{(g)} \tag{7}$$

$$12\ Al(NO_3)_3 \cdot 9H_2O_{(c)} + 6\ Zn(C_2H_3O_2)_2 \cdot 2H_2O_{(c)} + 14\ CH_4N_2O_{(c)} + 6\ NH_4NO_{3(c)} =$$
$$= 6\ ZnAl_2O_{4(c)} + 38\ CO_{2(g)} + 38\ N_{2(g)} + 178\ H_2O_{(g)} + 3\ O_{2(g)} \tag{8}$$

After dosing and mixing the starting materials in 20 mL of distilled water, a clear aqueous solution was obtained. In order to trigger the ignition of the combustion reaction, the porcelain dish containing the precursor solution was placed inside an electric furnace preheated at 500 °C. As the temperature of the precursor solution increased, most of the water evaporated and an exothermic combustion reaction occurred. The time span between the appearance of the reaction front (ignition) and its disappearance was measured.

The resulted powders were hand-crushed with a pestle. The phase composition of the samples was established by X-ray diffraction, using a Rigaku Ultima IV diffractometer (CuK$_\alpha$ radiation) operating at 40 kV and 40 mA. The crystallite size was calculated by Scherrer's equation (1), using the PDXL 2.0 software. The lattice parameter was calculated based on the X-ray diffraction patterns, using equation (9) and the same hkl peaks (311 and 220) used for the crystallite size calculation:

$$a = d_{hkl}\left(h^2 + k^2 + l^2\right) \tag{9}$$

where: a is the lattice parameter (Å), d stands for the interplanar distance (Å), hkl are the Miller indices of the peaks (311 and 220).

Particle morphology was investigated by SEM, using a FEI Quanta FEG 250 electron microscope. The nitrogen adsorption-desorption isotherms were recorded using a Micromeritics ASAP 2020 instrument at 77 K, after the samples were degassed at 150 °C and 5 μmHg for 12 hours. The BET surface area, S_{BET}, was calculated using the Brunauer–Emmett–Teller (BET) method. Cumulative pore volume was computed using the Barrett–Joyner–Halenda (BJH) method from the desorption branch of the isotherms. The equivalent particle size was calculated based on the BET surface area (2), considering a theoretical density of $ZnAl_2O_4$ of 4.62 g/cm^3.

Results and discussion: usually in the case of $ZnAl_2O_4$ preparation via traditional combustion reaction [89], zinc and aluminum nitrates are used as oxidizing agents and urea is used as fuel (sample 1). Once the combustion reaction is ignited, the raw material mixture reaches incandescence that lasts for 15 seconds (Table 7). XRD analysis of sample 1 evidenced that the white powder resulted from the combustion reaction consist of a single crystalline phase, namely $ZnAl_2O_4$ (Fig. 21) having an average crystallite size of 23 nm (Table 7).

The lattice parameter (8.079 Å) is very close to the theoretical value of gahnite (8.084 Å) mentioned in the PDF file 05-0669. Since no additional annealing was performed, the formation of $ZnAl_2O_4$ nanocrystalline structure took place only on the expense on the self-generated heat during the combustion process. However, sample 1 had a BET surface area of only 20 m^2/g

(Table 7), which is quite small, especially for catalysis applications [89]. The most probable explanation for this result might be the large amount of heat released during combustion, as evidenced by the standard enthalpy of reaction.

Table 7. Characteristics of $ZnAl_2O_4$ samples prepared by combustion synthesis.

Sample number =>	1	2	3
Standard enthalpy of reaction (kJ/mol)	-10099	-7743	-8451
Released gases (moles of gas/mol of $ZnAl_2O_4$)	55	39	43
Combustion reaction duration (sec)	15	35	20
Crystallite size (nm)	23	6	2
Lattice parameter (Å)	8.079	8.090	8.080
Equivalent particle size (nm)	65	10	6
BET surface area (m^2/g)	20	127	201
Cumulative pore volume (cm^3/g)	0.04	0.17	0.20
Pore size (nm)	6	4	3

Based on the available thermodynamic data [71,72,92,93] and assuming that combustion reactions (1-3) are complete, the standard enthalpies of reaction were calculated (Table 7). The standard enthalpy of reaction calculated for reactions (6-8) indicate that combustion reaction 1 is the most exothermic one (-10099 kJ/mol). This result is in excellent agreement with the visual observations on combustion reaction evolution, which revealed that reaction 6 was the fastest (15 seconds). At the same time reaction 1 stands out as having the largest amount of gases released per mole of $ZnAl_2O_4$: 55 moles of gas/mol of $ZnAl_2O_4$ (Table 7). Obviously, there is a competition between the two parameters, which have an opposite influence on particle size and morphology. In the case of sample 1 the high exothermicity of the combustion reaction is the dominant factor, as the resulted $ZnAl_2O_4$ powder had the lowest BET surface area (20 m^2/g) and the largest crystallite size (23 nm) among all samples.
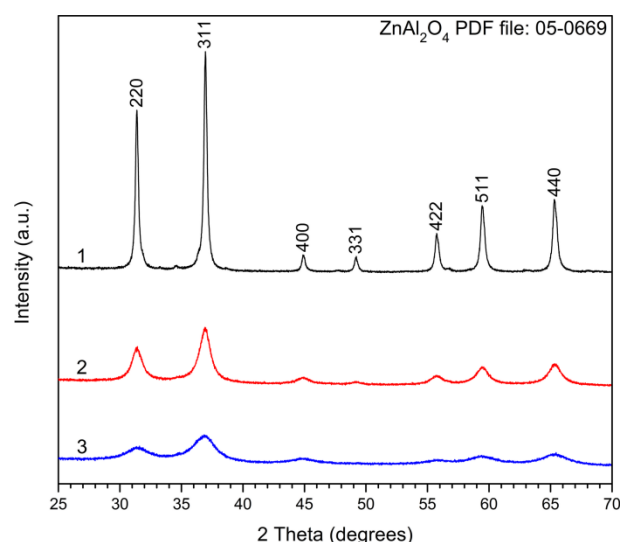

Fig. 21. XRD patterns of $ZnAl_2O_4$ powders prepared by combustion synthesis.

In order to decrease the amount of heat generated during the combustion process we suggest a modified combustion technique: $Zn(NO_3)_2$ (oxidizer) was replaced by $Zn(CH_3COO)_2$

(fuel) and the amount of urea was adjusted in order to keep the stoichiometric oxidizer/fuel ratio (sample 2). As far as we know this is the first time when such a solution is suggested. By comparison to sample 1, in the case of sample 2 the combustion reaction was less vigorous and lasted a little bit longer, yielding a white, more voluminous powder. XRD pattern of sample 2 is essentially identical to the one of sample 1, except the diffraction peaks are less intense and broader (Fig. 21), indicating smaller $ZnAl_2O_4$ crystallite size (Table 7). Also in this case, the lattice parameter (8.090 Å) is close to the theoretical value of gahnite (8.084 Å) mentioned in the PDF file 05-0669. In terms of crystallite size, sample 2 has $ZnAl_2O_4$ crystallites (6 nm) almost 4 times smaller than sample 1 (23 nm) due to the lower amount of heat generated during the combustion process (Table 7). By comparison to sample 1, the BET surface area of sample 2 increased by more than 6 times, up to 127 m^2/g (Table 7).

From the thermodynamic point of view, one can observe that the replacement of zinc nitrate by zinc acetate (sample 2) does decrease the heat released during the combustion reaction (-7743 kJ/mol), which is also reflected by a longer combustion reaction time (35 seconds). In the case of sample 2 the standard enthalpy of reaction is -7743 kJ/mol whilst the total amount of gases released is 39 moles of gas/mol of $ZnAl_2O_4$ (Table 7). By comparison to reaction 1, the amount of heat self-generated during the combustion reaction 7 was much lower, therefore the BET surface area of $ZnAl_2O_4$ powder increased whist the crystallite size decreased. This remarkable increase of the BET surface area corroborated with the decrease of the crystallite size suggests that the use of zinc acetate instead of zinc nitrate is an original, simple and efficient solution for increasing the surface area of $ZnAl_2O_4$ powders prepared by combustion synthesis.

Recipe 2 was furthermore enhanced, by adding NH_4NO_3 (pore generator) to the reaction mixture (sample 3). By comparison to sample 2, the presence of NH_4NO_3 accelerated the combustion reaction development, which lasted for 30 seconds (Table 7). At the same time, NH_4NO_3 increased the volume of generated gases, due to its decomposition to N_2, H_2O and O_2. As a result, the BET surface area of sample 3 (Fig. 22) increased to a staggering 201 m^2/g whilst the average $ZnAl_2O_4$ crystallite size decreased to 2 nm (Table 7). The lattice parameter of sample 3 is (8.080 Å) in exccellent agreement with the theoretical value of gahnite (8.084 Å) mentioned in the PDF file 05-0669.
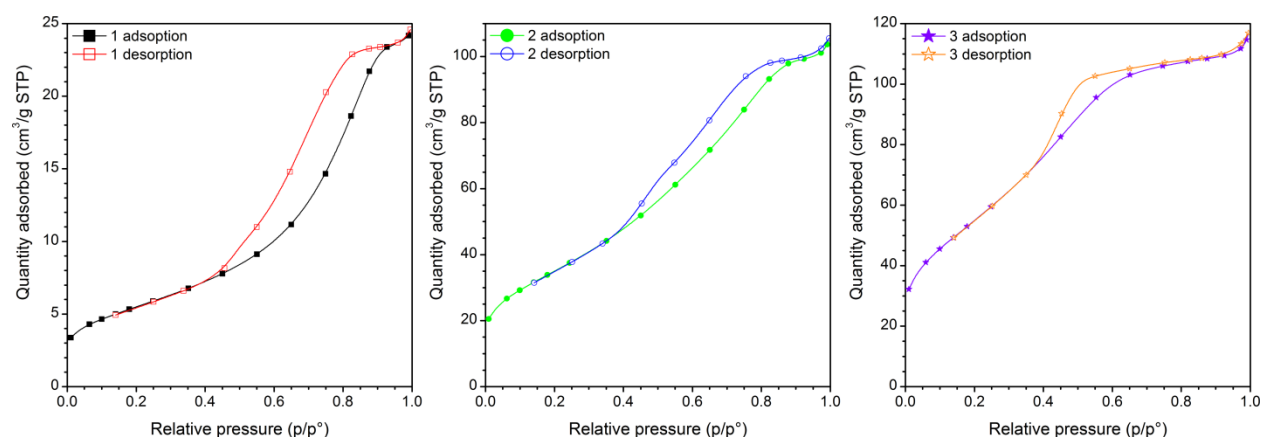

Fig. 22. Adsorption-desorption isotherms of combustion synthesized $ZnAl_2O_4$ powders.

The addition of NH_4NO_3 (sample 3) made the combustion process faster and more exothermic then reaction 2 (Table 7), as the standard enthalpy of reaction decreases to -8451 kJ/mol. Besides increasing the exothermic effect of the combustion process, NH_4NO_4 also

increases the total amount of released gases to 43 moles of gas/mol of $ZnAl_2O_4$ (Table 7). Considering that the $ZnAl_2O_4$ powder prepared by reaction 8 has the largest BET surface area (201 m^2/g) and the smallest crystallite size (2 nm) one can conclude that in this case, the larger amount of gases released during the combustion reaction is the dominant factor influencing the powder properties.

SEM images of sample 3 (Fig. 23) revealed the presence of relatively large and porous structures of primary nanometric particles. This kind of morphology, typical for combustion synthesized powders, is due to the large volume of gases evolving during combustion reaction and the high temperature developed within the reaction mixture. Higher magnification evidenced that the $ZnAl_2O_4$ structures are also agglomerated, have a plate-like shape and are larger than 1 micron. The equivalent particle size calculated from the BET surface area of $ZnAl_2O_4$ powders ranges between 6 and 65 nm, as indicated in Table 7. For the same sample, the equivalent particle size is larger than the crystallite size calculated from the XRD patterns, which indicates that the particles are polycrystalline.
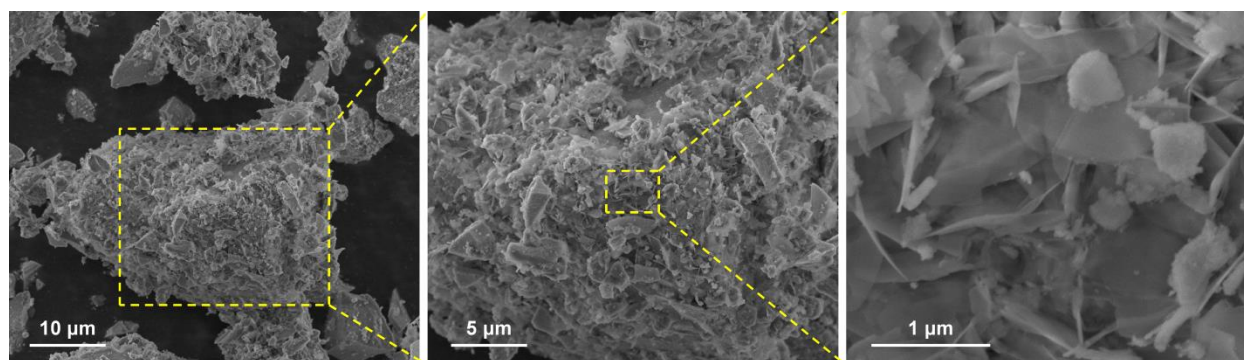
Fig. 23. SEM images of sample 3.

In the case of sample 1 the profile of the isotherm (Fig. 22) is very similar to one reported by Alves et al. [89], who also prepared $ZnAl_2O_4$ by combustion synthesis starting from metal nitrates and urea. According IUPAC classification, all samples have a type IV isotherm and H2 hysteresis (Fig. 22), which are typical for mesoporous materials having a complex structure [89,94]. The pore size measurements confirm that the three samples are indeed mesoporous materials. The pore size decreased from sample 1 (6 nm) to sample 2 (4 nm) and then to sample 3 (3 nm), whilst the cumulative pore volume increased in the same order (Table 7).

With respect to the potential applications of zinc aluminate, Farhadi and Panahandehjoo tested the catalytic activity of $ZnAl_2O_4$ powders with different BET surface areas (58 – 230 m^2/g) and concluded that large surface area had a positive effect on the catalytic activity, as the reaction time decreased in the case of high surface area $ZnAl_2O_4$ [95]. Taking into account the properties of the $ZnAl_2O_4$ powder prepared by the modified combustion technique (large surface area, small crystallite size and small pore size) one can assume that this powder might have a superior catalytic activity.

Key findings
- ✓ $ZnAl_2O_4$ powders with large surface area have been prepared in a single step procedure (without subsequent annealing), using an original combustion technique, which relies on using zinc acetate instead of zinc nitrate.

✓ Due to the large amount of heat (-10099 kJ/mol) released during the classical version of the combustion reaction (aluminum nitrate + zinc nitrate + urea) the resulted $ZnAl_2O_4$ powder had a small BET surface area (20 m^2/g) and an average crystallite size of 23 nm.

✓ The replacement of zinc nitrate by zinc acetate decreased the amount of heat released during the combustion reaction (-7743 kJ/mol), so that the resulted $ZnAl_2O_4$ powder had larger BET surface area (127 m^2/g) and smaller crystallites (6 nm).

✓ The addition of NH_4NO_3 increased furthermore the BET surface area of $ZnAl_2O_4$ powder (201 m^2/g) as the volume of gases released during combustion reaction increased. At the same time the average crystallite size decreased to 2 nm.

2.1.1.4. Fine tuning of $CoFe_2O_4$ properties prepared by solution combustion synthesis

Another possibility to decrease the combustion temperature is the use of oxalic acid, which acts as a retarding agent. For instance, single phase $CoFe_2O_4$ powders were prepared by solution combustion synthesis using β-alanine as fuel [30]. This work was supported by the Sectoral Operational Programme Human Resources Development, financed from the European Social Fund and by the Romanian Government under the contract number POSDRU/86/1.2/S/58146 (MASTERMAT). By adding to the reaction mixture various amounts of oxalic acid, which acts as a retarding agent and pore generator, properties of $CoFe_2O_4$ powders can be properly adjusted [30]. Depending on the amount of oxalic acid, the average crystallite size of $CoFe_2O_4$ ranges between 13 and 41 nm, whilst the specific surface area varies between 1.8 and 34.4 m^2/g. The combustion synthesized $CoFe_2O_4$ powders exhibit a hard ferimagnetic behavior. The $CoFe_2O_4$ coercivity varies between 71.8 and 126.0 kA/m and the saturation magnetization ranges between 53.0 and 70.6 emu/g. After pressing and sintering at 1400 °C for 4 hours, the pellets reached up to 90 % of the $CoFe_2O_4$ theoretical density.

General context: cobalt ferrite, $CoFe_2O_4$, has an inverse spinel structure and it is an important material that has exceptional magnetic, optical and electrical properties, exploited in various applications, such as: catalysis [96-98], adsorption and separation [96], microwave absorbers [97,98], photonic and electronic devices [98-100], ferrofluid technology [98,101-103], magnetocaloric refrigeration [101,102], medical diagnosis [101-104], drug delivery [102-104], magnetocytolysis [103,104], hyperthermia [98], permanent magnets [97], sensors [97].

Generally, the magnetic properties of cobalt ferrite namely coercivity, anisotropy and saturation magnetization, are highly dependent on several parameters, amongst which the preparation method is probably the most important. Therefore, by properly selecting the synthesis route one can obtain $CoFe_2O_4$ powders with high/moderate coercivity and high/moderate saturation magnetization, according to the desired applications [96,97,100,101,105]. Alongside the co-precipitation method [97,106] many other preparation routes have been reported for $CoFe_2O_4$ preparation: hydrothermal and solvothermal method [98,99], microemulsion technique [102,107], reverse micelles [104], Massart [108], sonochemical method [109], sol-gel [110], organic precursors [111] etc.

Although it has been reported that combustion synthesis has a great potential in the preparation of metal oxide nanopowders, little attention has been paid to the preparation of $CoFe_2O_4$. In a recent review on combustion synthesis of spinel-type ferrite nanomaterials, Sutka and Mezinskis [112] reported that the most popular fuels tested for combustion synthesis of $CoFe_2O_4$ are urea [100], glycine [101,113] and citric acid [105,114,115].

Experimental: based on combustion reaction (10) stoichiometric amounts of $Co(NO_3)_2 \cdot 6H_2O$ (Fluka), $Fe(NO_3)_3 \cdot 9H_2O$ (Roth) and $C_3H_7NO_2$ (β-alanine, Fluka) were dissolved in 15 mL of hot distilled water, according to the working procedure shown in Fig. 24.

$$3\ Co(NO_3)_2 + 6\ Fe(NO_3)_3 + 8\ C_3H_7NO_2 = 3\ CoFe_2O_4 + 24\ CO_2 + 28\ H_2O + 16\ N_2 \qquad (10)$$

Recipes were designed assuming a yield of 0.03 moles of $CoFe_2O_4$. Various amounts of $C_2H_2O_4$ (oxalic acid, Chimreactiv) were added to the reaction mixture in different proportions (0 – 175 % wt.), in order to investigate its influence on the cobalt ferrite properties.
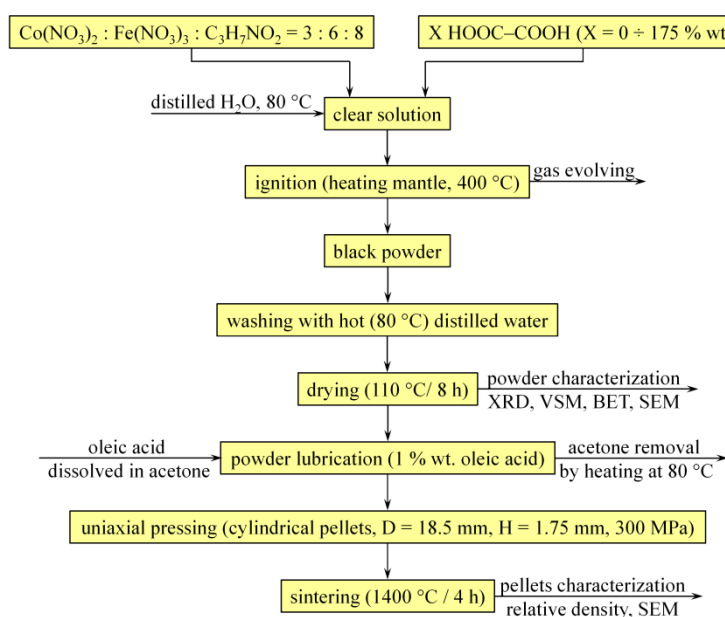
Fig. 24. Flowchart of the aqueous combustion synthesis and characterization of $CoFe_2O_4$.

The addition amount was calculated with respect to $CoFe_2O_4$. The resulting aqueous solution was placed inside a preheated heating mantle (400 °C). As water evaporated, combustion reaction took place leading to the formation of a fluffy black powder, which was hand-grinded, washed with distilled water and dried at 110 °C.

Phase composition of the powders was determined by X-ray diffraction (XRD) using a Rigaku ULTIMA IV diffractometer (monochromated $Cu_{K\alpha}$ radiation - 0.15406 nm). The average crystallite size (D_{XRD}) was calculated based on the XRD patterns using the PDXL 2 software. BET (Brunauer–Emmett–Teller) surface area of the powders, S_{BET}, was measured by nitrogen gas adsorption technique using a Micromeritics ASAP 2020 instrument. BJH (Barrett–Joyner–Halenda) cumulative volume of pores, V_{BJH}, was calculated from the adsorption isotherm.

Assuming that $CoFe_2O_4$ particles have a spherical shape, the equivalent diameter, D_{BET}, was calculated using equation (2), considering a theoretical density of 5.3 g/cm^3. Magnetic properties were measured at room temperature by vibrating sample magnetometry, using a VSM 880 ADE/DMS magnetometer. Combustion synthesized powders were lubricated with 1 % wt. of oleic acid, pressed into cylindrical pellets (1.75 mm height x 18.5 mm diameter) and then sintered at 1400 °C for 4 hours (Fig. 24). Relative density of the sintered pellets was determined by Archimedes technique. Morphology and elemental analysis of $CoFe_2O_4$ powders/sintered pellets were investigated by scanning electron microscopy (SEM) and energy dispersive X-ray analysis (EDAX), using a FEI Inspect S instrument.

Results and discussion: the evolution of the combustion reactions – present in all the 5 recipes – is highly influenced by the proportion of oxalic acid addition. Practically, increasing the oxalic acid addition leads to longer reaction periods (Table 8). The higher the addition amount, the more obvious this effect is. In the case of samples 4 and 5 this is directly correlated with the lack of incandescence during combustion reactions.

As a result, one can say that the oxalic acid addition results in a reduction of the combustion reaction intensity. Thus, the combustion reaction evolution gradually moves from a strong incandescence process, which is accompanied by flames (sample 1) to a smoldering process, where no flames or incandescence appeared (sample 5).

Table 8. Characteristics of combustion synthesized $CoFe_2O_4$ powders.

Sample no.	$C_2H_2O_4$ (wt. %)	Reaction time (s)	D_{XRD} (nm)	a (Å)	S_{BET} (m^2/g)	D_{BET} (nm)	M_s (emu/g)	H_c (kA/m)
1.	0	20	41	8.385	1.8	629	66.6	103.7
2.	50	45	31	8.387	2.1	539	70.6	126.0
3.	100	50	22	8.372	6.5	174	63.5	118.2
4.	150	80	18	8.386	20.0	57	53.1	109.1
5.	175	120	13	8.387	34.4	33	53.0	71.8

For example, in Fig. 25 are shown some images taken during the combustion reactions of the samples 1 and 5.

Fig. 25. Images taken during the combustion reactions of samples 1 and 5.

XRD patterns of the samples resulted from all the combustion reactions indicate $CoFe_2O_4$ as the single crystalline phase (Fig. 26). The unit cell parameter varies between 8.372 and 8.387 Å, which is very close to the theoretical value of $CoFe_2O_4$ (8.3919 Å) mentioned in the PDF file 22-1086. The average crystallite size of $CoFe_2O_4$ ranges between 13 and 41 nm, which indicates the nanocrystalline feature of combustion synthesized $CoFe_2O_4$.
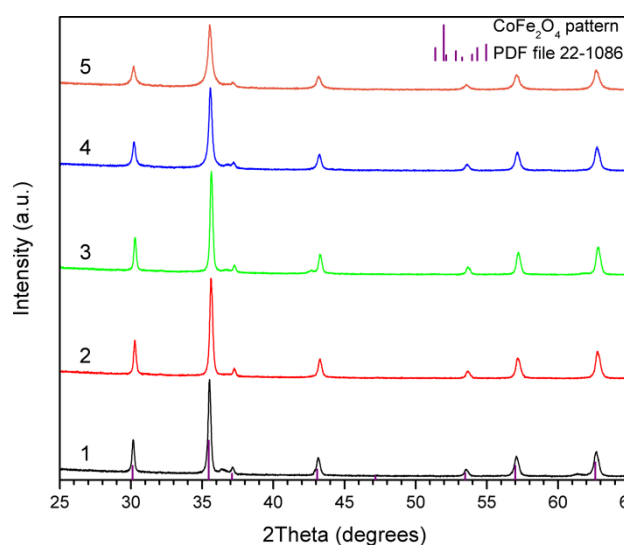

Fig. 26. XRD patterns of samples 1-5, prepared by solution combustion synthesis.

Analyzing the influence of the oxalic acid addition on the $CoFe_2O_4$ crystallite size, one can notice that the crystallite size decreases with increasing the oxalic acid amount (Table 8). This evolution may be assigned on one hand to the decrease of the maximum temperature achieved during the combustion reaction and on the other hand to the increase of the gas volume evolved during the reaction, which hinders the crystallite growth.

The adsorption-desorption isotherms of $CoFe_2O_4$ powders prepared by combustion synthesis are shown in Fig. 27. According to IUPAC classification, the samples show Type IV isotherms with H3 hysteresis, which suggests the presence of fragile porous particle agglomerations. Depending on the amount of oxalic acid added to the reaction mixture, the BET surface area of the powders varies between 1.8 and 34.4 m^2/g.
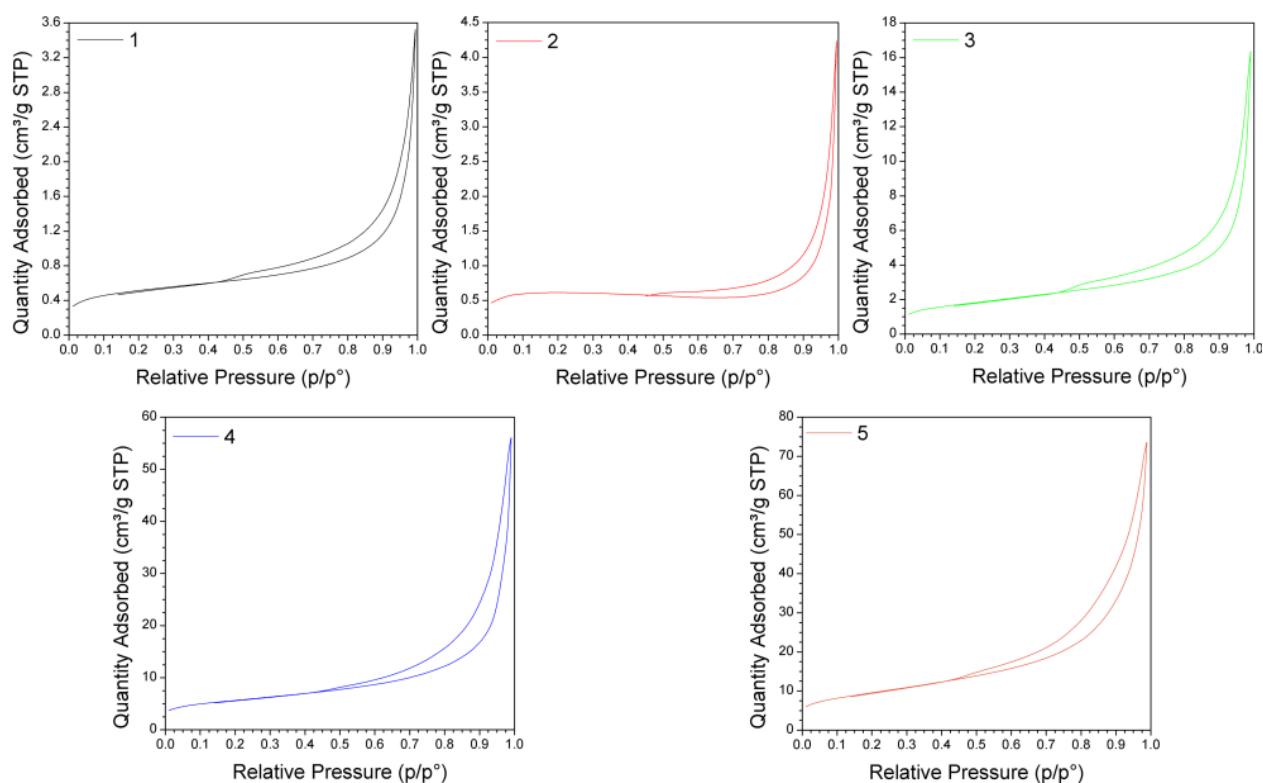

Fig. 27. Adsorbtion-desorbtion isotherms of samples 1-5.

Basically, increasing the oxalic acid addition leads to increased BET surface area and smaller crystallite size (Table 8). This evolution confirms the pore generator role of the oxalic acid, but also the mechanism that makes this possible: lowering the combustion temperature and increasing the volume of the evolved gases.

One may notice that the equivalent particle size, D_{BET}, calculated from the BET surface area is larger than the crystallite size, D_{XRD}, calculated from the XRD patterns (Table 8). This indicates that the resulted $CoFe_2O_4$ particles are not single crystals, but they contain several crystallites, are polycrystalline, as confirmed by the SEM images of the samples. The pore generator function of the oxalic acid may also be noticed from the evolution of the cumulative pore volume, calculated based on the adsorption isotherm using the BJH method (Fig. 28).

There is a direct correlation between the oxalic acid addition and pore volume: the higher the oxalic acid amount, the higher the pore volume. Thus, sample 5 prepared with 175 % oxalic acid has a cumulative pore volume more than 22 times higher than sample 1 prepared with no oxalic acid addition. The evolution of BET surface area and cumulative pore volume as a

function of the oxalic acid addition is also confirmed by the SEM images presented for samples 1, 2 and 5 (Fig. 29).
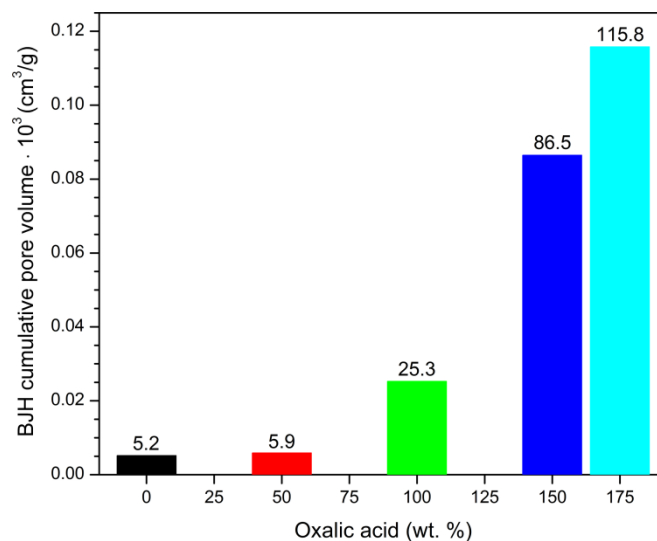

Fig. 28. The evolution of BJH cumulative pore volume as a function of the oxalic acid addition.

One may notice that in each case the particles are associated in agglomerations smaller than 40 μm, which is in accordance to the type H3 hysteresis shown by the adsorption-desorption isotherms (Fig. 29). In the case of sample 1, prepared without oxalic acid, the grain porosity is rather small, as already confirmed by the nitrogen adsorption-desorption investigations. By comparison, sample 2 prepared with 50 % oxalic acid addition, exhibits a clearly porous hollowly structure. Increasing the addition amount up to 175 % makes the $CoFe_2O_4$ morphology extremely loose, which is related to the large BET surface area of sample 5. The SEM images presented in Fig. 29 illustrate the increase of $CoFe_2O_4$ porosity with increasing the oxalic acid addition (sample $1 \rightarrow 2 \rightarrow 5$), which is also confirmed by the nitrogen adsorption-desorption investigations (Table 8).
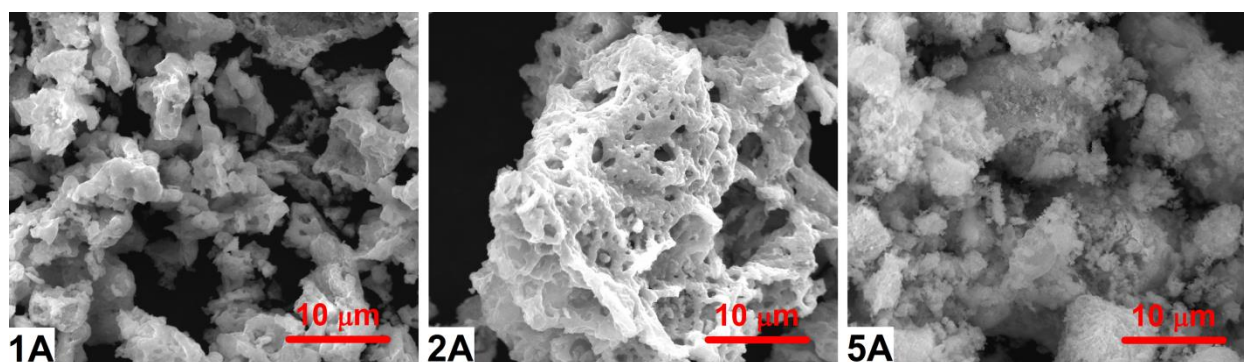
Fig. 29. SEM images of samples 1, 2 and 5.

Energy dispersive X-ray analysis (EDAX) of samples 1, 2 and 5 evidenced Co, Fe and O as the only present elements. Considering the method accuracy, the elemental composition of samples 1 (16.3 % Co, 31.3 % Fe, 52.5 % O), 2 (12.4 % Co, 25.3 % Fe, 62.3 % O) and 5 (13.2 % Co, 26.0 % Fe, 60.8 % O), expressed in atomic percents, is close to the theoretical composition of $CoFe_2O_4$ (14.3 % Co, 28.6 % Fe, 57.1 % O). These results are very well correlated to the XRD patterns (Fig. 26) of the samples showing $CoFe_2O_4$ as the single phase.

The magnetic hysteresis curves of the samples obtained from the combustion reactions are presented in Fig. 30. One may notice that none of the samples reach the saturation magnetization in the applied range of magnetic field. Therefore, the saturation magnetization was calculated by plotting M as a function of 1/H, followed by the extrapolation of the magnetic curve at the magnitude of M, when $H \rightarrow \infty$ ($1/H \rightarrow 0$). The saturation magnetization of $CoFe_2O_4$ powders calculated by this method ranges between 53.0 and 70.6 emu/g (Table 8).

Fig. 30. Magnetic hysteresis curves of solution combustion synthesized $CoFe_2O_4$ powders.
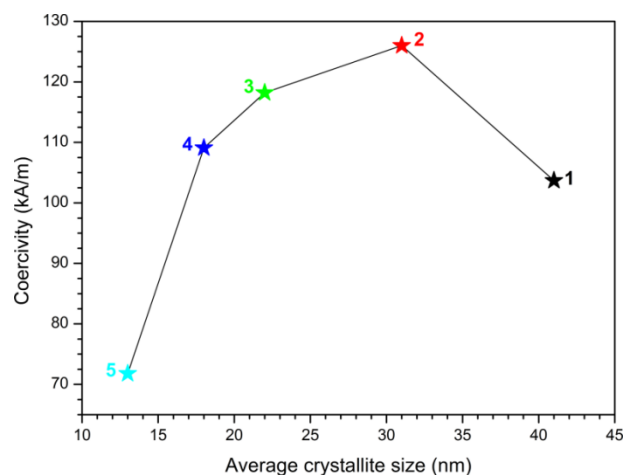
Fig. 31. The evolution of coercivity of $CoFe_2O_4$ powders as a function of crystallite size.

The coercivity of $CoFe_2O_4$ powders ranges between 71.8 and 126.0 kA/m, which indicates a hard ferrimagnetic character. The coercivity evolution as a function of the crystallite s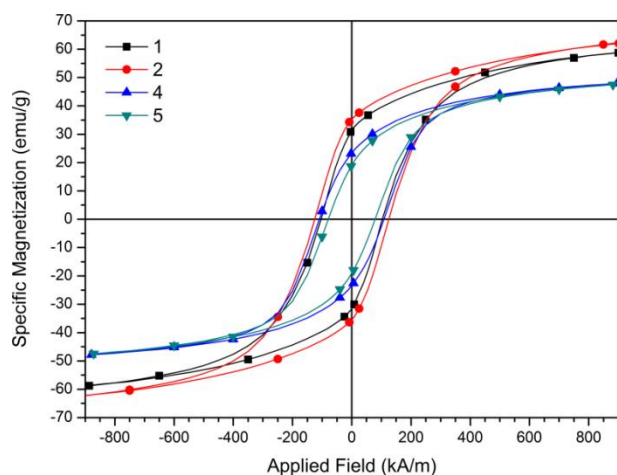ize (Fig. 31) is similar to the one reported by other authors [115,116]: coercivity increases with the increase of the crystallite size up to a maximum value of 126.0 kA/m, which corresponds to a crystallite size of 31 nm.

The coercivity of $CoFe_2O_4$ powders decreases for larger crystallites due to the multidomenial character of the grains, surface anisotropy and thermal energies [115,116]. However, for the same crystallite size the $CoFe_2O_4$ coercivity values reported in this paper are higher, which translates into enhanced magnetic properties. Making a comparison between our results [30] and those obtained by other authors using combustion synthesis (Table 9), one may notice that the solution of using β-alanine and oxalic acid addition allows the adjustment of crystallite size, surface area and magnetic properties of $CoFe_2O_4$ in a wide range.

Table 9. Comparative presentation of $CoFe_2O_4$ characteristics obtained in this study [30] with respect to other results reported for the same preparation route.

Fuel	D_{XRD} (nm)	H_c (kA/m)	M_s (emu/g)
β-alanine (this study) [30]	13-41	71.8-126.0	53.0-70.6
Urea [100]	66	50	-
Glycine [101]	38	7	76
Glycine [113]	37	84	45
Citric acid [114]	22	83	41
Citric acid [115]	15	97	67
Citric acid [105]	23	60	9

The coercivity value of $CoFe_2O_4$ powders prepared in this study should be especially highlighted, as it is much higher than the one of $CoFe_2O_4$ powders obtained via combustion method using other fuels: urea, glycine or citric acid [100,101,105,113-115].

The relative density of the pellets sintered at 1400 °C for 4 hours varies between 86 and 90 % of the theoretical density (Fig. 32). One may notice that the relative density of the samples decreases with the increase of BET surface area. This phenomenon is even more prominent in the case of samples 4 and 5 – which show the highest BET surface area. This behavior suggests that the main challenge in achieving a good compactness after sintering is to obtain high-density green pellets in the first place.
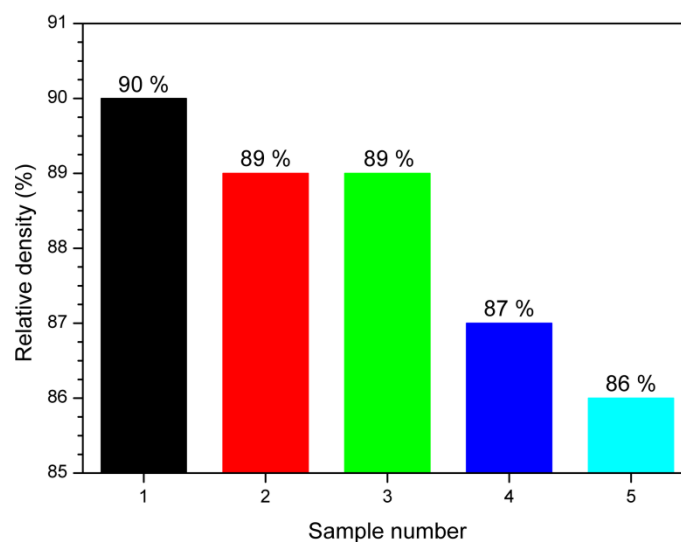
Fig. 32. Relative density of samples 1-5 sintered at 1400 °C for 4 hours.

Taking this into account, one may expect to achieve improved results when using isostatic pressing rather than uniaxial pressing. The SEM images (Fig. 33) of sample 2 sintered at 1400 °C for 4 hours reveal the presence of the interconnected grains, smaller than 10 μm, and also the residual pores located at the grain boundaries.
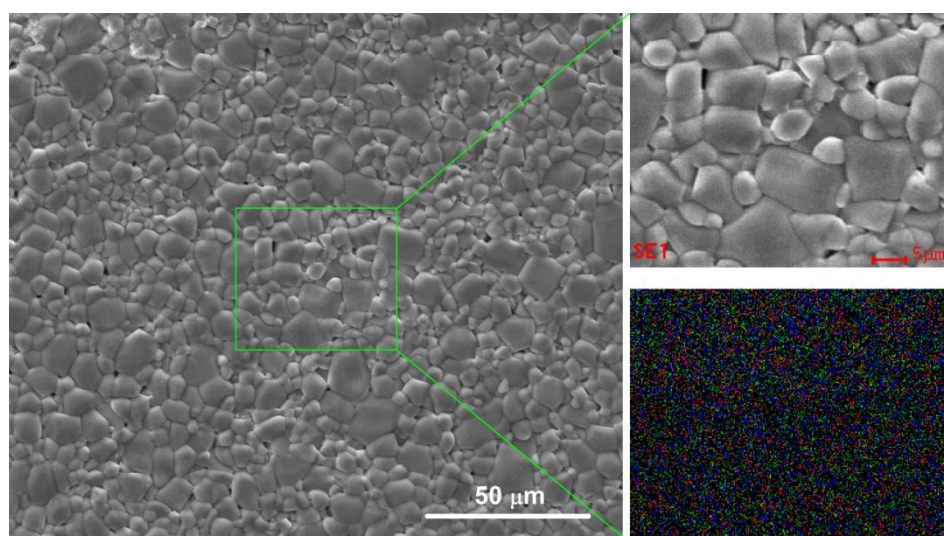
Fig. 33. SEM image and elements distribution (Co – blue, Fe – green, O – red) for sample 2, sintered at 1400 °C for 4 hours.

These observations are in agreement with the relative density of sample 2 (89 % of the theoretical density). After sintering, the elemental composition of sample 2 (15.1 at. % Co, 31.3 at. % Fe and 53.6 at. % O) is very close to the theoretical composition of $CoFe_2O_4$. One may also notice the homogeneous distribution of cobalt, iron and oxygen in the sintered sample.

Key findings

- ✓ Single phase $CoFe_2O_4$ powders were prepared by solution combustion synthesis, without any annealing step, using β-alanine as fuel.
- ✓ Properties of the resulted $CoFe_2O_4$ powders may be adjusted by adding various amounts of oxalic acid, which acts as a retarding agent (decreasing the combustion temperature) and pore generator.
- ✓ Depending on the amount of oxalic acid, the average crystallite size of $CoFe_2O_4$ ranges between 13 and 41 nm, whilst the BET surface area varies between 1.8 and 34.4 m^2/g.
- ✓ The combustion synthesized $CoFe_2O_4$ powders exhibit a hard ferrimagnetic behavior, having a coercivity that ranges between 71.8 and 126.0 kA/m. The saturation magnetization varies between 53.0 and 70.6 emu/g.
- ✓ After hydraulic uniaxial pressing and sintering at 1400 °C for 4 hours, the pellets reached relative densities up to 90 % of the $CoFe_2O_4$ theoretical density.
- ✓ The superior magnetic properties of the $CoFe_2O_4$ powders obtained directly from the combustion reaction (with no subsequent annealing), as well as their sintering behavior represent strong arguments for using the combustion method in the synthesis of $CoFe_2O_4$ powders with tailored properties.

2.1.1.5. Highly sinterable cobalt ferrite particles prepared by combustion synthesis

In an attempt to prepare $CoFe_2O_4$ powders having larger surface area (which requires lower combustion temperature) and a better sintering behavior, the candidate suggested a modified solution combustion synthesis, starting from a stoichiometric mixture of cobalt acetate (instead of cobalt nitrate), iron nitrate and 5-aminotetrazole [31]. The resulted cobalt ferrite powder had large surface area (44 m^2/g), small crystallite size (11 nm) and a saturation magnetization of 38.9 Am^2/kg. $CoFe_2O_4$ pellets sintered at 1100 °C for 2 hours developed a fine compact microstructure, reaching 99 % of the theoretical density. After sintering, the saturation magnetization increased to 71.3 Am^2/kg whilst the coercivity decreased to 21.8 kA/m.

General context: $CoFe_2O_4$, has been and still is one of the most interesting ferrimagnetic materials, which is used in a wide variety of applications in the fields of medicine, engineering and technology [117-119]. For many of these applications, such as the manufacturing of magnetostrictive sensors, actuators and permanent magnets, highly sinterable $CoFe_2O_4$ powders are required [120,121]. Therefore, efforts have been carried out to prepare single-phase $CoFe_2O_4$ particles that have not only suitable magnetic properties but also better sintering behavior. $CoFe_2O_4$ has been synthesized by various methods: ceramic method [122,123], coprecipitation [124], sol-gel [125], mechanical alloying [126], combustion synthesis [30,127,128], citrate [128].

However, most of the $CoFe_2O_4$ powders prepared by these routes have often low surface area and are difficult to sinter, as elevated temperature and long soaking times are required. For instance, Rafferty et al. [129] reported a non-isothermal two-step sintering procedure (6 hours at 1310 ºC followed by 3 more hours at 1500 ºC) which produced $CoFe_2O_4$ discs having a relative density of approximately 96 %. Nlebedim et al. [130] found that the $CoFe_2O_4$ pellets sintered in vacuum at 1200 ºC for 24 hours reached almost 97 % of the theoretical density, but they also developed a detrimental secondary phase. Mohaidee and Joy [127] prepared by the traditional combustion synthesis (cobalt nitrate, iron nitrate and glycine) a 4 nm particle size $CoFe_2O_4$. However, after sintering for 2 hours at 1450 ºC the cobalt ferrite specimen had reached only 85 % of the theoretical density.

Experimental: 0.03 moles of cobalt acetate tetrahydrate – $Co(CH_3COO)_2 \cdot 4H_2O$ (Reactivul, 99 %), 0.06 moles of iron nitrate nonahydrate – $Fe(NO_3)_3 \cdot 9H_2O$ (Merck, 99 %) and 0.06 moles of 5-aminotetrazole monohydrate – $CH_3N_5 \cdot H_2O$ (Sigma Aldrich, 97 %) were dissolved in 30 mL of hot distilled water in a porcelain evaporating dish.

The clear solution was placed inside a heating mantle, preheated at 400 °C. As the temperature of the solution increased, an exothermic self-propagating combustion reaction occurred (reaction 11), yielding in a matter of seconds a voluminous black powder (sample 1). The obtained sample was hand-grinded, washed with distilled water and dried at 110 °C.

$$CoC_4H_6O_4 + 2\ Fe(NO_3)_3 + 2\ CH_3N_5 = CoFe_2O_4 + 6\ CO_2 + 6\ H_2O + 8\ N_2 \qquad (11)$$
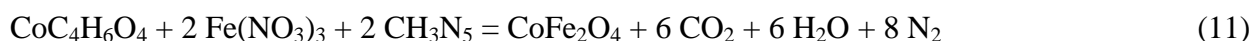
XRD analysis (Rigaku ULTIMA IV diffractometer, $Cu_{K\alpha}$ radiation – 1.5406 Å) was used to determine the phase composition of the samples. The average crystallite size, D_{XRD}, and the lattice parameter, a, were calculated based on the diffraction patterns, using the instrument-integrated PDXL 2.0 software (whole pattern profile fitting method). The instrumental broadening was subtracting from the measured XRD patterns using a Si standard.

BET (Brunauer–Emmett–Teller) surface area of the powder, S_{BET}, was measured by nitrogen gas adsorption technique using a Micromeritics ASAP 2020 instrument. BJH (Barrett–Joyner–Halenda) cumulative volume of pores, V_{BJH}, was calculated from the desorption branch of the isotherm. The powder resulted from the combustion reaction was lubricated with 3 % weight of oleic acid, pressed (300 MPa) into cylindrical pellets (18.5 mm diameter x 1.5 mm height) and sintered at 1100 °C for 2 hours (sample 2).

Relative density of the sintered pellets was determined by Archimedes technique. Particle size and morphology as well as elemental analysis were investigated by SEM-EDX, using a FEI Quanta FEG 250 instrument. Vibrating sample magnetometry (VSM 880 ADE/DMS magnetometer) was used to investigate the magnetic properties of the samples at room temperature.

Results and discussion: XRD analysis indicated that the black powder resulted from the combustion reaction (sample 1) consists of single-phase $CoFe_2O_4$ having a face-centered cubic structure (Fig. 34). The lattice parameter (a = 0.839 nm) calculated from the XRD pattern was in excellent agreement with the value mentioned in the PDF file 22-1086 (a = 0.839 nm). $CoFe_2O_4$ particles prepared by combustion synthesis had an average crystallite size of 11 nm.
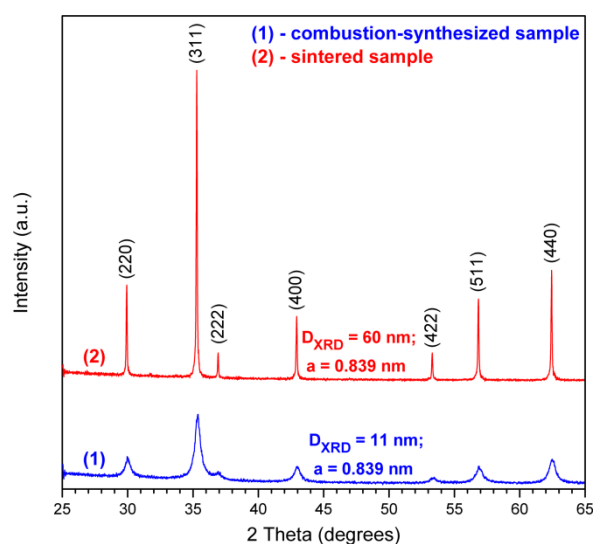
Fig. 34. XRD patterns of the combustion--synthesized powder (sample 1) and of the sintered sample (sample 2).
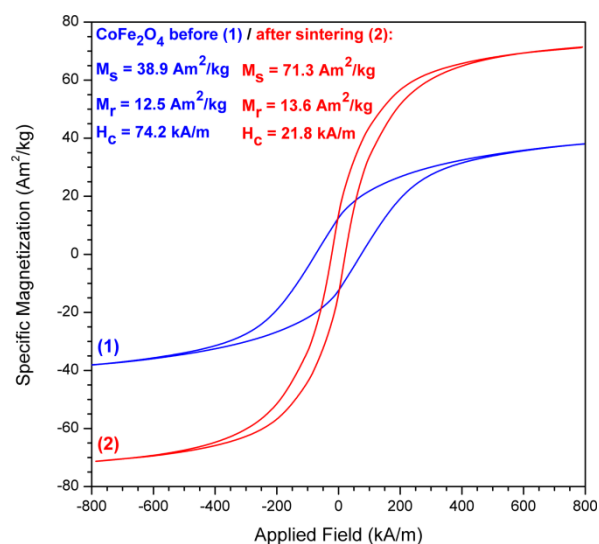
Fig. 35. Magnetic hysteresis loops of the combustion-synthesized powder (sample 1) and of the sintered sample (sample 2).

EDX analysis revealed that the combustion-synthesized powder is carbon free and nitrogen free, which confirms that the powder is not contaminated with organic residues − an essential requirement for achieving an advanced sintering degree. The elemental composition of as-prepared $CoFe_2O_4$ powder (14.1 at. % Co, 28.2 at. % Fe, 57.7 at. % O) is very close to the theoretical composition of pure $CoFe_2O_4$ (14.3 at. % Co, 28.6 at. % Fe, 57.1 at. % O), which is consistent with the XRD results.

The saturation magnetization of $CoFe_2O_4$ particles (M_s = 38.9 Am^2/kg) (Fig. 35) was lower than the one of bulk $CoFe_2O_4$, 74.08 Am^2/kg [131], which can be explained by the small size of $CoFe_2O_4$ particles [132] and the surface effects that are aroused by the distortion of the magnetic moments at the surface of nanoparticles [133]. The as-prepared powder (sample 1) had a remanent magnetization, M_r, of 12.5 Am^2/kg, and a coercivity, H_c, of 74.2 kA/m.

N_2 adsorption-desorption isotherm (Fig. 36) indicated that $CoFe_2O_4$ powder (sample 1) exhibits a type IV isotherm with H3 hysteresis, having a BET surface area, S_{BET}, of 44 m²/g. The equivalent particle size (D_{BET} = 26 nm), calculated from the BET surface area, was approximately two times larger than the crystallite size, which indicates that $CoFe_2O_4$ particles are polycrystalline.
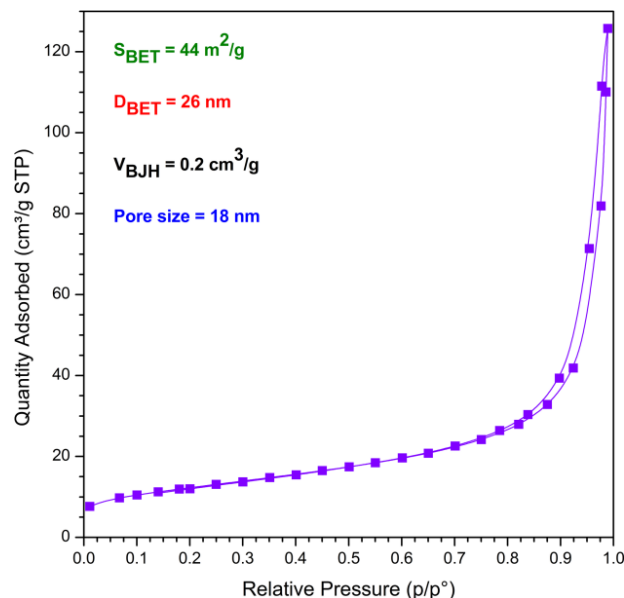
Fig. 36. N_2 adsorption-desorption isotherm of combustion-synthesized $CoFe_2O_4$ (sample 1).

The SEM image revealed the $CoFe_2O_4$ powder (sample 1) had a very porous, foamy structure (Fig. 37AB), which might be the result of the large volume of gases (20 moles of gas / mole of $CoFe_2O_4$) released during the combustion reaction (1). This particular kind of morphology is consistent with the large cumulative pore volume (V_{BJH} = 0.2 cm³/g) (Fig. 36). The average pore size (18 nm) places the as-prepared cobalt ferrite in the group of mesoporous materials. At the same time, Fig. 37A shows the presence of several agglomerates, which supports the idea of polycrystalline particles.
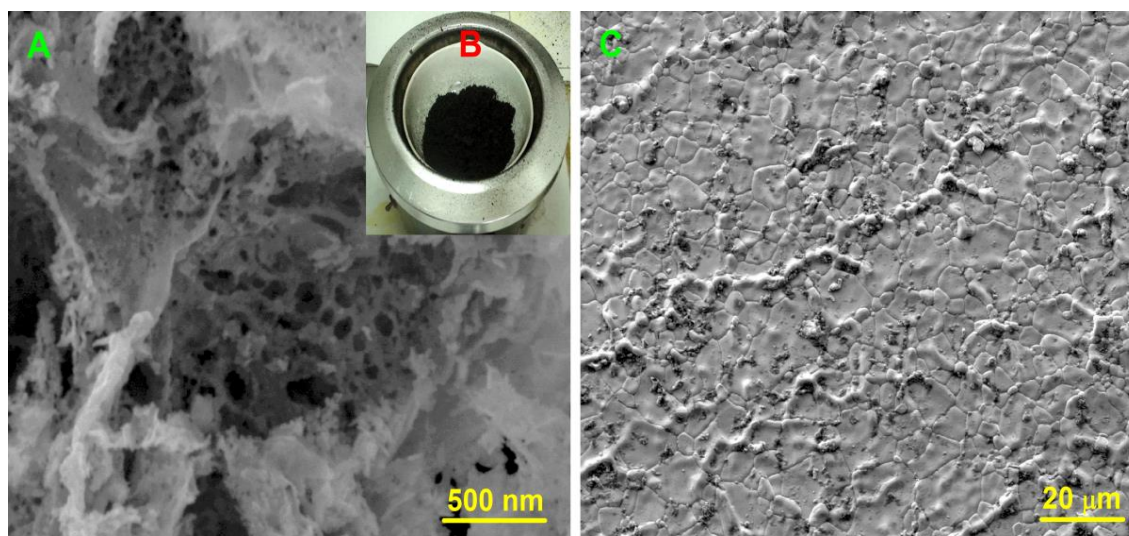
Fig. 37. SEM image of $CoFe_2O_4$ powder prepared by solution combustion synthesis (A – sample 1). $CoFe_2O_4$ powder resulted at the end of the combustion reaction (B – sample 1). SEM image of $CoFe_2O_4$ pellet after sintering at 1100 °C for 2 hours (C – sample 2).

After the sintering process (1100 °C / 2 hours) $CoFe_2O_4$ pellets (sample 2) reached a relative density of 99 % of the theoretical density, which is an excellent result, considering that usually, the sintering temperature of $CoFe_2O_4$ exceeds 1400 °C [30,127-129,134,135]. No pores could be seen on the SEM image of the sintered sample (Fig. 37C). The fine compact microstructure of the sintered pellet confirms the advanced sintering process which occurred during annealing (Fig. 37C). The sintered pellet (sample 2) had practically the same elemental composition (14.2 at. % Co, 28.5 at. % Fe, 57.3 at. % O) as the combustion-synthesized powder, but much larger crystallites – 60 nm (Fig. 34).

The saturation magnetization of the sintered sample (71.3 Am^2/kg) was larger than the one of the combustion-synthesized powder (Fig. 35) which may be related to the increase of the crystallite size (Fig. 34) [132]. At the same time, the coercivity of the sintered pellet decreased to 21.8 kA/m, due to the increase of the crystallite size and the formation of a larger number of magnetic domains [127].

Key findings
- ✓ Highly sinterable $CoFe_2O_4$ particles were prepared by a modified combustion technique, starting from a stoichiometric combination of cobalt acetate, iron nitrate and 5-aminotetrazole.
- ✓ The resulted cobalt ferrite had large surface area (44 m^2/g), small crystallite size (11 nm) and a saturation magnetization of 38.9 Am^2/kg.
- ✓ After sintering at 1100 °C for 2 hours $CoFe_2O_4$ pellets reached 99 % of the theoretical density. The average crystallite size of the sintered $CoFe_2O_4$ was 60 nm.
- ✓ The sintered pellet had a saturation magnetization of 71.3 Am^2/kg and a coercivity of 21.8 kA/m.

2.1.2. Atmosphere control during combustion reactions

The ability of various metal cations to adopt different oxidation states (Fe^{2+}/Fe^{3+}, Eu^{2+}/Eu^{3+}) makes the combustion synthesis of Fe_3O_4, Fe_3O_4/C or $BaAl_2O_4$: Eu^{2+}, Dy^{3+} a challenging task, because in addition to the temperature control, a special attention must be paid to the reaction atmosphere. For instance, to ensure the simultaneous presence of Fe^{2+} and Fe^{3+} (in the case of Fe_3O_4), or to promote the full reduction of Eu^{3+} to Eu^{2+} (in the case of $BaAl_2O_4$: Eu^{2+}, Dy^{3+}) the atmosphere self-generated during the combustion reaction must be a reducing one.

2.1.2.1. Solution combustion synthesis and characterization of Fe_3O_4

From this point of view, the candidate reported [27] a new combustion synthesis technique for the preparation of Fe_3O_4 nanopowders. Combustion synthesis of Fe_3O_4 and properties of the resulted powders have been discussed in relation to reaction atmosphere (in air / in the absence of air) and used fuel (sucrose, citric acid and glucose). Conducting the combustion reactions in air caused the rapid oxidation of Fe^{2+} to Fe^{3+} under the influence of the atmospheric oxygen; therefore the final reaction product was a mixture of α-Fe_2O_3 and γ-Fe_2O_3. In order to avoid the oxidation of Fe^{2+} to Fe^{3+} a simple but efficient solution has been suggested [27]: combustion reactions were carried out in a round bottom flask and the evolving gases were bubbled in a beaker filled with water. This solution allowed the preparation of Fe_3O_4 nanopowders, with crystallite size varying from 10 nm (glucose) to 18 nm (citric acid). Depending on the used fuel, the specific surface area of the magnetite powders varied between 56 m^2/g (citric acid) and 106 m^2/g (glucose). The saturation magnetization of Fe_3O_4 powders prepared in the absence of air ranged between 55.3 emu/g (glucose) and 59.4 emu/g (sucrose). This work was partially supported by the strategic grant POSDRU 107/1.5/S/77265, inside POSDRU Romania 2007-2013 co-financed by the European Social Fund – Investing in People.

General context: magnetite, Fe_3O_4, has attracted considerable interest because of its remarkable properties, which recommend it for a wide field of applications, such as: ferrofluids, magnetic hyperthermia, magnetic resonance imaging, magnetic drug delivery, catalyst, magnetic storage media, removal of different contaminants from water, etc [136-140]. At the same time, the production of pure Fe_3O_4 powders with appropriate features (large surface area, small particle size, narrow size distribution, good magnetic properties etc) has always been a challenge [141]. Therefore several synthesis methods have been suggested: precipitation [142-145], sol-gel [146], hydrothermal [147], thermal decomposition of different precursors [148-151], spray pyrolysis [152], carbothermal reduction [153], etc.

In the recent years, solution combustion synthesis has become a promising candidate for the preparation of a large variety of metal oxide nanopowders [1,4,17,18]. Despite its outstanding advantages – short preparation time, low energy consumption, environmentally friendly – little attention has been paid to the preparation of Fe_3O_4 powders via solution combustion synthesis.

According to Hu et al. [153], the auto-combustion reaction of citrate – iron nitrate precursor yields, in air, a red-brown α-Fe_2O_3 powder. Mukasyan et al. [154] reported the preparation of Fe_3O_4 powder with a specific surface area of 50 m^2/g, by conducting the combustion reaction between iron nitrate and citric acid in argon atmosphere. On the other hand, Toniolo et al. [155] reported that the combustion reaction product of iron nitrate – urea precursor is a mixture of α-Fe_2O_3 and Fe_3O_4. Deshpande et al. [156] prepared ferrimagnetic Fe_3O_4 powders

with exceptionally high coercivity ($\approx$ 17 kA/m), by conducting the combustion reaction between iron nitrate and hydrazine or glycine in argon atmosphere.

Experimental: iron nitrate nonahydrate ($Fe(NO_3)_3 \cdot 9H_2O$, Roth), sucrose (D-(+)-$C_{12}H_{22}O_{11}$, Fluka), citric acid monohydrate ($C_6H_8O_7 \cdot H_2O$, Silal Trading) and glucose (D-(+)-$C_6H_{12}O_6$, Riedel-de-Haën) were the starting raw materials. Stoichiometric metal nitrate/fuel molar ratios were used in all samples, according to reactions (12-14).

$$72\ Fe(NO_3)_3 + 23\ C_{12}H_{22}O_{11} = 24\ Fe_3O_4 + 276\ CO_2 + 253\ H_2O + 108\ N_2 \qquad (12)$$

$$54\ Fe(NO_3)_3 + 46\ C_6H_8O_7 = 18\ Fe_3O_4 + 276\ CO_2 + 184\ H_2O + 81\ N_2 \qquad (13)$$

$$36\ Fe(NO_3)_3 + 23\ C_6H_{12}O_6 = 12\ Fe_3O_4 + 138\ CO_2 + 138\ H_2O + 54\ N_2 \qquad (14)$$
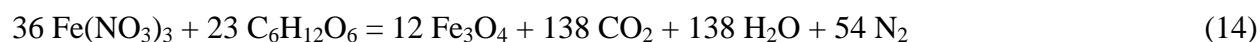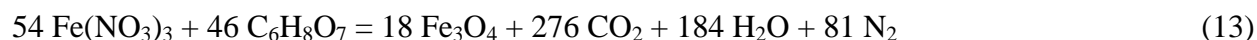
Recipes were designed in order to obtain 0.03 mol of Fe_3O_4. The starting raw materials were mixed under the right proportion and then dissolved in 50 mL of distilled water. The resulting clear solutions were rapidly heated to 400 ºC in a heating mantle in order to trigger the ignition of the combustion reaction. In order to investigate the influence of the air atmosphere, each combustion reaction was conducted under two different sets of conditions:
- under open air, in a porcelain evaporating dish (samples 1–3–5) and
- in the absence of air, in a round bottom flask (samples 2–4–6). In this case, the gases resulted from the combustion process were bubbled in a large beaker filled with distilled water (Fig. 38).
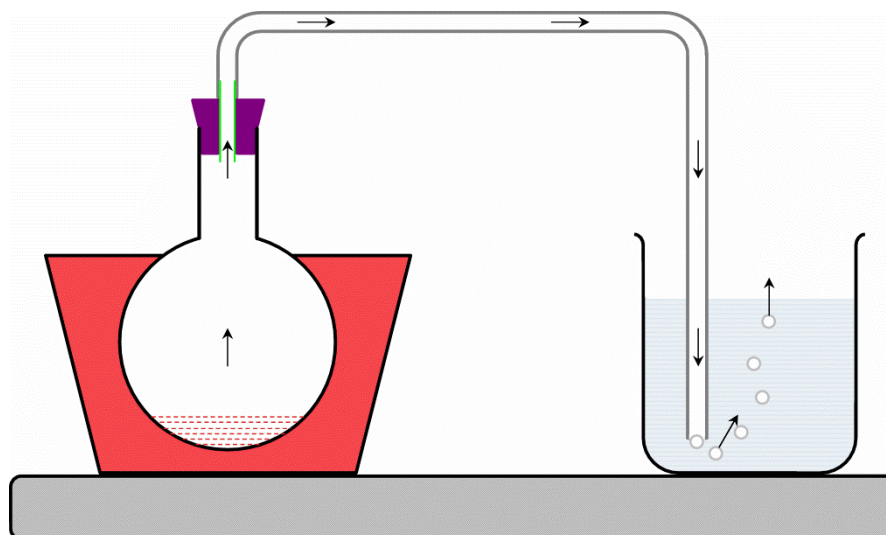
Fig. 38. The installation developed for combustion synthesis of Fe_3O_4 in the absence of air.

As the temperature increased, most of the water evaporated from the precursor solution and a smoldering combustion reaction occurred in all samples. During this process, which lasted for several minutes, large amounts of gases evolved and a loose material was obtained. Finally, the reaction product was hand grinded, washed with fresh distilled water and dried.

The resulted powders were characterized in terms of phase composition, specific surface area and magnetic properties. Thermal behavior of the precursor solutions was studied over the temperature range of 25–700 °C using a Netzsch STA 449 C instrument equipped with Pt

crucibles. The TG and DTA curves were recorded at a heating rate of 10 °C/min under both, air and nitrogen atmosphere, at a constant flow rate of 20 mL/min.

The phase composition of the powders was determined by XRD, using a Panalytical XPERT-PRO diffractometer (monochromated $Cu_{K\alpha}$ radiation) operating at 45 kV and 30 mA. The following PDF files were used for peak assignment: 33-0664 (hematite, α-Fe_2O_3), 19-0629 (magnetite, Fe_3O_4) and 39-1346 (maghemite, γ-Fe_2O_3). The average crystallite size was calculated based on the XRD patters using the Sherrer's equation (1). The peaks used for the Fe_3O_4 crystallite size calculation were the one corresponding to 311 and 440 hkl planes.

The presence of Fe^{2+} and Fe^{3+} was investigated by XPS. The XPS spectra were recorded using a XPS spectrometer SPECS equipped with a dual-anode X-ray source Al/Mg, a PHOIBOS 150 2D CCD hemispherical energy analyzer and a multi-channeltron detector with vacuum maintained at 10^{-9} torr. The $Al_{K\alpha}$ X-ray source (1486.6 eV) operated at 200 W was used for XPS investigations. The high resolution XPS spectra of Fe 2p core level were recorded by accumulating 10 scans at 30 eV pass energy and 0.1 eV/step. The sample powder was pressed on an indium foil to allow the XPS measurements. A cleaning of the samples surface was performed by argon ion bombardment (500 V) and the spectra were recorded before and after the cleaning. Data analysis and curve fitting was performed using CasaXPS software with a Gaussian-Lorentzian product function and a non-linear Shirley background substraction.

Specific surface area of the powders, S_{BET}, was measured by BET (Brunauer, Emmett, Teller) nitrogen gas adsorption technique using a Micromeritics ASAP 2020 instrument. Assuming that the magnetite particles have a spherical shape, the equivalent diameter was calculated using equation (2), considering a theoretical density of Fe_3O_4 of 5.2 g/cm^3. Magnetic properties were measured at room temperature by vibrating sample magnetometry, using a VSM 880 ADE/DMS magnetometer.

Results and discussion: the evolution of combustion reactions was strongly influenced by the working atmosphere. Basically, the combustion reactions performed in the presence of air were visibly more exothermic than the same reactions conducted in the absence of air, in a round bottom flask. The decisive role of the working atmosphere was confirmed by the thermal analysis of the precursor solutions containing iron nitrate and sucrose (Fig. 39a), citric acid (Fig. 39b) or glucose (Fig. 39c) recorded under air and in the absence of air (in nitrogen atmosphere), respectively.
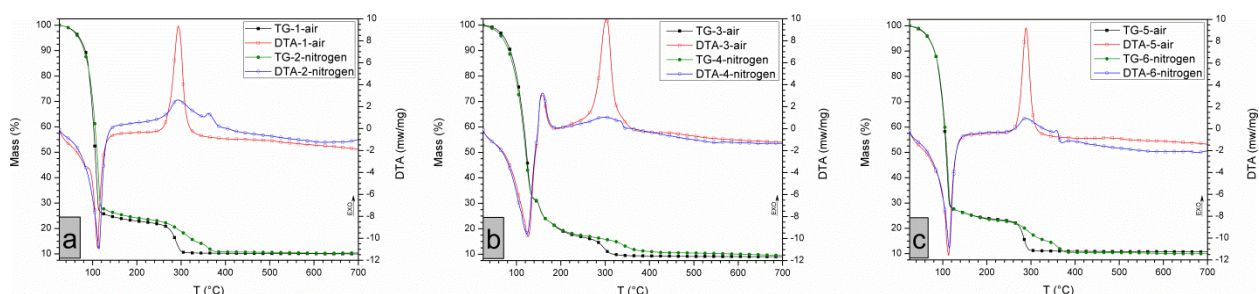

Fig. 39. TG-DTA curves of the precursor mixtures recorded under air and nitrogen atmosphere.

The general profile of TG curves indicates that all samples undergo a major mass loss (about 70 %) up to 120 °C, regardless of the working atmosphere or selected fuel (Fig. 39a–c). The DTA curves suggest that this mass loss is the result of a strong endothermic process. Based

on the literature data, one can assume that the strong endothermic effect is actually a superposition of the endothermic effects associated with water removal and iron nitrate partial decomposition (hydrolysis) [157]. Up 140 °C all samples have a very similar behavior, regardless of the working atmosphere. However, the situation changes radically as the temperature increases. For instance, the TG curves recorded in air indicate that over the temperature range of 250–320 °C samples 1–3–5 undergo a final mass loss, which is done in a single step. On the same temperature interval, the DTA curves recorded in air atmosphere exhibit a strong exothermic effect, which can be assigned to combustion reaction development.

The DTA curves of samples of 2–4–6 (Fig. 39a-c), indicate that changing the working atmosphere from air to nitrogen causes a major decrease of combustion reaction intensity, as well as an extension of the temperature range in which combustion reactions occur (250–360 °C). The TG curves of samples 2–4–6 emphasize once more that combustion reactions carried out in nitrogen are less exothermic than the same combustion reactions carried out in air. One may notice that during combustion reaction development, the mass of samples 2–4–6 decreases at a much lower rate than the mass of samples 1–3–5. In addition, the samples studied in nitrogen atmosphere reached a constant mass at a higher temperature than the samples studied in air.

The photographic images of the powders prepared by conducting the combustion reactions in air (samples 1–3–5) and in the absence of air (samples 2–4–6) are shown in Fig. 40. Color differences that exist between the two sets of samples are the result of performing the combustion reactions in different environments, with different exothermicity, as already confirmed by thermal analysis. At the same time, the reddish color of the samples obtained in air suggests a phase composition which is different from the phase composition of the black samples prepared in the absence of air.

The XRD patterns shown in Fig. 41 point out that hematite, α-Fe_2O_3, is the main crystalline phase in samples 3 and 5, obtained in air, which explains the reddish color of these powders (Fig. 40).
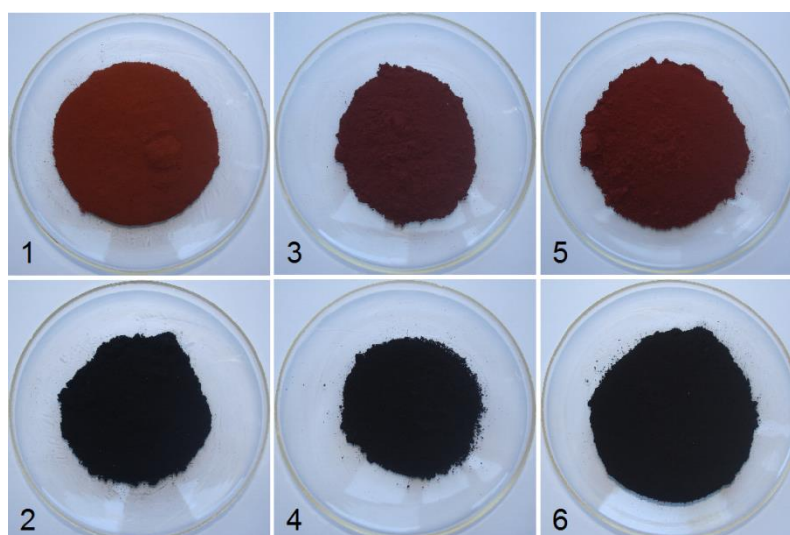
Fig. 40. Images of the powders resulted from the combustion process conducted under open air (samples 1–3–5) and in a round bottom flask (samples 2–4–6), respectively.

However, small positive values of saturation magnetization (Table 10) of these samples suggest the presence of minor amounts of ferrimagnetic phase, below the detection limit of XRD method. Given the reddish color of the samples, as well as the presence of atmospheric oxygen

during the powder preparation one can assume that γ-Fe_2O_3 is the ferrimagnetic phase responsible for these low values of saturation magnetization.

Table 10. Characteristics of the powders prepared by solution combustion synthesis.

No.	Fuel / Reaction conditions	XRD phase composition	D_{XRD} (nm)	S_{BET} (m^2/g)	D_{BET} (nm)	Ms (emu/g)	Mr (emu/g)	Hc (kA/m)
1.	Sucrose / air	γ-Fe_2O_3, α-Fe_2O_3	-	65	-	29.0	2.3	4.7
2.	Sucrose / flask	Fe_3O_4	15	71	16	59.4	3.8	2.9
3.	Citric acid / air	α-Fe_2O_3, γ-Fe_2O_3	-	11	-	4.1	0.3	4.9
4.	Citric acid / flask	Fe_3O_4	18	56	21	57.7	4.5	5.2
5.	Glucose / air	α-Fe_2O_3, γ-Fe_2O_3	-	15	-	1.5	0.3	16.9
6.	Glucose / flask	Fe_3O_4	10	106	11	55.3	3.3	3.0

Based on the XRD pattern of sample 1, the final reaction product in air is a mixture of γ-Fe_2O_3 and α-Fe_2O_3 (Fig. 41). This is in excellent agreement with the higher saturation magnetization of sample 1, with respect to samples 3 and 5 (Table 10). All together – the reddish color of samples 1–3–5, the small values of saturation magnetization and the absence of Fe_3O_4 peaks from the XRD patterns of the samples prepared in air – indicate that the preparation in air of Fe_3O_4 powders via solution combustion synthesis is a delicate problem. The main obstacle hindering the solution combustion synthesis of Fe_3O_4 in air seems to be the oxidation of Fe^{2+} to Fe^{3+} (15), which takes place during combustion reaction:

$$4\ Fe_3O_4 + O_2 = 6\ Fe_2O_3 \tag{15}$$
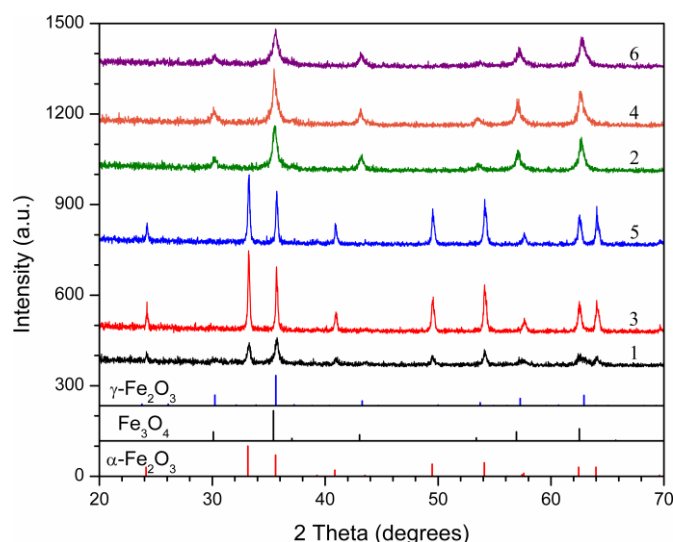
Fig. 41. XRD patterns of the powders prepared by combustion synthesis in air (samples 1–3–5) and in a round bottom flask (samples 2–4–6).

In the particular case of the combustion method, the oxidation of Fe^{2+} to Fe^{3+} is very munch enhanced due to the high reactivity of large surface area Fe_3O_4 nanopowders (Table 10) resulted from the combustion process. Such behavior should draw one's attention back to the combustion synthesis principles, which state that combustion redox reactions should be balanced assuming that atmospheric oxygen does not participate to the redox processes. The results reported hereby show that in the case of Fe_3O_4 preparation, the atmospheric oxygen does

participate to the combustion reaction, as reported by other authors [155,158]. The superposition of different processes (iron nitrate – fuel combustion reaction, oxidation of Fe^{2+} to Fe^{3+}, atmospheric oxygen – fuel interactions) explains the higher exothermicity of combustion reactions performed in air, as seen from the TG-DTA analysis (Fig. 39a–c).

Looking at the specific surface area of the powders (Table 10), one may notice that when the same fuel is used, the powder prepared in the absence of air exhibits larger surface area than the powder prepared in air. This observation corroborated with the profile of the DTA curve (Fig. 39) indicates that the temperature reached during the combustion reactions conducted under air atmosphere was higher than the temperature reached during the same combustion reactions performed in the absence of air. In addition, the higher temperature reached during the development of combustion reactions conducted in air promotes the formation of hematite, α-Fe_2O_3 (Fig. 41), which is the high temperature polymorph modification of Fe_2O_3.

The XRD patterns of samples 2–4–6 (Fig. 41) confirmed the formation of Fe_3O_4 as a single crystalline phase. The average crystallite size depends on the used fuel: 15 nm (sucrose), 18 nm (citric acid), 10 nm (glucose). Since the positions of the peaks in the XRD patterns are almost identical for γ-Fe_2O_3 and Fe_3O_4, XPS was used to show the presence of both Fe^{2+} and Fe^{3+}. The high-resolution XPS spectra of Fe 2p core level from samples 2, 4 and 6 are shown in figure 42. The Fe 2p spectrum contains the Fe 2p3/2 and Fe 2p1/2 doublet.
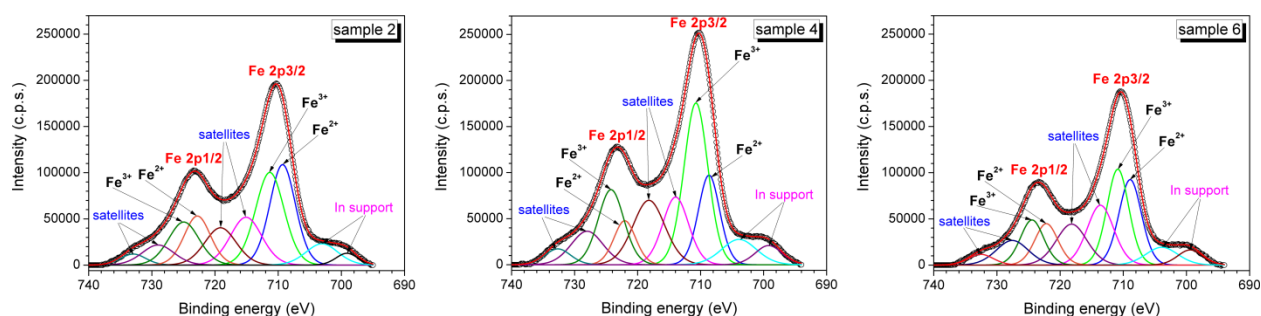
Fig. 42. High-resolution XPS spectra of Fe 2p core level from samples 2–4–6.

The contribution from the indium support can be observed at low energies 700–703 eV. The peaks positions of the main lines Fe 2p3/2, Fe 2p1/2 and their corresponding satellites indicate that samples 2–4–6 contain both Fe^{3+} and Fe^{2+} ions [159,160]. The Fe^{3+}/ Fe^{2+} atomic ratios calculated for samples 2–4–6 (0.9, 1.4 and 0.8 respectively) are smaller than the theoretical ratio, which is found in pure magnetite (Fe^{3+} / Fe^{2+} = 2).

Based on the Fe^{3+}/ Fe^{2+} atomic ratios and considering the XRD analysis (Fig. 41), one can conclude that alongside Fe_3O_4 there is also some amorphous FeO. The presence of excessive FeO is due to the reducing atmosphere created during the combustion reaction, which is a strong indication that the method suggested hereby is suitable for controlling the reaction atmosphere. One may expect that the optimization of iron nitrate / fuel ratio will lead to the formation of pure magnetite.

Powders 2–4–6 prepared by carrying out the combustion reactions in the absence of air have a black color, typical for magnetite (Fig. 40). The specific surface areas of the Fe_3O_4 powders obtained in the absence of air (samples 2–4–6) in a round bottom flask are considerably larger (71–56–106 m^2/g) than those reported by other authors who also addressed the preparation of magnetite powders via combustion synthesis [154]. The average crystallite size calculated

from the XRD patterns is slightly smaller than the grain size calculated from the BET surface area (Table 10).

In terms of reaction atmosphere, one can conclude that the preparation of Fe_3O_4 nanopowders via combustion synthesis requires to conduct the combustion reactions in the absence of air, or, to be more specific in the absence of oxygen. In order to overcome this drawback, we suggest an innovative solution which consists in carrying out the combustion reactions in a round bottom flask (Fig. 38). The gases resulting from the combustion process are bubbled in a beaker filled with water. This simple mechanism prevents air from getting in the round flask and ensures a reaction atmosphere with no oxygen, suitable for Fe_3O_4 formation. This ingenious solution is considerably simpler and cheaper than using an expensive furnace or reactor equipped with an inert atmosphere of nitrogen or argon [154,156].

Figure 43 shows the room-temperature magnetic hysteresis loops of the combustion synthesized powders. The saturation magnetization was calculated by plotting M versus 1/H and extrapolating the data to 1/H → 0 (extrapolation to infinite field). Table 10 indicates that the saturation magnetization of samples 2–4–6 (59.4–57.7–55.3 emu/g) is much higher than the saturation magnetization of samples 1–3–5 (29.0–4.1–1.5 emu/g). This is in agreement with the different phase composition of the two sets of samples, as evidenced by XRD and XPS analysis.
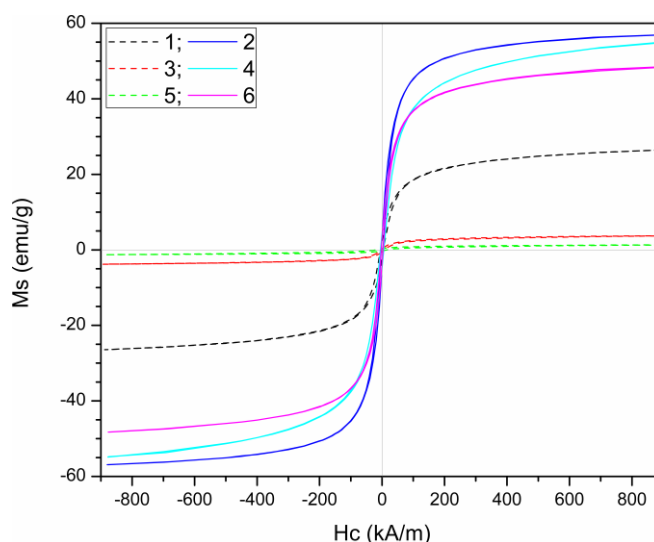
Fig. 43. Room-temperature magnetic hysteresis loops of the powders prepared by solution combustion synthesis under open air (1–3–5) and in a round bottom flask (samples 2–4–6).

At the same time, combustion synthesized Fe_3O_4 nanopowders (samples 2–4–6) exhibit lower saturation magnetization when compared to bulk Fe_3O_4, which may be explained by the small grain size as well as by the existence of some non-magnetic carbon impurities, resulted from the incomplete fuel oxidation [151]. Obviously, in this case the real saturation magnetization of Fe_3O_4 particles is even higher than the measured one.

Unlike the results reported by other authors [154-156] who used the combustion method for the preparation of Fe_3O_4, the magnetite powders 2–4–6 prepared by conducting the combustion reactions in a round bottom flask exhibit higher saturation magnetization, lower remnant magnetization (3.8–4.5–3.3 emu/g) and lower coercivity (2.9–5.2–3.0 kA/m), which indicates that the Fe_3O_4 particles are very close to the superparamagnetic behavior.

Key findings

✓ Solution combustion synthesis of Fe_3O_4 and properties of the resulted powders have been investigated in relation to the reaction atmosphere (in air and in the absence of air) and used fuel (sucrose, citric acid and glucose).

✓ The phase composition of combustion reaction product proved to be less influenced by the used fuel, whilst the reaction atmosphere had a major influence on the powder composition. On the other hand, specific surface area, particle size and magnetic properties of the powders were equally determined by the reaction atmosphere and the used fuel.

✓ In the case of the tested fuels (sucrose, citric acid, glucose) conducting the combustion reactions in air causes the rapid oxidation of Fe^{2+} to Fe^{3+} under the influence of the atmospheric oxygen; therefore the final reaction product is a mixture of α-Fe_2O_3 and γ-Fe_2O_3. In order to avoid the oxidation of Fe^{2+} to Fe^{3+} under the influence of the atmospheric oxygen an ingenious, simple but efficient solution has been suggested: combustion reactions were carried out in a round bottom flask, the evolving gases being bubbled in a beaker filled with water.

✓ The solution we suggest hereby allowed the preparation of nanocrystalline Fe_3O_4 powders. The magnetite crystallite size was 10 nm in the case of glucose and 18 nm in the case of citric acid. Depending on the used fuel, the specific surface area of the magnetite powders varied between 56 m^2/g (citric acid) and 106 m^2/g (glucose). The saturation magnetization of the samples prepared in the absence of air ranges between 55.3 emu/g (glucose) and 59.4 emu/g (sucrose), whilst the coercivity varies between 2.9 kA/m (sucrose) and 5.2 kA/m (citric acid).

Related findings

✤ The in vitro effects of combustion synthesized magnetite nanoparticles – coated with a double layer of oleic acid and dispersed in a phosphate buffered saline solution – on SK-BR-3 breast cancer cell line and human adult mesenchymal stem cells were also studied [161]. After 48 hours of contact, SK-BR-3 tumor cells exhibited a very rare and unusual behavior, extruding their nucleus. Under similar conditions, the human adult mesenchymal stem cells did not suffer the enucleation process [161], which might indicate a certain degree of toxic selectivity of these nanoparticles with respect to SK-BR-3 tumor cells only. The enucleation phenomenon described in the case of SK-BR-3 tumor cells treated with combustion synthesized nanoparticles might reveal a novel mechanism for cancer cell death, occurring under certain environmental conditions [161].

✤ Several magnetic iron oxides prepared under similar conditions (combustion synthesis carried out in air and in the absence of air) were tested as adsorbent materials for phenol, p-chlorophenol [162-164] and Congo Red dye [165], showing good results. The effective adsorbent properties were associated with the large BET surface area of the powders, but also, in some cases, to the presence of organic residues on the surface of particles, as a direct result of the synthesis method.

2.1.2.2. Magnetite/carbon nanocomposites prepared by combustion synthesis

The benefits of conducting the combustion reactions in the absence of air were confirmed during the preparation of magnetite/carbon nanocomposites within a work partially supported by the strategic grant POSDRU 107/1.5/S/77265 (2010) of the Ministry of Labor, Family and Social Protection, Romania, co-financed by the European Social Fund – Investing in people. Magnetite nanoparticles embedded within a matrix of activated carbon were prepared for the first time using a simple and effective combustion synthesis technique [28]. The resulted nanocomposites had a magnetite/carbon mass ratio varying between 1/1 and 1/10 and exhibited a ferrimagnetic behavior. As the magnetite/carbon ratio decreased from 1/1 to 1/10, the BET surface area increased from 360 m^2/g to 814 m^2/g and the saturation magnetization decreased from 34.1 emu/g to 7.8 emu/g. The as-prepared composites were tested as adsorbents for the removal of phenol and p-chlorophenol. The removal efficiency of phenol and p-chlorophenol increased as the magnetite/carbon ratio decreased. Using an adsorbent mass of 2 g/L, magnetite/carbon nanocomposites showed a removal efficiency ranging from 89 % to 98 % for p-chlorophenol. For the same adsorbent mass, the removal efficiency of phenol varied between 59 % and 91 %. The experimental data for phenol and p-chlorophenol adsorption on magnetite/carbon nanocomposites were best fitted by the Sips isotherm and showed a significant increase of the maximum adsorption capacity with the increase of the carbon content. The unique combination of enhanced adsorption capacity, excellent separation capability and the short time span for reaching equilibrium indicate that the as-prepared magnetite/carbon nanocomposites are excellent adsorbent materials.

General context: water pollution caused by industrialization, agricultural activities and the population growth, received considerable attention worldwide. The effluents containing heavy metal ions, dyes, pesticides, phenolic compounds and other toxic pollutants severely threaten the aquatic ecosystem and the human health [166,167]. Therefore, the removal of pollutants from wastewater is of significant importance and represents a constant challenge.

As a result of researches in the field of pollution control and management, various techniques were developed for the removal of pollutants from wastewater, including oxidation [168], coagulation/flocculation [169], photo-degradation [170], reverse osmosis [171], ion exchange [172], extraction [173], adsorption [174,175]. Among these methods, adsorption proved to be a superior technique in terms of cost, wide range of applications, simplicity of design, availability of a wide range of adsorbents, low harmful secondary products, facile regeneration of the adsorbents and high effectiveness [175-177]. Depending on the used adsorbent, the removal capacity by this method may be up to 99.9 % [167]. Activated carbon, polymers, waste materials, by-products in industries and agriculture, zeolites, silica-gel and hydrogels were investigated as adsorbents for the removal of hazardous compounds [177-182].

Activated carbon is one of the most popular and widely used adsorbent for wastewater treatment, since it is a versatile adsorbent with very good adsorption capacity for a large variety of pollutants. However, its main disadvantages are the high cost production, regeneration issues, poor mechanical properties and difficulties in liquid-solid phase separation [177,183]. The magnetic separation technique offers new perspectives in the development of adsorptive technologies, generating more efficient and cost-effective remediation approaches as compared with conventional technologies [184-186].

To make full use of the magnetic separation technology it is imperative to develop magnetic adsorbents with simple preparation process, inexpensive and with high adsorption capacity. Magnetic iron oxide nanoparticles are considered valuable candidates for the development of next-generation of adsorbents with great potential for the efficient treatment of large volume of wastewater and fast separation using an external magnetic field [185].

Additionally, magnetic iron oxide nanopowders show chemical stability, low toxicity, and excellent reuse capacity, are cost-effective and possess a huge potential to enhance the adsorption capacity by their surface modification with suitable functional groups, specific to the contaminant type [185,187]. Considering the excellent adsorption capability of activated carbon, researchers are attempting to develop magnetic nanosorbents by combining the strong adsorption capacity of carbon materials with the ferrimagnetic-superparamagnetic nature of various iron oxides or ferrites.

Carbon/magnetic nanocomposites are considered the most suitable magnetic adsorbents for wastewater treatment [188-190]. Although many techniques including chemical vapor deposition [191], standard and modified carbon arc techniques [192,193], pyrolysis of organometallic compounds [194], solvothermal [183,195,196] have been reported for the synthesis of carbon/magnetite nanocomposites, they are usually multistep or require severe conditions and toxic or expensive raw materials.

Although, there have been reported several papers [4,197-199] dealing with impregnation-based solution combustion synthesis and different carriers were used, little attention has been paid to the synthesis of magnetite/carbon nanocomposites.

Experimental: 0.090 mols of $Fe(NO_3)_3 \cdot 9H_2O$ (Roth) and 0.138 mols of $C_4H_6O_6$ (Merck) were dissolved in 50 mL of distilled water. The resulting solution was poured into a round bottom flask containing different amounts of activated carbon (Utchim), according to Table 11.

Table 11. Composition of the investigated magnetite/carbon nanocomposites.

Sample	$Fe(NO_3)_3 \cdot 9H_2O$ (g)	$C_4H_6O_6$ (g)	Activated carbon (g)	Fe_3O_4/carbon mass ratio
1.	36.3600	20.7124	-	1/0
2.	36.3600	20.7124	6.9459	1/1
3.	36.3600	20.7124	13.8918	1/2
4.	36.3600	20.7124	20.8377	1/3
5.	36.3600	20.7124	34.7295	1/5
6.	36.3600	20.7124	69.4590	1/10
7.	-	-	6.9459	0/1

After the activated carbon was impregnated for 24 hours with the iron nitrate and tartaric acid solution, the flask was placed inside a heating mantle at 400 °C. As the temperature increased, a smoldering combustion reaction occurred between iron nitrate and tartaric acid. The gases evolving from the combustion process were bubbled in a beaker filled with distilled water, to prevent air getting inside the flask. After 30 minutes, the gas evolution stopped and a black fluffy powder was obtained. The resulting powder was washed with warm distilled water and dried at 70 °C for 5 hours. The phase composition of the samples was studied by X-ray diffraction (XRD) using a Rigaku Ultima IV instrument. The XRD patterns were recorded using $Cu_{K\alpha}$ radiation. Crystallite size was calculated using the PDXL 2.0 software.

The heating behavior of the samples was studied over the range of 25–1000 °C by thermal analysis, using a Netzsch 449 C instrument. TG–DTA curves were recorded using Pt crucibles, under an artificial air flow of 200 mL/min, at a heating rate of 10 °C/min.

After the samples were degassed for 12 hours at 100 °C and 5 µmHg, the nitrogen adsorption-desorption isotherms were recorded using a Micromeritics ASAP 2020 instrument at 77 K. The specific surface area was calculated using the Brunauer–Emmett–Teller (BET) method. Micropore area, external surface area and micropore volume were calculated using the t-plots. Cumulative volume of pores was computed using the Barrett–Joyner–Halenda (BJH) method from the adsorption isotherms.

The magnetic properties of the samples were measured at room temperature by vibrating sample magnetometry using a VSM 880 ADE/DMS instrument. FT-IR spectra were carried out using a Shimadzu Prestige-21 spectrometer in the range of 400–1500 cm^{-1} at a resolution of 4 cm^{-1}. The morphology of the magnetite/carbon nanocomposites was investigating by scanning electron microscopy (SEM), using a FEI Quanta FEG 250 microscope.

The adsorption of phenol and p-chlorophenol (PCP) from aqueous solution onto magnetite/carbon nanocomposites was performed at 25 °C, at a pH of 6.5 using 1 g/L and respectively 2 g/L adsorbent mass and different initial concentrations of 50-200 mg/L. All experiments were performed at a shaking speed of 200 rpm. At predetermined time intervals, the adsorbent was separated from the aqueous solution using a NdBFe magnet. The concentration of phenol and PCP was monitored using a Shimadzu UV–VIS spectrophotometer. The absorbance values were measured at the wavelength of 270 nm for phenol and at 280 nm for PCP. The adsorption process was assessed by calculating the adsorbed amount, q_t (mg/g) (Eq. (16)) and the removal efficiency R (%) of the adsorption process (Eq. (17)):

$$q_t = \frac{(C_0 - C_t) \cdot V}{m} \tag{16}$$

$$R = \frac{C_0 - C_e}{C_0} \cdot 100 \tag{17}$$

C_0 is the initial concentration of solution (mg/L), C_t and C_e are the concentrations at different times and at equilibrium (mg/L), V is the volume of solution (L), m is the adsorbent mass (g).

Results and discussion: XRD patterns of the samples prepared by solution combustion synthesis are shown in Fig. 44. One can see that the activated carbon (sample 7) has an amorphous structure, whilst all the other compositions contain a single crystalline phase, namely magnetite, Fe_3O_4. The average crystallite size of magnetite, calculated from peak broadening, ranges between 12 and 21 nm. These results suggest that the as prepared composites are made up of nanocrystalline Fe_3O_4 particles embedded within an amorphous matrix of activated carbon.

N_2 adsorption-desorption isotherms of magnetite/carbon nanocomposites measured at 77 K are shown in Fig. 45. One may notice that sample 1 (magnetite) exhibits a type IV isotherm, whilst sample 7 (activated carbon) has a type II isotherm. In the case of magnetite/carbon nanocomposites (samples 2-6), the profile of the isotherms gradually changes from type IV isotherm to type II isotherm, as the magnetite/carbon ratio decreases.
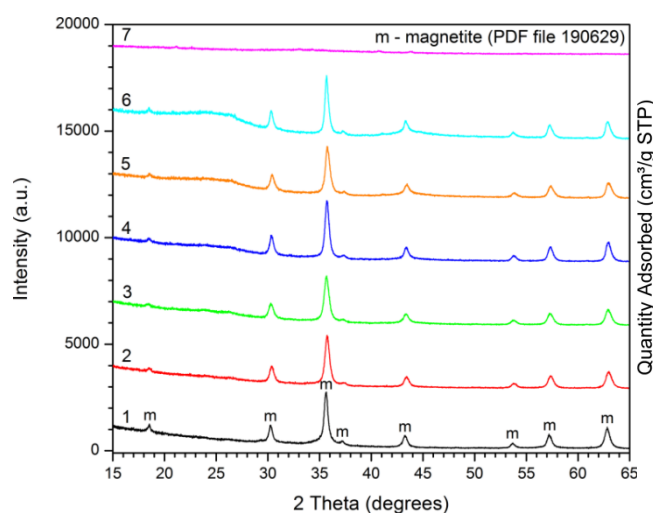
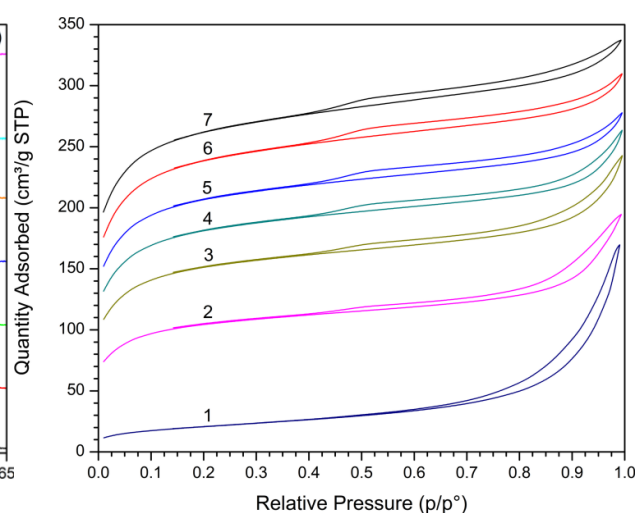Fig. 44. XRD patterns of the samples prepared by combustion synthesis.

Fig. 45. Adsorption-desorption isotherms of magnetite/carbon nanocomposites.

Sample 1, which contains only Fe_3O_4, has the lowest surface area – 75 m^2/g. In this case, only ≈ 5 % of the BET surface area is the contribution of micropore area whilst ≈ 95 % is the contribution of the external surface area (Table 12). On the other hand, sample 7, which contains only activated carbon, has the largest BET surface area (890 m^2/g) among all samples. In this case, ≈ 64 % of the BET surface area is represented by the micropore area and ≈ 36 % is the contribution of the external surface area. The large value of micropore area is also reflected by the large micropore volume. As a matter of fact, sample 7 (activated carbon) has a micropore volume 264 times larger than sample 1 (magnetite) (Table 12).

Table 12. Characteristics of magnetite/carbon nanocomposites.

Sample	Fe_3O_4/carbon mass ratio	BET surface area (m^2/g)	Micropore area (m^2/g)	External surface area (m^2/g)	Micropore volume (cm^3/g)	Pore diameter (nm)
1.	1/0	75	4.0	71.2	0.001	14.0
2.	1/1	360	211.5	148.4	0.096	7.4
3.	1/2	522	317.8	204.5	0.144	6.2
4.	1/3	622	390.9	231.5	0.178	5.4
5.	1/5	706	460.8	245.5	0.212	4.8
6.	1/10	814	505.6	307.9	0.234	4.4
7.	0/1	890	568.8	321.1	0.264	4.4

Since the surface area is a key feature of adsorption materials, it is crucial to be able to tune the surface area of the as-prepared materials. From this point of view, combustion synthesis seems to be an adequate method for the preparation of magnetite/carbon nanocomposites with BET surface area ranging from 360 to 814 m^2/g. By changing the magnetite/carbon ratio, one can adjust the BET surface area of the resulted composites. As the magnetite/carbon ratio decreases the BET surface area and the micropore volume increase constantly (Table 12). All magnetite/carbon nanocomposites (samples 2-6) exhibit a micropore area larger than the external surface area, which is related to the presence of activated carbon. The evolution of specific magnetization as a function of the applied field (Fig. 46) suggests that all samples containing

Fe$_3$O$_4$ (samples 1-6) have a ferrimagnetic behavior. As expected, pure magnetite (sample 1) has the largest saturation magnetization, whilst activated carbon has the lowest (sample 7) saturation magnetization (Fig. 46). The saturation magnetization of magnetite/carbon nanocomposites (sample 2-6) decreases as the magnetite/carbon ratio decreases. Magnetic separation experiments evidenced that even sample 6, which has the smallest content of magnetite, and therefore the lowest saturation magnetization, could be easily extracted from water using a NdBFe magnet.
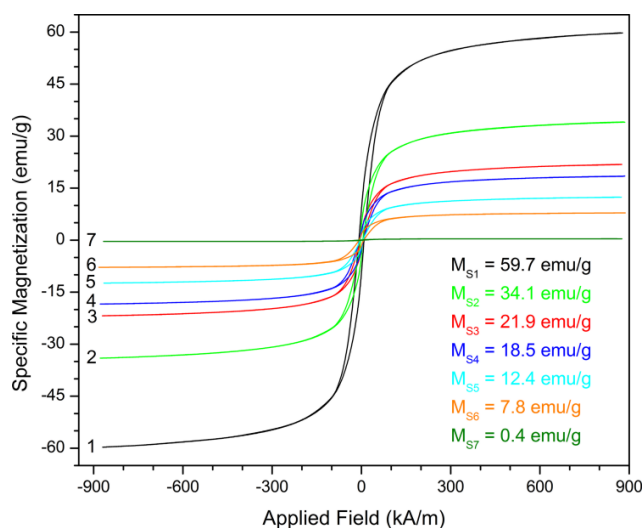
Fig. 46. Magnetic hysteresis curves of magnetite/carbon nanocomposites.

Thermal analysis revealed that up to 350 °C, sample 4 – having a magnetite/carbon ration of 1/3 – does not suffer any significant transformation (Fig. 47). Between 350 °C and 750 °C sample 4 undergoes a substantial mass loss (67.2 %) which is accompanied by a broad and intense exothermic effect on the DTA curve. Most likely, this process can be assigned to the carbon oxidation. At the same time, the oxidation of Fe$_3$O$_4$ to γ-Fe$_2$O$_3$ and probably its conversion to α-Fe$_2$O$_3$ take place over the same temperature range, but these processes are hindered by the carbon oxidation. As the carbon content increased from sample 2 to sample 6, the TG analysis of magnetite/carbon composites revealed an increasing mass loss from 43.6 % to 83.1%, due to carbon oxidation.
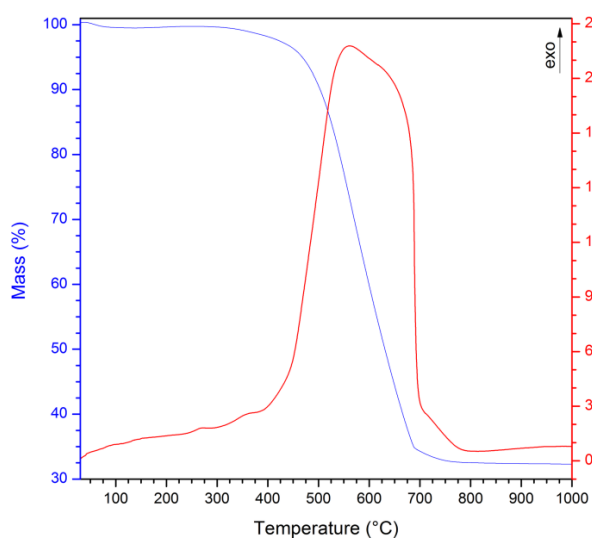
Fig. 47. TG-DTA curves of sample 4.
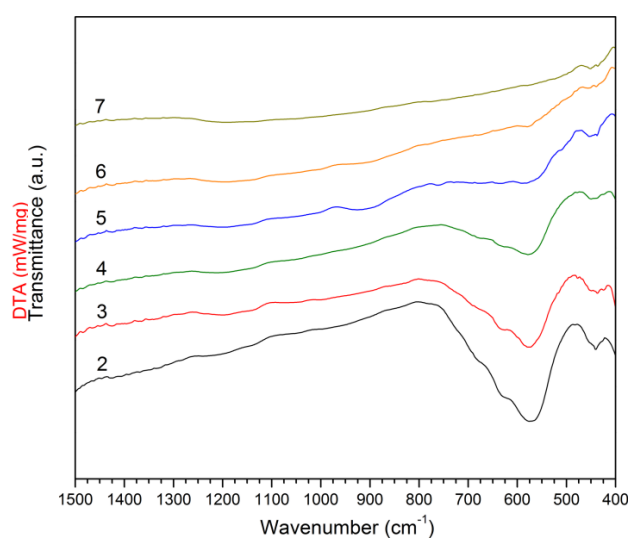
Fig. 48. FT-IR spectra of samples 2-7.

The FT-IR spectra of samples 2-7 are shown in Fig. 48. The band located at 574.8 cm^{-1} is assigned to the Fe-O vibration in Fe_3O_4 [200-202]. The intensity of this band is related to the magnetite content from the nanocomposites. As the magnetite/carbon ratio decreases, from sample 2 to sample 6, the intensity of the band located at 574.8 cm^{-1} also decreases.

SEM measurements revealed that magnetite nanoparticles have a spherical shape and an average diameter of ≈ 40 nm (Fig. 49). The particle size observed by SEM is larger than the average crystallite size calculated from the XRD patterns suggesting that the magnetite nanoparticles are polycrystalline – in agreement with the ferrimagnetic behavior of these nanocomposites (Fig. 46). Unlike the magnetite nanoparticles, the carbon particles are much larger (several microns) and have an irregular plate-like morphology. It appears that the magnetite nanoparticles are accumulated on the carbon surface (Fig. 49).
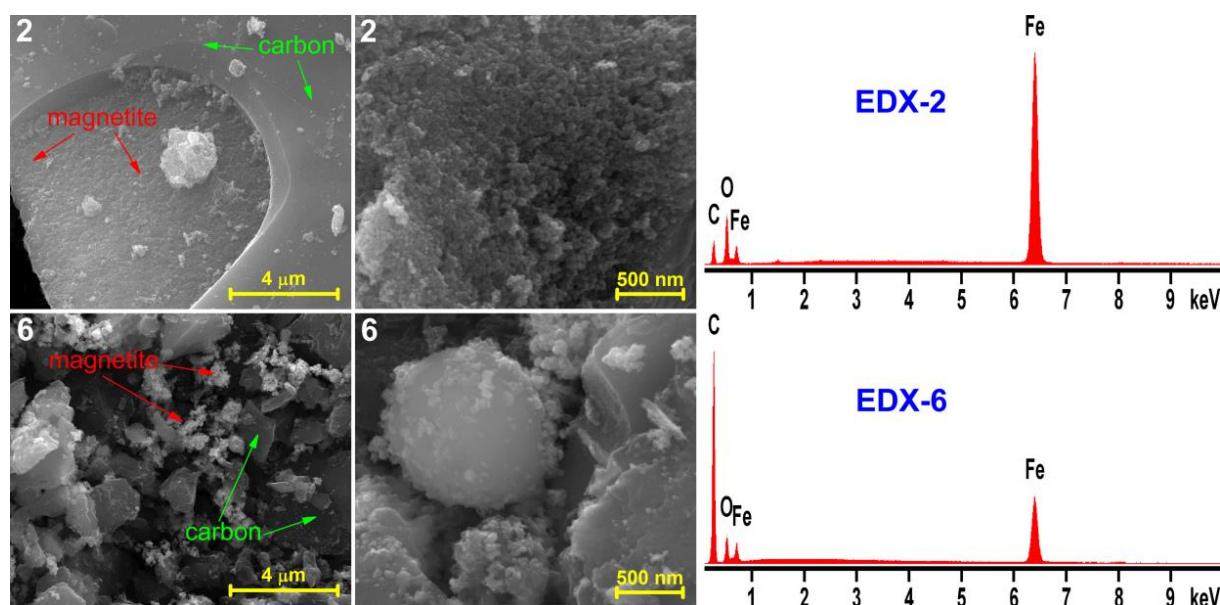
Fig. 49. SEM-EDX analysis of samples 2 and 6.

As seen on the SEM and EDX spectra, the proportion of magnetite nanoparticles is considerably smaller in the case of sample 6, which is consistent with the lower magnetite/carbon mass ratio (1/10 – in the case of sample 6, and 1/1 – in the case of sample 2).

The effect of magnetite/carbon ratio on the removal efficiency is shown in Figs. 50 and 51 for phenol and PCP respectively. As can be observed, the increase of the carbon content from sample 2 to sample 7, continually increases the removal efficiency for both, phenol and PCP. It is also evident that the removal efficiency increases with the increase of the adsorbent mass from 1 g/L to 2 g/L, especially in the case of phenol adsorption.

Using an adsorbent mass of 2 g/L, the removal efficiency of PCP (Fig. 51) increases from 89 % (sample 2) up to 98 % (sample 6), which is practically identical with the removal efficiency of activated carbon (sample 7). These results prove that even the adsorbent 2, with the lowest carbon content, shows a very good efficiency for the PCP removal. For the same mass of adsorbent, the removal efficiency of phenol (Fig. 50) was lower than the removal efficiency of PCP (Fig. 51).

Using an adsorbent mass of 2 g/L, sample 4 had a phenol removal efficiency of 85 %. As the BET surface area of magnetite/carbon nanocomposites increased, the phenol removal efficiency also increased, up to 91 % for adsorbent 6. As a matter of fact, the phenol removal

efficiency of sample 6 is very close to the one achieved by using activated carbon alone (sample 7 - 92 %). Based on these results it can be concluded that all the prepared magnetite/carbon nanocomposites can be successfully used for the PCP removal. Samples 4-6 show very good results for phenol removal.
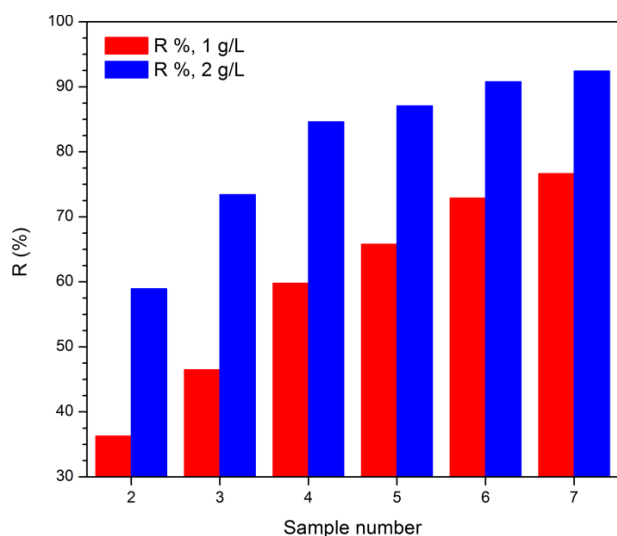
Fig. 50. Removal efficiency of phenol onto samples 2-7 (C_0 - 100 mg/L).
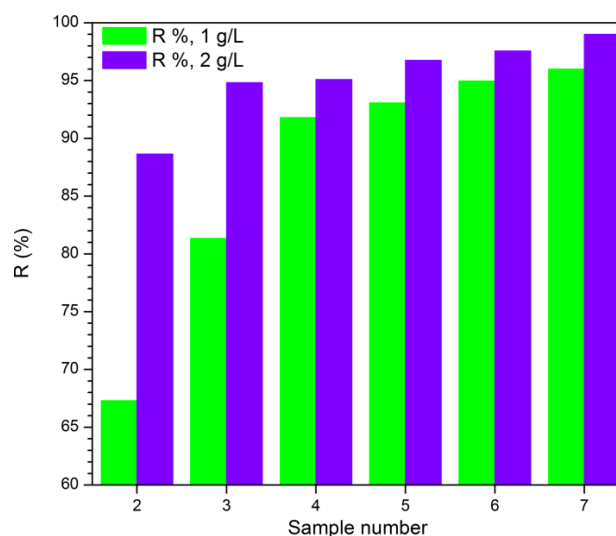
Fig. 51. Removal efficiency of PCP onto samples 2-7 (C_0 - 100 mg/L).

Besides the excellent adsorption capacity imparted by the activated carbon, the presence of ferrimagnetic magnetite embedded within the carbon matrix considerably enhances the separation process of magnetite/carbon nanocomposites from aqueous solutions. Figure 52 shows the effect of contact time on the removal of phenol and PCP by magnetite/carbon nanocomposites 2-6. The adsorption of phenol and PCP onto samples 2-6 is very fast during the first 20 minutes, and then it becomes slower, as the system approaches equilibrium.
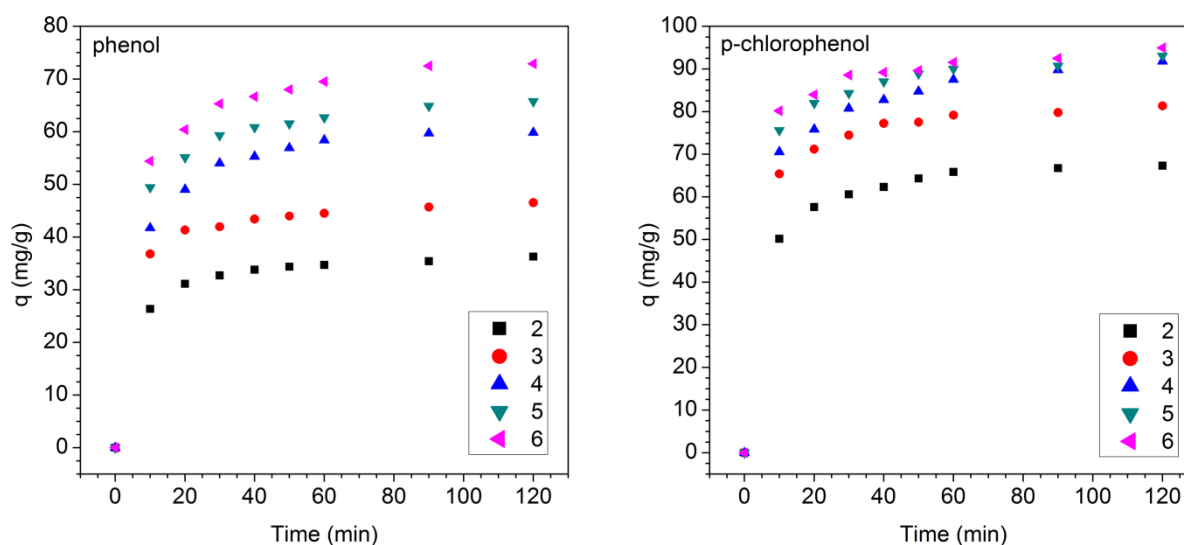
Fig. 52. Amount adsorbed versus time for phenol and PCP removal onto samples 2-6 (C_0 - 100 mg/L, m - 1 g/L).

This can be explained by the high availability of vacant sites on the adsorbent surface at the initial stage, and which are gradually being occupied in time as a result of the sorption

process. With the increase of the carbon content, from sample 2 to sample 6, a longer time for reaching equilibrium is needed. This can be correlated with the decrease of the average pore diameter as the magnetite/carbon mass ratio decreases (Table 12). It is also important to note that the amount of phenol and PCP adsorbed on magnetite/carbon nanocomposites increases with the increase of the carbon content, from the sample 2 to the sample 6.

The experimental equilibrium data were fitted with Langmuir, Freundlich, Redlich–Peterson and Sips isotherms [203-205] to find the most suitable model that can be used for designing and assessing the performance of the adsorption process. The optimum isotherm out of the four above mentioned was determined by non-linear regression analysis, using ORIGIN 8 software. Figure 53 shows the experimental equilibrium data fitted to the four isotherms for the phenol and PCP adsorption onto sample 6.
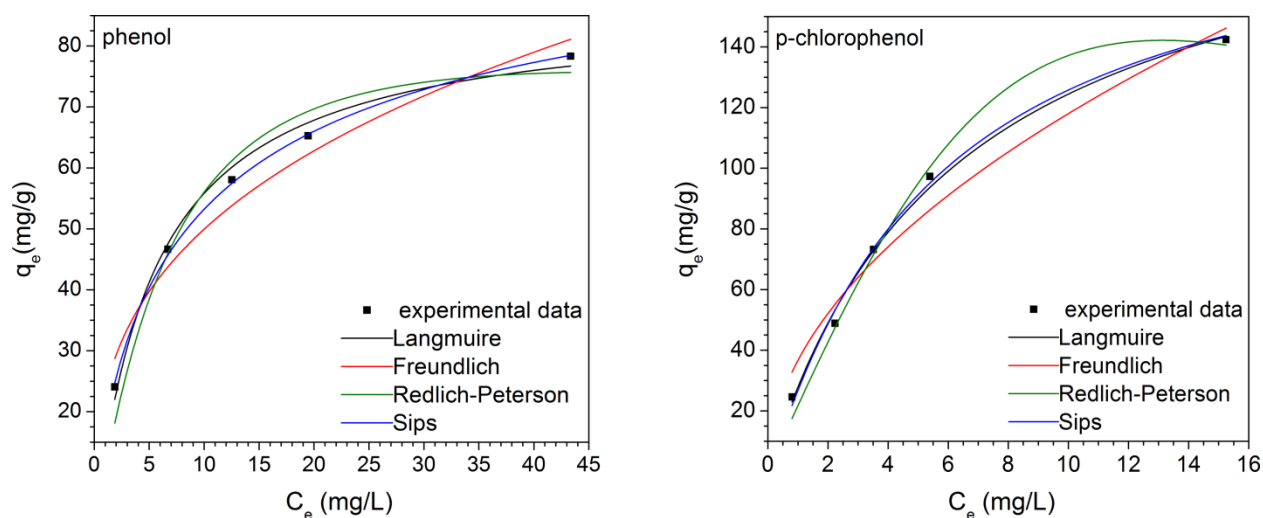
Fig. 53. Isotherm plots for phenol and PCP adsorption onto sample 6 (m - 2 g/L): q_e is the amount of solute adsorbed per unit mass of adsorbent at equilibrium; C_e is the equilibrium concentration of the solute in the bulk solution.

The isotherm parameters and the correlation coefficient (R^2) for the adsorption of phenol and PCP respectively onto samples 2-6 are listed in Table 13. Comparing the correlation coefficients of the analyzed isotherms, the best model that fits the equilibrium data for the phenol and PCP adsorption onto all samples, is the Sips model.

One can notice that the maximum adsorption capacity gradually increases from sample 2 to sample 6, for both, phenol and PCP. The Sips maximum adsorption capacity for phenol increases from 24.78 mg/g (sample 2) to 66.47 mg/g (sample 6). In the case of PCP the Sips maximum adsorption capacity increases from 69.76 mg/g (sample 2) to 218.00 mg/g (sample 6) (Table 13). This behavior can be correlated with the gradually increase of the BET surface area from 360 m^2/g (sample 2) to 814 m^2/g (sample 6) (Table 13).

It can be also noted that all samples show a much better adsorption capacity for PCP as compared to phenol, in agreement with the results reported in the literature [204-207]. This behavior can be explained by the lower solubility of PCP as compared to phenol. According to the literature data, the adsorption of phenol and chlorophenols on activated carbon is controlled by dispersion forces between the π-electrons of the aromatic ring in phenols and the π-electrons in activated carbon [204,206,207].

The presence of chloro-group (strong electron-withdrawing group) in PCP reduces the overall electron density of the aromatic ring enhancing attraction with the surface of carbon, which leads to an increase in adsorption capacity.

Table 13. Isotherm parameters and the correlation coefficients for the adsorption of phenol and PCP onto 2 g/L of magnetite/carbon nanocomposites.

	Isotherm parameters and correlation coefficient		Samples				
			2	3	4	5	6
phenol	Langmuir	K_L (L mg^{-1})	0.0580	0.0692	0.1519	0.1069	0.1824
		q_m (mg g^{-1})	44.896	57.373	70.105	81.904	86.412
		R^2	0.9858	0.9940	0.9736	0.9876	0.9927
	Freundlich	K_F (mg$^{1-(1/n)}$L$^{1/n}$g^{-1})	9.6038	12.0647	19.535	17.5917	23.3218
		n	0.058	3.127	3.378	2.822	3.024
		R^2	0.9835	0.9697	0.9832	0.9742	0.9419
	Redlich–Peterson	K_{RP} (L g^{-1})	2.1805	3.3566	6.0873	5.8369	11.006
		α_{RP} ((L mg^{-1})$^\beta$)	0.0350	0.0414	0.0329	0.0274	0.0664
		β	1.065	1.068	1.217	1.220	1.162
		R^2	0.9706	0.9850	0.8994	0.9577	0.9647
	Sips	K_S (L mg^{-1})	0.1022	0.1066	0.1771	0.132	0.1958
		q_{mS} (mg g^{-1})	24.776	34.717	47.674	56.562	66.474
		n	1.756	1.508	1.771	1.439	1.391
		R^2	0.9986	0.9958	0.9995	0.9965	0.9991
PCP	Langmuir	K_L (L mg^{-1})	0.1809	0.1415	0.3840	0.1756	0.1600
		q_m (mg g^{-1})	84.766	121.48	135.75	158.60	202.19
		R^2	0.9939	0.9959	0.9906	0.9812	0.9956
	Freundlich	K_F (mg$^{1-(1/n)}$L$^{1/n}$g^{-1})	29.8529	31.478	47.5456	37.2152	36.6619
		n	4.546	3.340	3.514	2.628	1.970
		R^2	0.8722	0.9187	0.9232	0.9125	0.9686
	Redlich–Peterson	K_{RP} (L g^{-1})	7.8457	11.273	41.242	17.083	21.866
		α_{RP} ((L mg^{-1})$^\beta$)	0.0331	0.0399	0.2341	0.0085	0.0062
		β	1.216	1.186	1.065	1.697	1.982
		R^2	0.9219	0.9654	0.9762	0.9770	0.9917
	Sips	K_S (L mg^{-1})	0.2197	0.1538	0.3812	0.1682	0.1622
		q_{mS} (mg g^{-1})	69.760	106.49	124.47	180.44	218.00
		n	1.180	1.091	1.177	0.916	0.934
		R^2	0.9952	0.9964	0.9943	0.9841	0.9961

Langmuir: q_m is the maximum monolayer adsorption capacity, K_L is the Langmuir sorption constant. Freundlich: K_F is the Freundlich constant, n is a dimensionless constant related to the intensity of adsorption. Redlich–Peterson: K_{RP} is the Redlich-Peterson constant, α_{RP} is a constant, β is an exponent varying between 0 and 1. Sips: K_S is the Sips constant, q_{mS} is the Sips maximum adsorption capacity and n is the Sips model exponent.

Key findings

✓ Magnetite nanoparticles embedded within an amorphous matrix of activated carbon were successfully prepared using a simple and effective combustion synthesis technique. Properties of magnetite/carbon nanocomposites can be properly adjusted by using different $Fe(NO_3)_3$/activated carbon ratios. The resulted nanocomposites had a magnetite/carbon ratio varying between 1/1 and 1/10 and exhibited a ferrimagnetic behavior.

✓ As the magnetite/carbon ratio decreased from 1/1 to 1/10, the saturation magnetization decreased from 34.1 to 7.8 emu/g. At the same time, the BET surface area of magnetite/carbon nanocomposites increased from 360 up to 814 m^2/g.

✓ The removal efficiency of phenol and p-chlorophenol increased as the magnetite/carbon ratio decreased. For an adsorbent mass of 2 g/L, magnetite/carbon nanocomposites showed a removal efficiency ranging from 89 to 98 % for p-chlorophenol.

✓ For the same adsorbent mass, the removal efficiency of phenol varied between 59 and 91 %. The experimental data for phenol and p-chlorophenol adsorption onto all magnetite/carbon nanocomposites were best fitted by the Sips isotherm and showed a significant increase of the maximum adsorption capacity with the increase of the carbon content.

✓ The unique combination of enhanced adsorption capacity (due to the activated carbon), excellent separation capability (given by the presence of magnetite) and the short time span for reaching equilibrium (≈ 40 minutes) indicate that magnetite/carbon nanocomposites prepared by one step combustion synthesis are excellent adsorbent materials, with great potential for industrial scale wastewater treatment.

2.1.2.3. <u>Solution combustion synthesis of bluish-green BaAl$_2$O$_4$: Eu^{2+}, Dy^{3+} phosphors</u>

The preparation of Fe$_3$O$_4$ or Fe$_3$O$_4$/carbon composites requires not only a *reducing atmosphere* but also a relatively *low combustion temperature* to avoid the oxidation reactions and polymorph transformations. In the case of long-afterglow phosphor materials, such as BaAl$_2$O$_4$: Eu^{2+}, Dy^{3+} the *reducing atmosphere* (generated in situ by the use of fuel reach recipes) facilitates the reduction of Eu^{3+} to Eu^{2+}, which is essential for the optical properties [24]. However, in this case an *elevated combustion temperature* is also mandatory to ensure the formation of the desired crystalline phase. From this point of view, the candidate prepared by an upgraded combustion technique BaAl$_2$O$_4$: Eu^{2+}, Dy^{3+} bluish-green phosphors, starting from Ba(ClO$_4$)$_2$ instead of Ba(NO$_3$)$_2$ (slightly soluble), NH$_4$NO$_3$ (to increase the combustion temperature) and a mixture of urea (in excess, to create the reducing atmosphere) and glycine [24]. The average crystallite size of BaAl$_2$O$_4$: Eu^{2+}, Dy^{3+} samples varied between 72 and 82 nm and the BET specific surface area was 1.4 m^2/g. The emission spectra of BaAl$_2$O$_4$: Eu^{2+}, Dy^{3+} phosphors showed a single band at 499 nm. Increasing the Eu^{2+} proportion from 0.005 to 0.020 led to a slight increase of the emission band intensity. The presence of Dy^{3+} improves the afterglow without modifying the wavelength of the emitted radiation. For the same Eu^{2+} proportion, increasing the Dy^{3+}/Eu^{2+} ratio from 0/1 to 3/1 contributes to a sharp increase of the emission band intensity. This work was supported by the Sectoral Operational Programme Human Resources Development, financed from the European Social Fund and by the Romanian Government under the contract number POSDRU/86/1.2/S/58146 (MASTERMAT).

General context: recently materials showing luminescent properties, such as MAl$_2$O$_4$ (M = Ca, Sr, Ba) doped with Eu^{2+} and Dy^{3+} became intensely studied due to their long-lasting phosphorescence and high intensity emission radiation [208-210]. Such materials are suitable for numerous applications as fluorescent lamps and screens, LEDs, sensors and detectors for radiations, warning and emergency signs [211-213]. With a view to obtain materials with enhanced phosphorescence, most researchers focus on SrO-Al$_2$O$_3$ system, whilst BaO-Al$_2$O$_3$ system is less explored, although the emission time may as well last over a few hours in the case of Eu^{2+} and Dy^{3+} - doped BaAl$_2$O$_4$.

The dependence of the luminescent properties on the synthesis conditions prompted scientists to use various obtaining methods for BaAl$_2$O$_4$: Eu^{2+}, Dy^{3+}. By comparison with the classical method [214,215] or hydrothermal method [216], solution combustion synthesis [217-220] shows a series of clear advantages. Thus, the formation of the desired crystalline structure takes place more rapidly and solely on the account of the heat generated from the combustion reaction. This highly exothermic reaction is ignited by the rapid heating of an adequate mixture of oxidizing agents and fuels. Moreover, the high temperature generated ensures the crystallite growth, which enhances the emission intensity and the afterglow of the phosphor material.

Despite these advantages, obtaining pure BaAl$_2$O$_4$: Eu^{2+}, Dy^{3+} via combustion synthesis may encounter serious difficulties because of the reduced Ba(NO$_3$)$_2$ solubility and improper fuel choice. This explains the presence of Ba(NO$_3$)$_2$ [221] or BaAl$_{12}$O$_{19}$ [220,222] impurities alongside BaAl$_2$O$_4$: Eu^{2+}, Dy^{3+} solid solution when using urea as single fuel, which often reflects in poor optical properties.

Experimental: the raw materials used for BaAl$_2$O$_4$: Eu^{2+}, Dy^{3+} phosphors were: Ba(ClO$_4$)$_2$ (Merck), Al(NO$_3$)$_3$·9H$_2$O (Merck), Eu$_2$O$_3$ (Sigma-Aldrich), Dy$_2$O$_3$ (Merck), HNO$_3$

(Chimopar), $C_2H_5NO_2$ (Merck), CH_4N_2O (Merck) and NH_4NO_3 (Chimopar). The recipes were elaborated in order to obtain 0.03 moles of $BaAl_2O_4$: Eu^{2+}, Dy^{3+}, considering the following molar ratio of the raw materials: $(1-x-y)$ $Ba(ClO_4)_2$: x $Eu(NO_3)_3$: y $Dy(NO_3)_3$: 2 $Al(NO_3)_3$: $(16-y)/9$ $C_2H_5NO_2$: 5 CH_4N_2O. The actual stoichiometry of $BaAl_2O_4$: Eu^{2+}, Dy^{3+} phosphors prepared by combustion synthesis is shown in Table 14.

Table 14. Stoichiometry of $BaAl_2O_4$: Eu^{2+}, Dy^{3+} phosphors, prepared by combustion synthesis.

Sample no.	X	Y	$Ba_{1-x-y}Eu_xDy_yAl_2O_4$
0.	0.000	0.000	$BaAl_2O_4$
1.	0.010	0.000	$Ba_{0.99}Eu_{0.01}Al_2O_4$
2.	0.010	0.010	$Ba_{0.98}Eu_{0.01}Dy_{0.01}Al_2O_4$
3.	0.010	0.020	$Ba_{0.97}Eu_{0.01}Dy_{0.02}Al_2O_4$
4.	0.010	0.030	$Ba_{0.96}Eu_{0.01}Dy_{0.03}Al_2O_4$
4a.	0.010	0.030	$Ba_{0.96}Eu_{0.01}Dy_{0.03}Al_2O_4$
5.	0.005	0.010	$Ba_{0.985}Eu_{0.005}Dy_{0.01}Al_2O_4$
6.	0.015	0.030	$Ba_{0.955}Eu_{0.015}Dy_{0.03}Al_2O_4$
7.	0.020	0.040	$Ba_{0.94}Eu_{0.02}Dy_{0.04}Al_2O_4$

In order to compensate the urea loss due to hydrolysis side reaction and also to ensure a reducing atmosphere necessary for Eu^{3+} to Eu^{2+} conversion, 50 wt. % urea excess was used in relation with the required stoichiometric amount.

On the other hand, for enhanced reaction exothermicity NH_4NO_3 was added to the raw materials mixture in a 100 wt. % ratio related to the amount of $BaAl_2O_4$: Eu^{2+}, Dy^{3+} to be obtained. This was done with a view to promote the development of the $BaAl_2O_4$ crystalline structure and facilitate the inclusion of Eu^{2+} and Dy^{3+} in the $BaAl_2O_4$ network.

In a first stage, the necessary amounts of Eu_2O_3 and Dy_2O_3 were dissolved in hot HNO_3 and a clear, slightly yellowish solution was obtained. This solution was subjected to evaporation at 110 °C. The rest of the raw materials dissolved in 50 mL of hot distilled water (80 °C) were then added to the obtained europium and dysprosium nitrates, according to the general working procedure shown in Fig. 54.
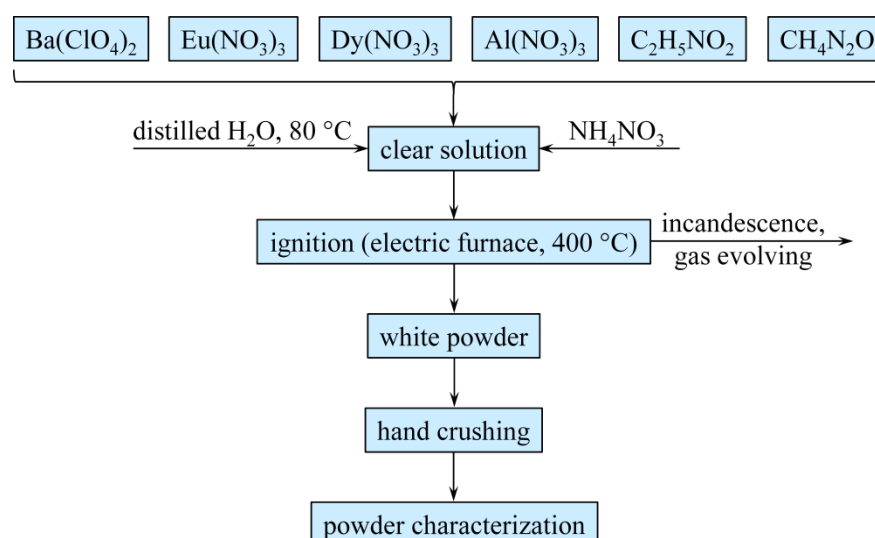

Fig. 54. Working procedure used for $BaAl_2O_4$: Eu^{2+}, Dy^{3+} preparation via combustion synthesis.

The porcelain dish containing the such-obtained solution was introduced in a preheated electric furnace at 400 °C. As the temperature of the raw materials mixture increased, most of the water evaporated and a highly exothermic combustion reaction took place. During this reaction large amounts of colorless gases evolved and the temperature of the sample increased very fast, leading to incandescence. The combustion reaction lasted for about 40 seconds and yielded a voluminous, white fluffy powder. In the case of sample 4, some of the resulted powder was also subjected to further annealing in an electric oven at 1200 °C, for 2 hours (10 ºC/min heating rate in air atmosphere, 4 ºC/min cooling rate). The such-treated sample was marked as 4a.

The phase composition of the obtained powders was established by X-ray diffraction using a Rigaku ULTIMA IV, $Cu_{K\alpha}$ radiation (0.15418 nm) produced at 40 kV and 40 mA. The average crystallite size was calculated from the recorded diffraction patterns of the samples using the instrument integrated PDXL2 software.

BET (Brunauer–Emmett–Teller) specific surface area of the samples was measured by nitrogen adsorption at liquid N_2 temperature using a Micromeritics ASAP 2020 instrument.

The samples were previously degased for 5 hours at 300 °C under 5 µmHg vacuum. The emission spectra of $BaAl_2O_4$: Eu^{2+}, Dy^{3+} powders were recorded by fluorescence spectrometry using a Perkin Elmer LS 55 instrument.

Morphology and particle size of the powders resulted from the combustion reaction were explored by scanning electron microscopy using a FEI Quanta FEG 250 microscope.

Results and discussion: studying the evolution of the combustion reactions lead to the conclusion that the presence of $Eu(NO_3)_3$ and $Dy(NO_3)_3$ does not significantly influence the redox processes. The XRD patterns presented in Fig. 55, indicate $BaAl_2O_4$: Eu^{2+}, Dy^{3+} as single phase in all the obtained samples. The formation of the designed crystalline phase $BaAl_2O_4$: Eu^{2+}, Dy^{3+} is due to the high exothermicity of the combustion reactions, which confirms the viability of using highly soluble $Ba(ClO_4)_2$ as oxidizing agent, instead of the traditional, less soluble $Ba(NO_3)_2$ [223].

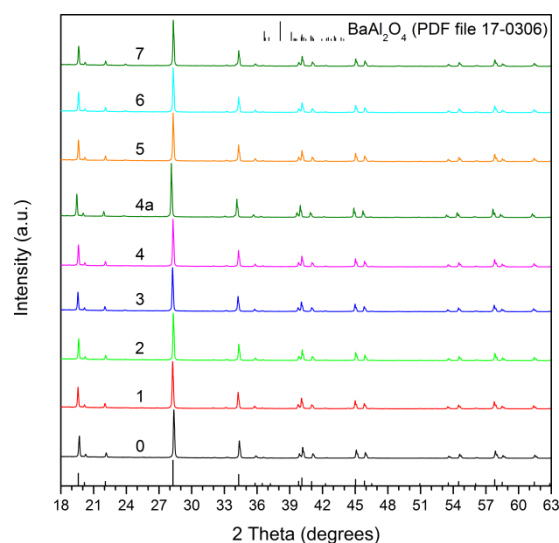Fig. 55. XRD patterns of $BaAl_2O_4$: Eu^{2+}, Dy^{3+} powders prepared by combustion synthesis.

One may notice that even in the case of sample 7, containing the highest amount of Eu^{2+} and Dy^{3+}, the solid solution is present as single phase. The as-resulted $BaAl_2O_4$: Eu^{2+}, Dy^{3+} crystallite size varies between 72 and 82 nm. Considering on the one hand the extremely short

reaction duration (approximately 40 seconds) and on the other hand the relatively large crystallites size, one can appreciate that the temperature developed during combustion was very high, exceeding 1200 °C. In addition, the BET specific surface area of the powders resulting from the combustion is extremely low (1.4 m^2/g).

Comparing the crystallite size of sample 4 and sample 4a (obtained after subsequent annealing of sample 4 at 1200 °C for 2 hours) we found the two values are very close: 82 nm (sample 4) and 84 nm (sample 4a). Although it is said that larger crystallite size lead to improved luminescent properties [216,218], in the case of combustion-synthesized $BaAl_2O_4$: Eu^{2+}, Dy^{3+} the subsequent annealing is useless since it does not promote crystallite growth. The SEM images evidence that the obtained powders consist of flat particle agglomerates, which vary in size (Fig. 56a). The formation of these agglomerates can be attributed to the sintering process, which is favored by the high temperature reached during the combustion reaction (Fig. 56b and c). Using a higher magnification, the SEM image of sample 4 reveals the presence of hexagonal rods-like formations (Fig. 56c). This $BaAl_2O_4$: Eu^{2+}, Dy^{3+} powder morphology is in accordance to the hexagonal crystalline structure of $BaAl_2O_4$ described by Sun [224] or Zhang [216] et al.
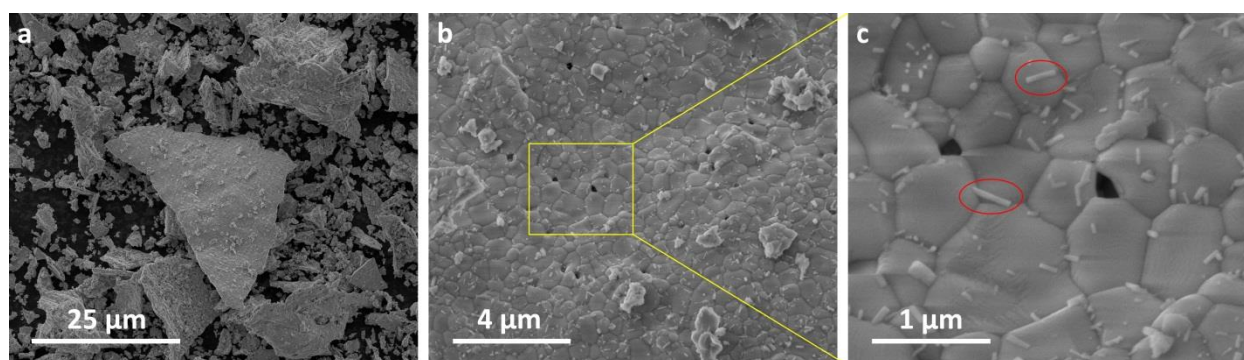
Fig. 56. SEM images of $BaAl_2O_4$: Eu^{2+}, Dy^{3+} (sample 4) obtained by combustion synthesis.

Figure 57 shows images of the obtained $BaAl_2O_4$: Eu^{2+}, Dy^{3+} phosphors under VIS and UV illumination, respectively. In visible light the powders obtained from combustion are white regardless of their stoichiometry. On the other hand, under UV illumination the samples containing europium (1-7) present a bluish-green color which is typical for these phosphors [213,214,217]. One may also clearly notice the weak intensity of the light emitted by sample 4a compared with sample 4.
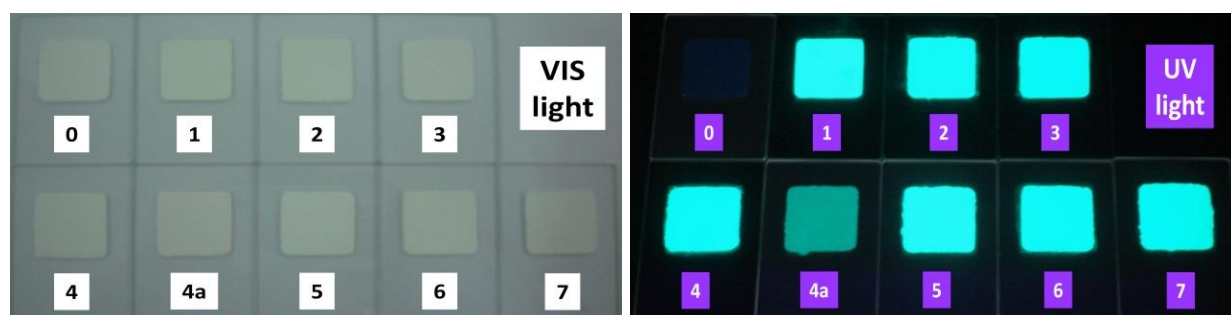
Fig. 57. Images of the $BaAl_2O_4$: Eu^{2+}, Dy^{3+} powders under VIS and UV illumination.

The emission spectra of samples 1-4 (Fig. 58)c show that all the samples excited at 339 nm exhibit a single emission band situated between 400 and 600 nm with a maximum at 499 nm,

regardless the Dy^{3+}/Eu^{2+} ratio. The emission band at 499 nm is specific for the bluish-green $BaAl_2O_4$: Eu^{2+}, Dy^{3+} and is assigned to the $4f^65d^1 \rightarrow 4f^7$ transition of electrons within Eu^{2+} ions [220-222]. Many authors have reported in the case of $BaAl_2O_4$: Eu^{2+}, Dy^{3+} phosphors the presence of a shoulder at 426 nm [224], 450 nm [221], 435 nm [224] or 440 nm [222] alongside the maximum at 500 nm. Yet, it is clear that in the case of the samples obtained within the present paper, no shoulder is present on the emission spectra (Fig. 58). This shape of the emission spectra may be explained taking into account the structure of $BaAl_2O_4$.
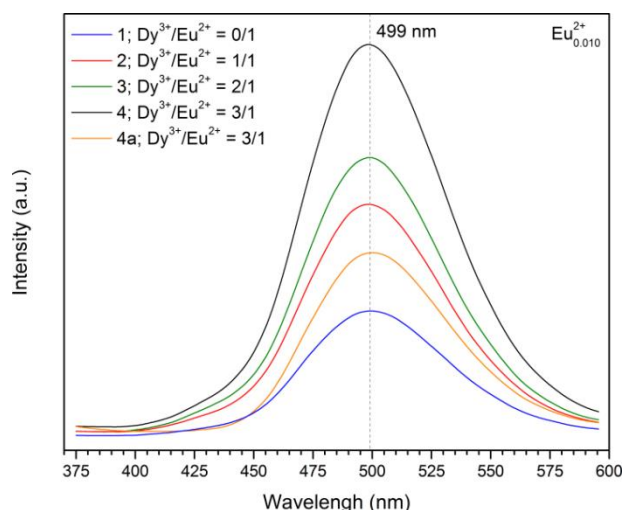

Fig. 58. Emission spectra of the obtained $BaAl_2O_4$: Eu^{2+}, Dy^{3+} phosphors excited at 339 nm: influence of the Dy^{3+}/Eu^{2+} molar ratio.
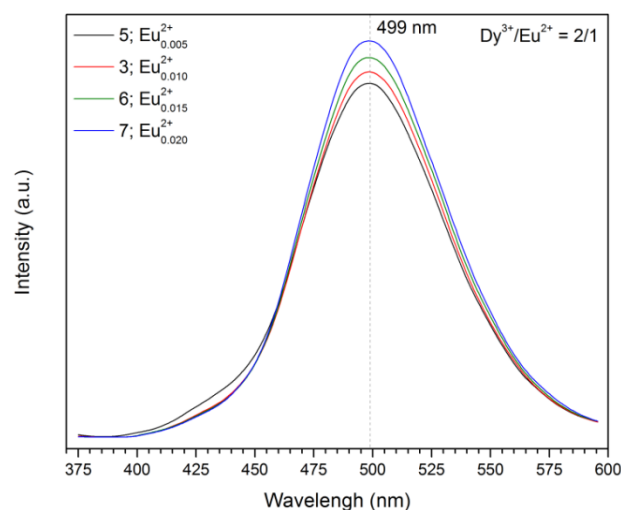
Fig. 59. Emission spectra of the $BaAl_2O_4$: Eu^{2+}, Dy^{3+} phosphors excited at 339 nm: influence of the Eu^{2+} proportion.

Ba^{2+} cations occupy two types of positions in the $BaAl_2O_4$ structure (2a and 6c respectively), which differ by the length of Ba–O bonds and symmetry degree [214,220]. Moreover, the 6c positions are three times more numerous than 2a positions. As a result of $Ba^{2+} \leftrightarrow Eu^{2+}$ substitution, the Eu^{2+} cations may theoretically occupy both types of positions, in which situation the emission spectra would present both the maximum at 500 nm and a shoulder at 420 – 450 nm [222,225].

The absence of this shoulder in the case of the samples obtained within the present paper suggests that the Eu^{2+} cations occupy only one of the two available positions. Taking into account that the length of the Ba–O bond in the case of Ba^{2+} cations occupying the 6c positions is very close (2.69 Å) to that of the Eu^{2+}–O bond length (2.68 Å), most probably the Eu^{2+} cations occupy the 6c positions [214,225].

Analyzing the influence of the Dy^{3+}/Eu^{2+} molar ratio upon the emission band intensity at 499 nm (Fig. 58), one may notice that all the samples containing Dy^{3+} exhibit higher intensity than the sample doped solely with Eu^{2+} (sample 1). On the other hand the presence of Dy^{3+} does not lead to new emission bands, which suggests that Eu^{2+} is the emission center. Increasing the Dy^{3+}/Eu^{2+} molar ratio from 0/1 to 3/1 leads to an enhanced emission at 499 nm, which confirms the viability of using Dy^{3+} as co-activator.

A very interesting issue was found with respect to the influence of the supplementary thermal treatment applied to the sample 4 showing the highest emission (Fig. 58). After annealing in air at 1200 ºC for two hours, the emission band of the newly obtained sample 4a shows a decreased intensity to almost 50 % compared to the initial emission intensity of sample

4. This observation is also confirmed by the images of the samples under UV illumination (Fig. 57).

The (re)oxidation of Eu^{2+} to Eu^{3+} during the thermal treatment cannot be responsible for this obvious worsening of the luminescent properties, since no other bands appear on the emission spectrum of sample 4a and the position of the emission band is virtually identical to the one before annealing. Moreover, in terms of phase composition or crystallite size no significant changes were noticed as a result of the annealing step (Fig. 55).

A possible explanation for this behavior could be the presence of the structural defects – mainly oxygen vacancies [226] and residual stress [210] – present in the powders resulted from the combustion reactions. As a matter of fact, Zhang [226] et al. have already evidenced the existence of these oxygen vacancies in the $BaAl_2O_4$ structure obtained under reducing atmosphere, and their importance on $BaAl_2O_4$ optical properties.

The presence of the structural defects is the most plausible hypothesis, considering the particular synthesis conditions in the case of combustion reaction: the temperature of the reaction mixture increases from 400 ºC up to well over 1200 ºC in less than 40 seconds. This means that the sample is being heated and then cooled down very fast in a reducing atmosphere caused by the excess urea, which makes the structural equilibrium impossible to be attained.

As a result, a tensioned, full of defects structure is obtained, having a positive influence upon the luminescent properties. In addition, one may also take into account that, same as the case of $Sr_{1-x-y}Eu_xDy_yAl_2O_4$ [213,227], the Ba^{2+} substitution by Eu^{2+} and Dy^{3+} generates structural defects, such are oxygen vacancies. Some of these defects are eliminated during the subsequent thermal treatment at 1200 ºC for 2 hours in air and the sample approaches equilibrium, with the intensity of the emission radiation decreasing consequently.

Unlike other authors [218] reporting that supplementary annealing does not influence the luminescent properties of the phosphors obtained via combustion synthesis, we found that the thermal treatment has a dramatic effect upon the emission intensity. Moreover, the visual observation of the decay time in the case of samples 4 and 4a also confirmed the negative effect of annealing upon the emission time. After exposing both samples to visible light, the afterglow of sample 4 could be observed with the clear eye for about 30 minutes, whilst no afterglow was seen in sample 4a. This behavior represents an additional argument supporting the previous hypothesis concerning the importance of the structural defects (oxygen vacancies) upon the luminescent properties of combustion-synthesized $BaAl_2O_4$: Eu^{2+}, Dy^{3+}.

Regardless of the Eu^{2+} proportion, the emission spectra were very similar, showing a single emission band with a maximum at 499 nm (Fig. 59). The increase of the Eu^{2+} proportion from 0.005 to 0.020 leads to a slight increase of the emission intensity. However, it seems that the Dy^{3+}/Eu^{2+} ratio has a much more important influence upon the emission intensity, than the Eu^{2+} proportion (Fig. 58).

Key findings
- ✓ Using $Ba(ClO_4)_2$ together with urea and glycine fuel mixture proved to be a viable choice for obtaining $BaAl_2O_4$: Eu^{2+}, Dy^{3+} phosphors via solution combustion synthesis, as no further annealing was required. The average crystallite size of the samples varied between 72 and 82 nm and the BET specific surface area was ≈ 1.4 m^2/g.

- ✓ The emission spectra of the obtained $BaAl_2O_4$: Eu^{2+}, Dy^{3+} phosphors show a single band at 499 nm. Increasing the Eu^{2+} proportion from 0.005 to 0.020 led to a slight increase of the emission band (499 nm) intensity.
- ✓ The presence of Dy^{3+} considerably improves the afterglow without modifying the wavelength of the emitted radiation. For the same Eu^{2+} proportion, increasing the Dy^{3+}/Eu^{2+} ratio from 0/1 to 3/1 contributes to a sharp increase of the emission band (499 nm) intensity.
- ✓ Supplementary annealing of the samples obtained directly from the combustion reaction resulted in significant deterioration of the optical properties of $BaAl_2O_4$: Eu^{2+}, Dy^{3+}, as a consequence of reducing the concentration of structural defects (oxygen vacancies and residual stress).

2.1.3. Hydrogen peroxide treatment – an effective method for carbon removal

The specific surface area of metal oxides is depending on the preparation route but also on the synthesis temperature; usually the lower the synthesis temperature, the larger the surface area. However, in some cases, lower annealing temperatures lead to the contamination of desired phase with residual carbon originating from the incomplete organic material oxidation. Since the increase of the annealing temperature is not an option, as the specific surface area would significantly decrease, the candidate suggested and tested an ingenious solution [29,32]: chemical oxidation of residual carbon by hydrogen peroxide. Basically, this solution relies on treating the ceramic powder, such as $ZnAl_2O_4$ [32] or γ-Fe_2O_3 [29], which contains residual carbon with hydrogen peroxide, followed by drying. The organic carbon residues are oxidized by H_2O_2, preserving or sometimes increasing the specific surface area of metal oxides.

2.1.3.1. Chemical oxidation of residual carbon from ZnAl₂O₄ powders

For example, the removal of carbon residue from $ZnAl_2O_4$ nanopowders by annealing at 500–800 °C leads to a decrease of specific surface area from 228.1 m^2/g to 47.6 m^2/g. At the same time, the average crystallite size increased from 5.1 nm to 14.9 nm. In order to overcome these drawbacks, a new solution for removing the carbon residue has been suggested [32]: chemical oxidation using hydrogen peroxide. This work was supported by a grant of the Romanian National Authority for Scientific Research, CNCS – UEFISCDI, project number PN-II-RU-TE-2011-3-0024 (18/05.10.2011). In terms of carbon removal, an H_2O_2 treatment for 8 hours at 107 °C proved to be equivalent to a heat treatment of 1 hour at 600 °C. The benefits of chemical oxidation over thermal oxidation were obvious. The specific surface area was much larger (188.1 m^2/g) in the case of the powder treated with H_2O_2. The average crystallite size (5.8 nm) of $ZnAl_2O_4$ powder treated with H_2O_2 was smaller than the crystallite size (8.2 nm) of the $ZnAl_2O_4$ powder annealed at 600 °C.

General context: the removal of carbon residue from ceramic powders prepared by "soft chemical routes" has always been a delicate issue. Usually, the complete removal of carbon by annealing under air atmosphere requires not only a sufficiently high temperature (usually above 700 °C) but also a significant period of time (several hours).

On the other hand, there are many literature reports describing various "soft chemical routes" of preparing high reactivity ceramic nanopowders: citrate [80,228,229], combustion synthesis [230,231], Pechini [232,233], sol-gel [234-237], organic precursors [238] etc. The efficiency of these methods can be assessed in terms of lower annealing temperature, shorter soaking time and superior characteristics of the resulting product (nanocrystalline character, large specific surface area, small grain size, lower agglomeration degree).

For instance, it is reported that $ZnAl_2O_4$ may be obtained at 500–600 ºC by using the citrate method [229]. However, the as-prepared powders cannot be pressed and then sintered due to the presence of large amount of residual carbon originating from the incomplete oxidation of the organic material. Although the formation of the $ZnAl_2O_4$ takes place at $\approx$ 550 ºC, the complete removal of the residual carbon requires a heat treatment of 2 hours at 800 ºC [229].

The preparation of α-Al_2O_3, corundum, powder by thermal decomposition of complex combination derived from sucrose and aluminum nitrate is another eloquent example. According to the results reported by Das et al. [239], after annealing the sucrose-aluminum nitrate precursor at 600 °C for 4 hours a gray powder of α-Al_2O_3 is obtained. In this case, the complete removal of carbon material can be achieved only after a heat treatment of 12 hours at 600 °C [239].

Powder annealing at temperatures 200 °C higher than the minimum temperature where the designed crystalline phase is formed leads to the decrease of specific surface area and amplifies grain growth and agglomeration phenomena.

Experimental: table 15 shows the starting raw materials, which were used for solution combustion synthesis of $ZnAl_2O_4$ powder. The $Zn(NO_3)_2 : Al(NO_3)_3 : C_6H_{18}N_4$ molar ratio of 7:14:20 corresponds to a $C_6H_{18}N_4$ (triethylenetetramine) excess of 300 %.

Table 15. Raw materials used in the present experiments

Sample	$Zn(NO_3)_2 \cdot 4H_2O$	$Al(NO_3)_3 \cdot 9H_2O$	$C_6H_{18}N_4$	H_2O_2
Manufacturer	Merck	Merck	Riedel-de Haën	Silal Trading
Purity	pro analysi	pro analysi	pro analysi	pro analysi
M (g/mol)	261.44	375.13	146.24	34.01
c (%)	≥ 98.5	≥ 98.5	-	30
ρ (g/cm^3)	-	-	0.98	-

The recipe was designed in order to obtain 70.0 g of $ZnAl_2O_4$. After dosing and mixing the starting materials (Fig. 60) in distilled water, a clear solution was obtained. In the next step, the porcelain dish containing the precursor solution has been placed in a heating mantle, preheated at 400 °C. As the temperature of the precursor solution increases, most of the water evaporates and an exothermic combustion reaction occurs.
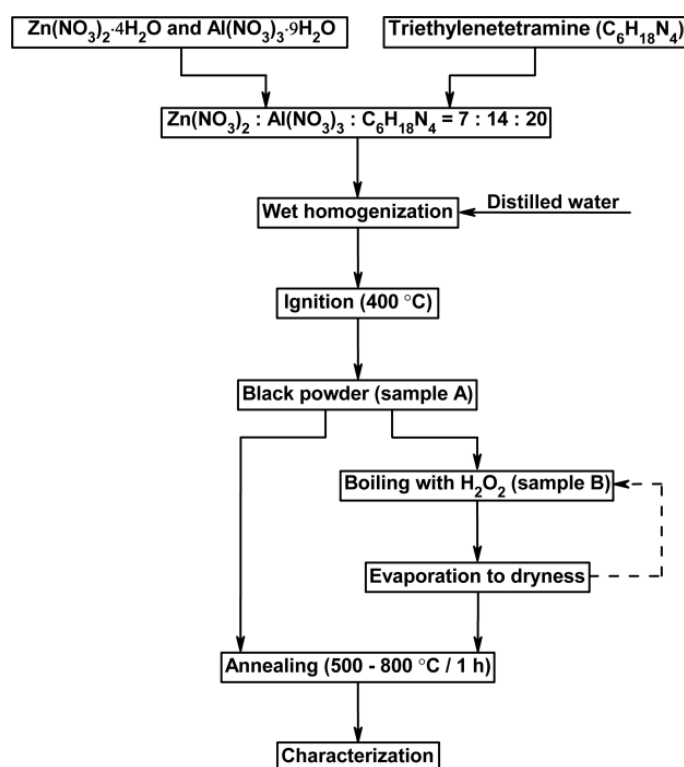

Fig. 60. The general preparation scheme of $ZnAl_2O_4$ powders.

During this process (5 minutes) the raw material mixture reaches dark red incandescence and large amounts of gases evolve, typical for smoldering combustion. The fluffy material which

resulted after the combustion process was hand-crushed with a pestle, resulting a black powder (denoted as sample A).

Small portions of sample A were annealed for 1 hour at temperatures ranging from 500 °C to 800 °C. Another portion of the black powder resulted from the combustion reaction (sample A), was treated with a concentrated solution of hydrogen peroxide, H_2O_2, followed by heating at 107 °C under continuous magnetic stirring at 500 rpm. For every gram of powder, 20.0 mL of H_2O_2 were used. After 8 hours, the color of the powder treated with H_2O_2 (denoted as sample B) turned from black to light gray and the sample was evaporated to dryness.

Subsequently, small portions of powder B were annealed in the same conditions as sample A (Fig. 60). The heating behavior of samples A and B was monitored by thermal analysis, using a Netzsch 449 C instrument equipped with Pt crucibles. The TG–DTA curves were recorded under an artificial air flow of 20 mL/min, at a heating rate of 10 °C/min.

The carbon, nitrogen and hydrogen content of the powders (CNH elemental analysis) was determined by ''Dynamic Flash Combustion'' using an Elemental Analyzer EA 1108 according to ASTM D 5373-08 standard test procedures.

The phase composition of the powders was determined by X-ray diffraction, using a Panalytical XPERT-PRO diffractometer operating at 45 kV and 30 mA. The X-ray diffraction patterns were recorded using the Ni filtered $Cu_{K\alpha}$ radiation. The crystallite size was calculated based on the Scherrer's equation (1), using the fallowing hkl peaks: 311, 220 and 440. The lattice parameter of cubic $ZnAl_2O_4$ was calculated based on the X-ray diffraction patterns, using equation (9).

BET (Brunauer-Emmet-Teller) specific surface area of the powders was measured by $N_2(g)$ adsorption technique using a Micromeritics ASAP 2020 instrument. The equivalent grain diameter was calculated based on the BET specific surface area (2), considering a theoretical density of $ZnAl_2O_4$ of 4.62 g/cm^3.

The two series of powders were also characterized by Fourier-transform infrared spectroscopy, using a Shimadzu PRESTIGE-21 FT–IR spectrometer in the range of 400–4000 cm^{-1} with KBr pellets.

The color of the samples was investigated by diffuse reflectance spectrophotometry. CIEL*a*b* parameters were measured using a Varian Cary 300 Bio UV-VIS spectrophotometer (illuminant - D_{65}, observer angle - 10°). L* is a measure of brightness: L* = 100 corresponds to the total reflection of radiation from the VIS range (white), whilst L* = 0 corresponds to the complete absorption of radiation from the VIS range (black). Negative values of a* indicates the proportion of green. Positive values of a* indicates the proportion of red. Negative values of b* indicates the proportion of blue. Positive values of b* indicates the proportion of yellow.

Results and discussion: the combustion reaction evolved as a typical smoldering process (Fig. 61), meaning that the reaction front propagated very slowly. The combustion temperature was not very high, as the sample hardly reached incandescence. The powder obtained at the end of the combustion process had a black color, which indicates the presence of residual carbon (Table 16), derived from partial oxidation of triethylenetetramine. The CNH elemental analysis of the sample resulted from the combustion process (Table 16) confirmed that the powder contains 6.1 % carbon as well as small amounts of nitrogen (2.8 %) and hydrogen (1.0 %).
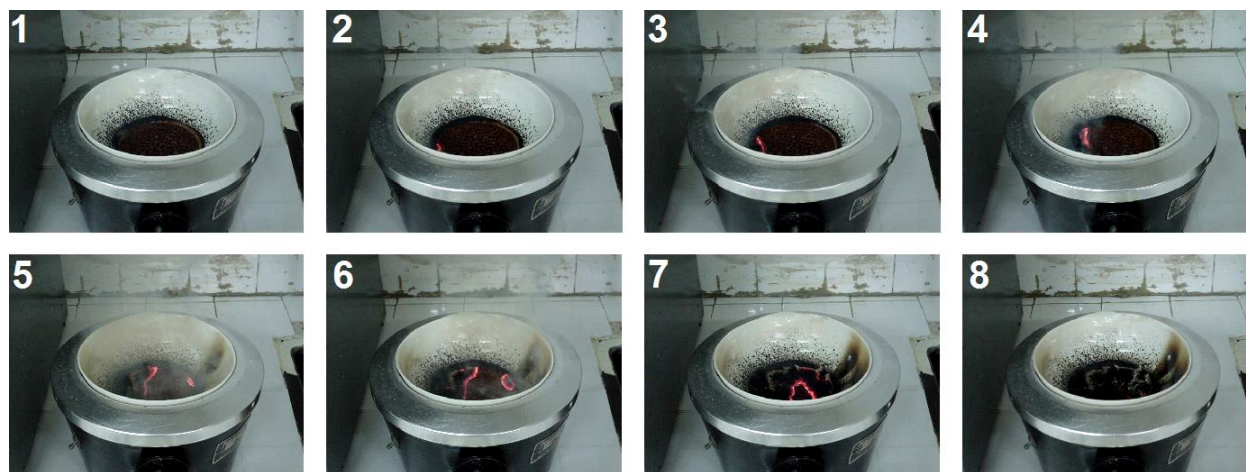
Fig. 61. Images recorded during the preparation of ZnAl$_2$O$_4$ powder by combustion synthesis.

Table 16. CNH elemental analysis, lattice parameter, crystallite size, specific surface area and the equivalent grain size of the samples

Sample	CNH elemental analysis [wt.%]			a^1 [Å]	D_{XRD} [nm]	S^3 [m^2/g]	D_{BET} [nm]	D_{BET}/D_{XRD}
	C	N	H					
A	6.1	2.8	1.0	8.089	5.1	228.1	5.7	1.14
A$_{500}$	0.5	0.1	0.7	-	-	160.3	8.1	-
A$_{600}$	0.4	0.1	0.4	8.087	8.2	113.0	11.5	1.40
A$_{800}$	-	-	-	8.084	14.9	47.6	27.3	1.83
B	0.4	0.8	1.3	8.087	5.8	188.1	6.9	1.19
B$_{500}$	0.3	0.1	0.7	-	-	164.1	7.9	-
B$_{600}$	0.2	0.1	0.6	8.085	7.4	133.7	9.7	1.31
B$_{800}$	-	-	-	8.083	13.2	67.5	19.2	1.45

1 – lattice parameter, 2 – crystallite size, 3 – specific surface area, 4 – equivalent grain diameter.

Thermal analysis of the precursor solution containing Zn(NO$_3$)$_2$, Al(NO$_3$)$_3$ and C$_6$H$_{18}$N$_4$ (Fig. 62) reveals that up to 100 °C, the sample undergoes an endothermic process (82 °C), which is accompanied by a mass loss of about 18 %. Most probably, the phenomenon occurring in this case is the elimination of water from the aqueous solution.
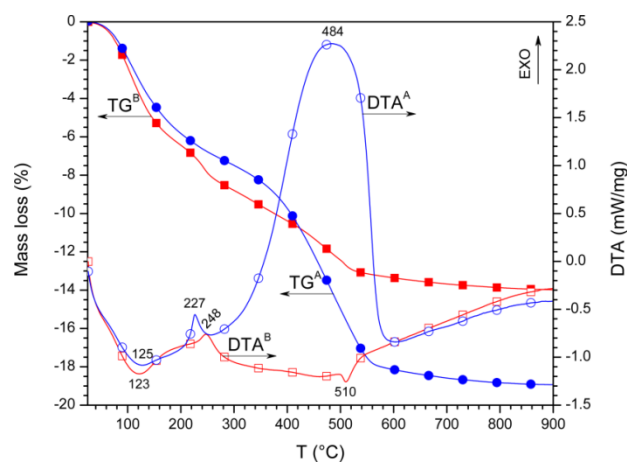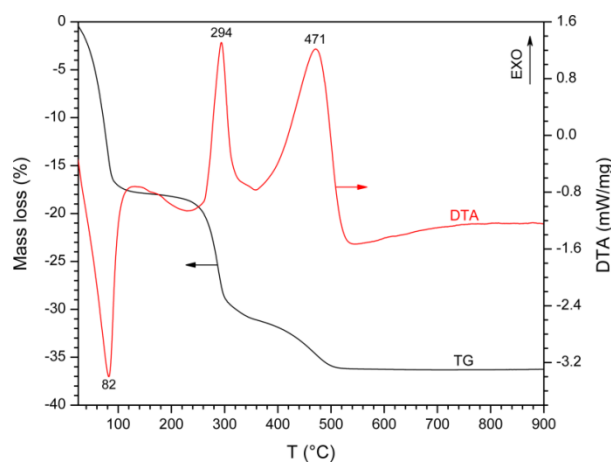
Fig. 62. TG–DTA curves of the precursor solution.

Fig. 63. TG–DTA curves of powders A, B.

.

As the temperature increases, the ignition of the combustion reaction occurs. This process is characterized by a steep and significant mass loss on the TG curve (Fig. 62) which is accompanied by a sharp exothermic effect on the DTA curve (294 °C). Since the black powder resulting from the combustion has a carbon content of 6.1 % (Table 16), one can assume that the second exothermic effect (471 °C) – which is also accompanied by a mass loss – may be assigned to burning out the residual carbon (thermal oxidation). The shape of TG and DTA curves suggests that above 500 °C sample undergoes no further transformations. Thermal analysis of the black powder prepared by combustion synthesis (sample A) indicates that during heating 3 major processes occur (Fig. 63). The DTA curve of sample A shows an endothermic effect at 125 °C, which is accompanied by a mass loss on the TG curve, corresponding to the removal of the adsorbed moisture.

Another process occurs at 227 °C and it is characterized by a slight mass loss on the TG curve, which may be related to a small exothermic reaction between traces of amorphous metal nitrates and triethylenetetramine. The presence of traces of amorphous metal nitrates and triethylenetetramine in the powder resulted from the combustion reaction is supported by the CNH elemental analysis (Table 16), which indicated that sample A contained 6.1 % carbon as well as small amounts of nitrogen (2.8 %) and hydrogen (1.0 %). As the temperature increases, the DTA curve exhibits a broad exothermic effect in the temperature range of 300–600 °C (with a maximum at 484 °C), which is assigned to burning out the residual carbon (thermal oxidation). The removal of residual carbon is marked on the TG curve as a significant mass loss (Fig. 63).

After 8 hours of mixing and heating at 107 °C, the color of the powder treated with H_2O_2 (sample B) turned from black to light gray (Fig. 64). Considering that pure $ZnAl_2O_4$ is white, this color change suggests that the sample treated with hydrogen peroxide (sample B) contains less carbon residue than the mother sample A.
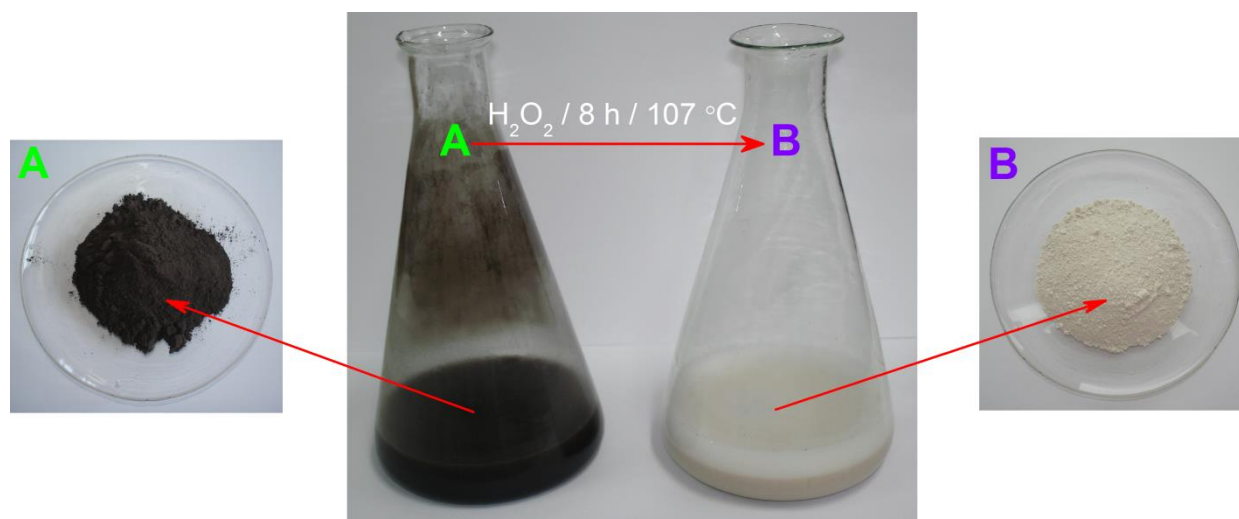
Fig. 64. Digital images of powders A and B.

The CNH elemental analysis confirms these results (Table 16): the mother sample A has a carbon content of 6.1 % whilst the sample treated with H_2O_2 (sample B) has a carbon content of only 0.4 %. The carbon content decreased radically, which indicates that hydrogen peroxide, H_2O_2, was able to chemically oxidize the residual carbon. As a matter of fact in the field of soil analysis hydrogen peroxide is often used as a pretreatment reagent for organic matter removal

[240,241]. However, this would be for the first time when hydrogen peroxide is used for the removal of carbon residue from ceramic powders, as there are no such reports in the literature.

Thermal analysis of the sample treated with H_2O_2 (sample B) revealed that over the temperature range of 25–300 °C, the TG–DTA curves of sample B (Fig. 63) resemble quite well the TG–DTA curves of sample A. However, instead of a broad exothermic effect, which appears on the DTA curve at 484 °C (denoting the residual carbon burnout), the DTA curve shows only a small endothermic effect at 510 °C, indicating a possible decomposition process.

Besides the visible color change of the powder treated with H_2O_2 (Fig. 64), the TG curves of samples A and B revealed an important difference between the total mass loss of the two samples. From this point of view, one may notice that the total mass loss of sample B (13.9 %) is significantly smaller than the total mass loss of sample A (18.9 %), which confirms once more the carbon removal during the hydrogen peroxide treatment (Fig. 63).

X-ray diffraction analysis revealed that the only crystalline phase present in the powder resulting from the combustion reaction (sample A) is the spinel-structured $ZnAl_2O_4$, known as gahnite (Fig. 65). The average crystallite size of $ZnAl_2O_4$ is 5.1 nm. Based on the results obtained by X-ray diffraction and the CNH analysis of sample A, one can assume that the combustion synthesized powder is a mixture of $ZnAl_2O_4$ and amorphous carbon. After annealing the A powder at 600 °C and 800 °C for 1 hour, a slight increase of the crystallite size could be observed, to 8.2 nm and 14.9 nm (Table 16).
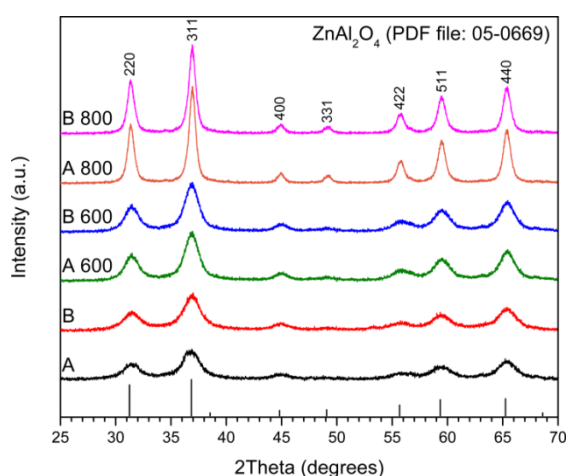
Fig. 65. XRD patterns of the samples before and after annealing 1 hour at 600 °C and 800 °C.
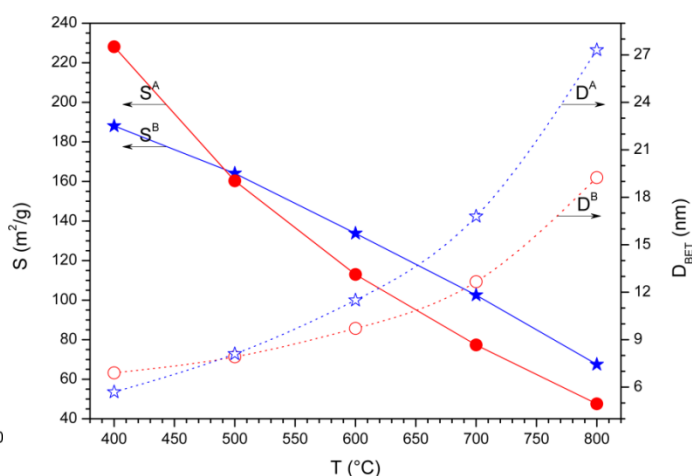
Fig. 66. The evolution of specific surface area and equivalent grain diameter of samples A and B as a function of the annealing temperature.

The XRD pattern of sample B is very similar to the one of sample A (Fig. 65), indicating that $ZnAl_2O_4$ is the only crystalline phase. The average crystallite size of $ZnAl_2O_4$ is 5.8 nm. Therefore, in terms of phase composition, there is virtually no difference between powder A and powder B, treated with H_2O_2. After annealing powder B at 600 °C and 800 °C for 1 hour, a slight increase of the crystallite size could be observed, to 7.4 nm and 13.2 nm respectively (Table 16).

After performing the sample degassing operation at 400 °C, the specific surface area of sample A (228.1 m^2/g) proved to be larger than the specific surface area of sample B (188.1 m^2/g) (Table 16). Taking into account the CNH elemental analysis (Table 16), this decrease of the surface area may be explained by the removal of fine carbon fraction as a result of H_2O_2

treatment. The removal of carbon grains by H_2O_2 oxidation is also supported by the evolution of cumulative pore volume, which decreases from 0.33 cm^3/g (sample A) to 0.28 cm^3/g (sample B).

Figure 66 shows the evolution of specific surface area and equivalent grain diameter of samples A and B as a function of the annealing temperature. As the annealing temperature increases, the carbon content of the samples decreases, but so does the specific surface area (Table 16). In this case, the traditional carbon removal by annealing has major side effects on the other powder properties, such as specific surface area and grain size. In order to reach the same carbon content as the sample treated with H_2O_2 (sample B), mother sample requires annealing at 600 °C for one hour (sample A_{600}) (Table 16). However, the specific surface area of sample B is 188.1 m^2/g, whilst the specific surface area of sample A_{600} decreased by almost 40 %, to 113.0 m^2/g. Thus, the solution we report hereby allows the elimination of carbon residue by H_2O_2 chemical oxidation, without altering the other powder properties.

On the other hand, the specific surface area of both samples (A and B) decreases as the annealing temperature increases (Fig. 66). Yet, the specific surface area decreases to a higher extent in the case of sample A. Moreover, it is quite obvious that above 500 °C, the specific surface of sample B is larger than the one of sample A. Even at 800 °C, powder B has a specific surface of 67.5 m^2/g, which is ≈42 % higher than the specific surface area of sample A, 47.6 m^2/g (Table 16). In the case of both sample series (A and B), the equivalent grain diameter increases with increasing the annealing temperature. The evolution of equivalent grain diameter as a function of temperature suggests that A grains are growing much faster than B grains. At 800 °C the A grains (27.3 nm) are ≈42 % larger than the B grains (19.2 nm).

FT–IR spectra of samples A and B, before and after annealing for 1 hour at 600 °C and 800 °C are shown in Fig. 8. The large specific surface area of the powders enables the rapid adsorption of H_2O and CO_2 from the atmosphere, as evidenced by the FT–IR spectra of the samples (Fig. 67). The broad band at 3430 cm^{-1} may be assigned to the stretching vibration of H_2O molecules, whilst the band from 1640 cm^{-1} is attributed to H_2O bending.
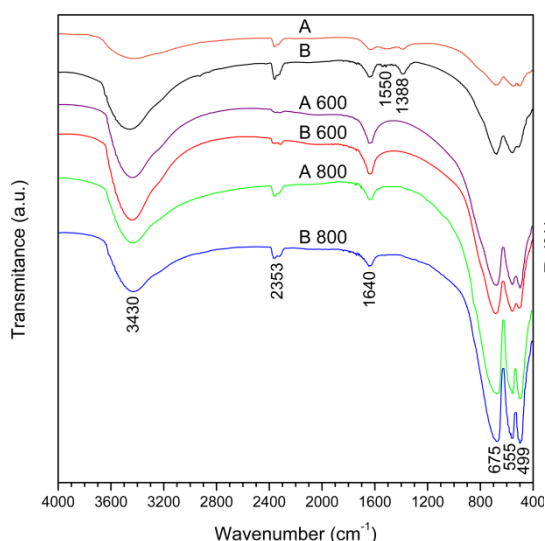
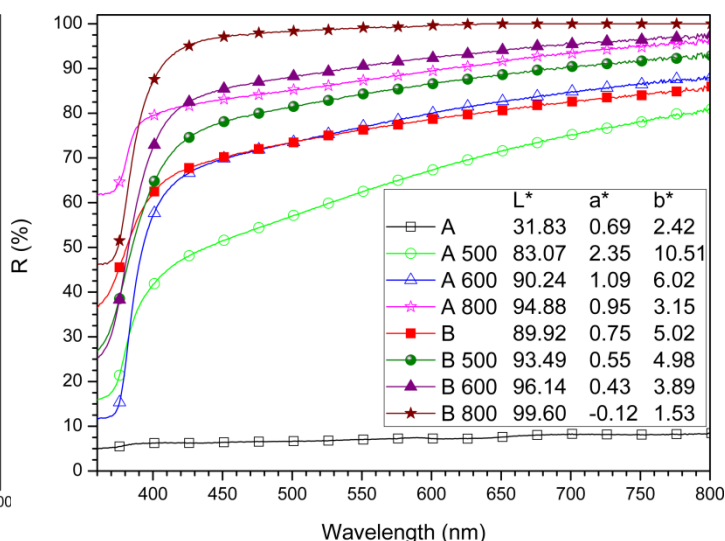Fig. 67. FT–IR spectra of the samples before and after annealing 1 hour at 600 °C and 800 °C.

Fig. 68. DRS spectra and CIEL*a*b* parameters of samples A and B before and after annealing at various temperatures.

The absorption band at 2353 cm^{-1} is due to the stretching vibration of CO_2. The bands at 675, 555 and 499 cm^{-1} confirm the formation of normal spinel structure, $ZnAl_2O_4$, as evidenced

by the XRD analysis (Fig. 65). The band at 1388 cm^{-1} may be assigned to nitrate anion, which suggests that combustion reaction did not reach completion. Considering that an excess of triethylenetetramine has been used, it is likely that small amounts of triethylenetetramine may also exist within powders A and B, which agrees with the CNH elemental analysis (Table 16).

While the presence of –NH$_2$ stretch band (around 3400 cm^{-1}) cannot be clearly identified on the FT-IR spectra of samples A and B because of its overlapping with the H$_2$O stretch band, one may observe the bending vibration of –NH$_2$ group at 1550 cm^{-1}. Furthermore, as shown by the TG-DTA analysis of samples A and B (Fig. 62), the combustion reaction between traces of metal nitrates and triethylenetetramine is responsible for the small exothermic effect, which occurs at 227–248 °C. From this point of view, there is an excellent correlation of the TG-DTA results (Fig. 62) and the disappearance of nitrate and –NH$_2$ bands (1388 cm^{-1} and 1550 cm^{-1} respectively) after annealing at 600 °C. As the annealing temperature increases the typical bands of ZnAl$_2$O$_4$ (675, 555 and 499 cm^{-1}) increase in intensity, which indicates a more advanced crystallinity degree of ZnAl$_2$O$_4$, in agreement with the XRD analysis (Fig. 65).

The influence of the H$_2$O$_2$ treatment and the annealing temperature on the color of samples A and B has been studied by means of diffuse reflectance spectroscopy and CIEL*a*b* parameters (Fig. 68). The black color of sample A, which contains 6.1 % carbon, is illustrated by the intense unselective absorption of the VIS radiation (Fig. 68) and the low value of the brightness parameter, L* = 31.83. On the other hand, after the H$_2$O$_2$ treatment, sample B, which contains 0.4 % carbon, shows much higher value of the brightness parameter, L* = 89.92 (Fig. 68), which is in agreement with the light gray color of the powder (Fig. 64).

After analyzing the CIEL*a*b* parameters shown in Fig. 68, one may notice that the brightness, L*, increases as the annealing temperature increases, due to the removal of carbon residue. The samples treated with H$_2$O$_2$ show higher brightness and higher reflectance than the samples A annealed at the same temperature. Actually, in terms of brightness there are only minor differences between sample B and sample A$_{600}$ annealed at 600 °C for one hour.

In terms of color and carbon content (Table 16), a hydrogen peroxide treatment of 8 hours at 107 °C (sample B) is virtually equivalent to a heat treatment applied to sample A$_{600}$ of 1 hour at 600 °C. In terms of other measurable properties of the powder, such as specific surface area or equivalent grain size diameter, the balance tilts in favor of sample B, which allows obtaining powders with smaller grain size and higher specific surface are (Table 16). In addition, the D$_{BET}$/D$_{XRD}$ ratio suggests that the agglomeration degree of A crystallites is higher than the agglomeration degree of B crystallites, which means that the number of crystallites in A grains is higher than the number of crystallites in B grains.

Key findings
✓ Carbon impurified ZnAl$_2$O$_4$ resulted from the combustion reaction of zinc nitrate, aluminum nitrate and triethylenetetramine. The removal of carbon residue by annealing at temperatures of 500–800 °C promoted a substantial decrease of specific surface area from 228.1 m^2/g to 47.6 m^2/g. At the same time, an increase of the average crystallite size was noticed, from 5.1 nm to 14.9 nm.

✓ In order to overcome these drawbacks a new solution to remove the carbon residue from ZnAl$_2$O$_4$ powders has been suggested. This alternative relies on the chemical oxidation of carbon residue by hydrogen peroxide rather than thermal oxidation (annealing).

- ✓ In terms of color, the CIEL*a*b* measurements indicated that an H_2O_2 treatment for 8 hours at 107 °C is equivalent to a heat treatment of 1 hour at 600 °C. The benefits of chemical oxidation instead of thermal oxidation of residual carbon were obvious.
- ✓ The specific surface area of the powder treated with H_2O_2 was much larger (188.1 m^2/g) than the specific surface area of the powder annealed at 600 °C (113.0 m^2/g). At the same time, the crystallite size (5.8 nm) and the equivalent grain size diameter (6.9 nm) of the powder treated with H_2O_2 were smaller when compared to the crystallite size (8.2 nm) and the equivalent grain size diameter (11.5 nm) of the powder annealed at 600 °C.

2.1.3.2. γ-Fe$_2$O$_3$ nanoparticles prepared by combustion synthesis

In a paper, partly supported by the Sectorial Operational Programme Human Resources Development (SOPHRD), financed by the European Social Fund and the Romanian Government under the contract number POSDRU 141531, the candidate reported that the combustion reaction product between iron nitrate and glucose is a black powder of γ-Fe$_2$O$_3$ contaminated with residual carbon [29]. After the H$_2$O$_2$ treatment, the carbon residue is removed, so that the carbon content decreases from 32.7 % to 0.4 %, and the color of the sample changes from black to reddish brown. Simultaneously the BET surface area of γ-Fe$_2$O$_3$ increases dramatically from 72.6 m^2/g to 149.0 m^2/g. The resulted γ-Fe$_2$O$_3$ particles have a round shape and an average size of 12 nm. The average crystallite size of γ-Fe$_2$O$_3$ calculated from XRD patterns was 5 nm. The resulted γ-Fe$_2$O$_3$ nanoparticles exhibit a superparamagnetic behavior and a saturation magnetization of 41.5 emu/g. In addition to the removal of residual carbon, the H$_2$O$_2$ treatment also ensures the sterilization of γ-Fe$_2$O$_3$ particles, which is a key requirement in the field of biomedical applications. γ-Fe$_2$O$_3$ nanoparticles coated with a double layer of oleic acid were dispersed in saline solution, leading to a stable colloidal suspension. DLS measurements indicated a unimodal distribution of γ-Fe$_2$O$_3$ nanoparticles and a hydrodynamic diameter of 80 nm [29]. The obtained results suggest that the procedure described hereby might be a promising candidate for obtaining pure γ-Fe$_2$O$_3$ nanoparticles, suitable for biomedical applications.

General context: in the last decades, much research has been focused on the synthesis of γ-Fe$_2$O$_3$, maghemite, nanoparticles [242-247]. γ-Fe$_2$O$_3$ is considered as one of the most desirable materials for biomedical applications, due to its inherent biocompatible nature, (superpara)magnetic properties as well its stability towards oxidation [248-252].

Because of its remarkable properties, γ-Fe$_2$O$_3$ nanoparticles are widely used in biomedical applications, such as magnetic resonance imaging, targeting drug delivery, hyperthermia, detoxification, magnetic paper [253-258]. At the same time there is an increased interest in using maghemite nanoparticles for the removal of various pollutants (As^{5+}, Cr^{6+}, dyes) from wastewaters [244,259-261].

Several synthesis routes have been developed for the preparation of γ-Fe$_2$O$_3$ nanoparticles in an attempt to control the particle size and shape, size distribution and magnetic properties: co-precipitation [259-261], microemulsions [262], thermal decomposition [263], laser pyrolysis [264], flame spray pyrolysis [265,266], sol-gel [267], plasmachemical synthesis [268] etc. Although the synthesis of γ-Fe$_2$O$_3$ nanoparticles has seen substantial progress, the preparation of pure, large surface area γ-Fe$_2$O$_3$ nanopowders is still one of the top priorities in the field.

Recently, combustion synthesis proved to be a simple, fast, eco-friendly and low cost method for the preparation of many metal oxide nanoparticles [4]. However, there are few reports on the combustion synthesis of γ-Fe$_2$O$_3$ nanopowders [269,270].

Experimental: 0.140 moles of Fe(NO$_3$)$_3$·9H$_2$O (Roth, 96 %) and 0.179 moles of D-(+)-C$_6$H$_{12}$O$_6$ (Riedel-de Haën, 99 %) were dissolved in 40 mL of distilled water in a round bottom flask, according to the general preparation scheme shown in Fig 69. The flask containing the aqueous solution was placed inside a heating mantle at 400 °C. As the solution was heated up, a smoldering combustion reaction occurred between iron nitrate and glucose. During this process, large amounts of gases were released. The evolving gases were bubbled in a beaker filled with distilled water, as described in detail in [27].
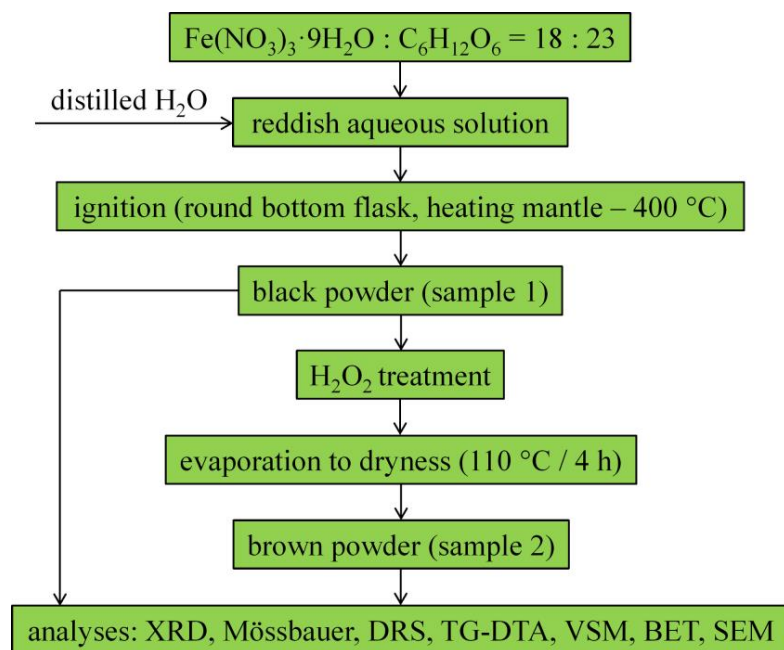
$$Fe(NO_3)_3 \cdot 9H_2O : C_6H_{12}O_6 = 18 : 23$$

distilled H_2O → reddish aqueous solution

ignition (round bottom flask, heating mantle – 400 °C)

black powder (sample 1)

H_2O_2 treatment

evaporation to dryness (110 °C / 4 h)

brown powder (sample 2)

analyses: XRD, Mössbauer, DRS, TG-DTA, VSM, BET, SEM

Fig. 69. General preparation scheme of γ-Fe_2O_3 nanopowders.

After 30 minutes the gas evolution stopped and a black voluminous powder was obtained, hereinafter referred to as sample 1. Half of this powder was subsequently treated with H_2O_2 (Silal trading, 30 %) under mechanical stirring, followed by evaporation to dryness (Fig. 69). Each gram of powder was treated with 50 mL of H_2O_2.

After evaporation to dryness, a reddish brown powder was obtained, hereinafter referred to as sample 2. 0.7 g of sample 2 was sonicated for 2 hours and then the particles were coated with a double layer of oleic acid (Merck, 65-88 %). The oleic acid double layer coated nanoparticles were dispersed in 25 mL of saline solution (Sigma Aldrich), leading to a stable colloidal suspension.

The phase composition of the samples was investigated by X-ray diffraction using a Rigaku Ultima IV instrument operating at 40 kV and 40 mA. The XRD patterns were recorded using $Cu_{K\alpha}$ radiation. Crystallite size was calculated using the PDXL 2.0 software.

The Mössbauer spectra measurement was done in the transmission mode with ^{57}Co diffused into a Rh matrix as the source moving with constant acceleration. The spectrometer (Wissel) was calibrated by means of a standard α–Fe foil and the isomer shift was expressed with respect to this standard at 20 °C. The samples were measured at the temperature of 20 °C. The fitting of the spectra was performed with the help of the NORMOS program.

The heating behavior of the samples was studied over the range of 25–1000 °C by thermal analysis, using a Netzsch 449 C instrument. TG-DTA curves were recorded using Pt crucibles, under an artificial air flow of 20 mL/min, at a heating rate of 10 °C/min.

The color of the samples was investigated by diffuse reflectance spectrophotometry. CIEL*a*b* parameters were measured using a Varian Cary 300 Bio UV-VIS spectrophotometer (illuminant – D_{65}, observer angle – 10°).

The carbon content of the samples was determined by "Dynamic Flash Combustion" using an Elemental Analyzer CNH EA 1108, according to ASTM D 5373-08 standard test procedure.

After the samples were degassed for 12 hours at 100 °C and 5 μmHg, nitrogen adsorption-desorption isotherms were recorded using a Micromeritics ASAP 2020 instrument at

77 K. The specific surface area was calculated using the Brunauer–Emmett–Teller (BET) method. Micropore area, external surface area and micropore volume were calculated using the t-plots. Cumulative volume of pores was computed using the Barrett–Joyner–Halenda (BJH) method from the desorption branch of the isotherms.

The magnetic properties of the powders were measured at room temperature by vibrating sample magnetometry using a VSM 880 ADE/DMS instrument.

The particle size and morphology were explored by scanning electron microscopy (SEM), using a FEI Quanta FEG 250 microscope. In addition, a drop of diluted colloid was placed on a lamella and allowed to air-dry, and SEM images were subsequently recorded. The resulted colloidal suspension was characterized by dynamic laser scattering, DLS, using a ZetaSizer NanoZS Malvern Instrument.

Results and discussion: the XRD pattern of the black powder resulting from the combustion reaction is shown in Fig. 70. In this case, the peak assignment to γ-Fe_2O_3 and/or Fe_3O_4 phase is a difficult task, because both, γ-Fe_2O_3 and Fe_3O_4, crystallize in the cubic system, and both species show diffraction peaks at very close 2θ angles [271].
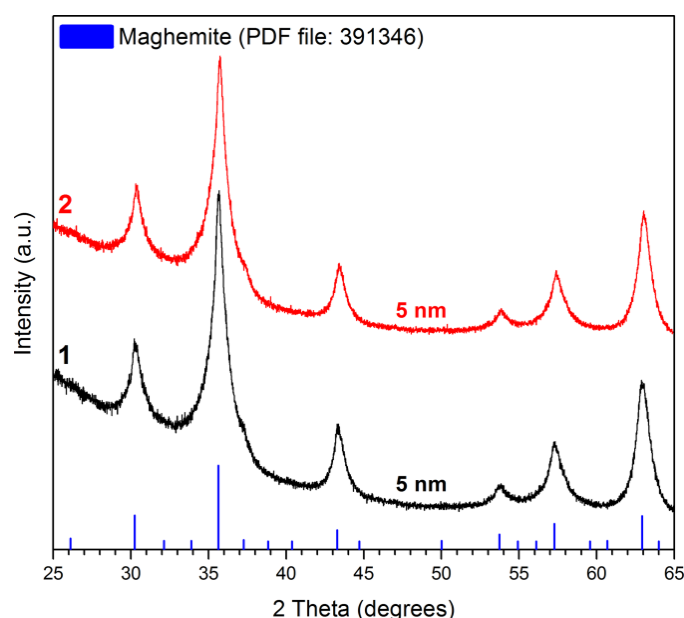
Fig. 70. XRD patterns of the powders before (1) and after (2) the H_2O_2 treatment.

The problem is even more complicated since the peaks are quite broad, suggesting the presence of small crystallites. For a proper interpretation of the diffraction pattern, sample 1 was subjected to Mössbauer analysis (Fig. 71). From the isomer shifts of the subspectra 1 and 2 can be seen that sample 1 contains only Fe^{3+}. The absence of Fe^{2+} in sample 1 proves that no Fe_3O_4 has been formed. This means that the diffraction peaks can be precisely assigned to γ-Fe_2O_3 (Fig. 70), having an average crystallite size of 5 nm. Subspectrum 1 corresponds to the Fe^{3+} (76 % of total iron in the sample), which is not in the magnetically ordered structure (Table 17). Most likely this is related to the presence of superparamagnetic γ-Fe_2O_3 with particle size less than 10 nm, as confirmed by the average crystallite size calculated from the XRD pattern. Subspectrum 2 corresponds to the Fe^{3+} (24 % of total iron in the sample), which is in the magnetically ordered structure. Mössbauer parameters show, that the most probable origin of this iron is γ-Fe_2O_3 with particle size of 10-15 nm, which is close to the crystallite size calculated from the XRD pattern.

Fig. 71. Mössbauer spectra of the powders before (1) and after (2) the H_2O_2 treatment.

After the H_2O_2 treatment, the color of the sample changed from deep black (sample 1) to reddish brown (sample 2), which is the typical color of γ-Fe_2O_3 (Fig. 72). The XRD pattern of sample 2 is very s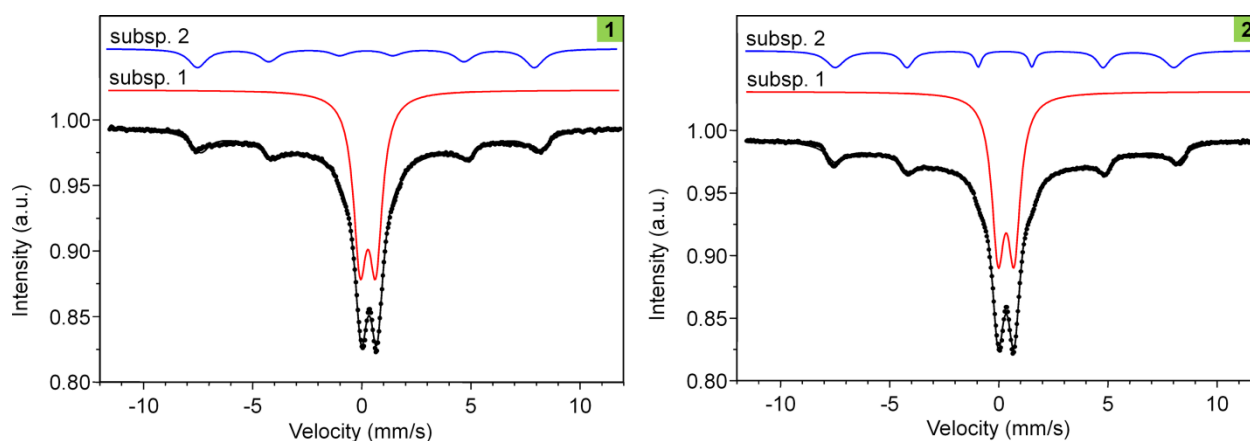imilar to that of sample 1, which suggests that the only crystalline phase present is maghemite, γ-Fe_2O_3 (Fig. 70). This statement is in agreement with the Mössbauer analysis of sample 2, which confirms the presence of Fe^{3+}. Actually, from the Mössbauer analysis point of view sample 2 (Fig. 66) is practically identical with sample 1 (Table 17).

Table 17. Mössbauer parameters of the samples before (1) and after (2) the H_2O_2 treatment.

Sample number		Isomer shift δ (mm/s)	Quadrupole splitting ΔE_Q (mm/s)	Hyperfine field B_{Hf} (T)	Relative area (%)
1	Subsp. 1	0.33	0.72	N/A	76
	Subsp. 2	0.34	- 0.02	47.9	24
2	Subsp. 1	0.33	0.73	N/A	75
	Subsp. 2	0.32	- 0.02	48.2	25

The average crystallite size of γ-Fe_2O_3 calculated from the diffraction pattern is 5 nm, which indicates that the H_2O_2 treatment does not cause any changes within the γ-Fe_2O_3 crystal structure nor crystallite size. The black color of sample 1 (Fig. 72) is due to the presence of residual carbon originating from the decomposition of glucose. The CNH elemental analysis revealed that sample 1 has a carbon content of 32.7 weight %. After the treatment with H_2O_2 the carbon content in sample 2 drops to 0.4 weight %, which demonstrates that the H_2O_2 treatment is a viable alternative for removing unwanted organic residues [32].

Unlike the tradition annealing procedure, which decreases significantly the specific surface area and promotes the γ-$Fe_2O_3 \rightarrow \alpha$-$Fe_2O_3$ phase transition, the carbon removal by H_2O_2 treatment does not alter the γ-Fe_2O_3 properties. On the contrary, it seems that the H_2O_2 treatment has a positive influence on γ-Fe_2O_3 properties – as will be shown later on. In addition to the removal of residual carbon, the H_2O_2 treatment also ensures the sterilization of γ-Fe_2O_3 particles, which is a key requirement in the field of biomedical applications.

The diffuse reflectance spectrum of sample 1 indicates that the sample absorbs electromagnetic radiation over the entire VIS range, which explains the black color of the sample induced by the presence of residual carbon (Fig. 72). The diffuse reflectance spectrum of sample 2, which is carbon free maghemite, (Fig. 72) shows a large and strong absorption band in the range of 360-550 nm, in accordance with the literature data [272,273]. This band is considered to

be the envelope of three absorption bands which can be assigned to the following transitions: $^6A_1 \rightarrow ^4E(^4D)$ for the band near 360-380 nm, $^6A_1 \rightarrow ^4E$, $^4A_1(^4G)$ for the band located at 430 nm and $2^6A_1 \rightarrow 2^4T_1(^4G)$ for the band near 480-550 nm [274,275].
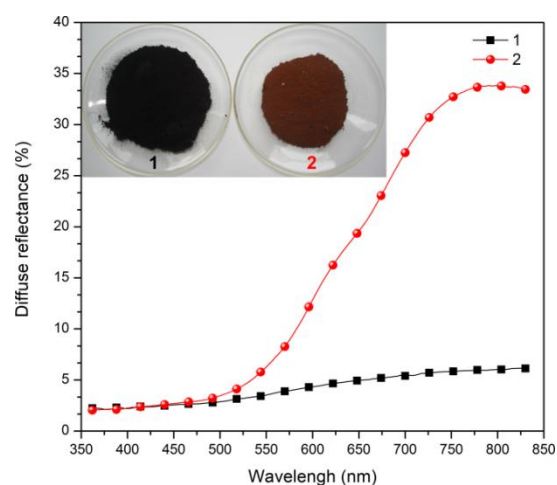
Fig. 72. Diffuse reflectance spectra of the two powders. Inset: images of the samples before (1) and after the H_2O_2 treatment (2).
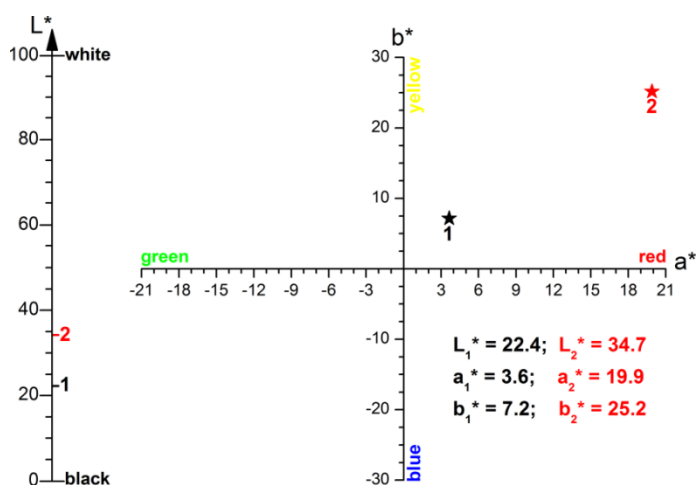
Fig. 73. Position of the two samples in the CIEL*a*b* color space.

In addition, sample 2 shows a sharp increase of the reflectance in the range of 550-750 nm, typical for γ-Fe_2O_3 powders with a reddish brown color. The CIEL*a*b* parameters confirm the visual observations concerning the color change from black (sample 1) to reddish brown (sample 2) as a consequence of carbon removal (Fig. 73). One may also notice that the sample treated with H_2O_2 (sample 2) has a higher proportion of red (a *) and a higher brightness (L *) than the sample resulted from the combustion process (sample 1). Thermal analyses of samples 1 and 2 (Fig. 74) confirm the positive action of H_2O_2 in terms of carbon removal. Up to 200 °C both samples exhibit a mass loss of ≈ 3 % that can be ascribed to the removal of adsorbed moisture. Between 200-700 °C sample 1 shows a wide exothermic effect on the DTA curve, with a maximum at 309 °C. This effect is associated to a mass loss of 33.8 %, which is due to the thermal oxidation of residual carbon originating from the incomplete combustion of glucose.
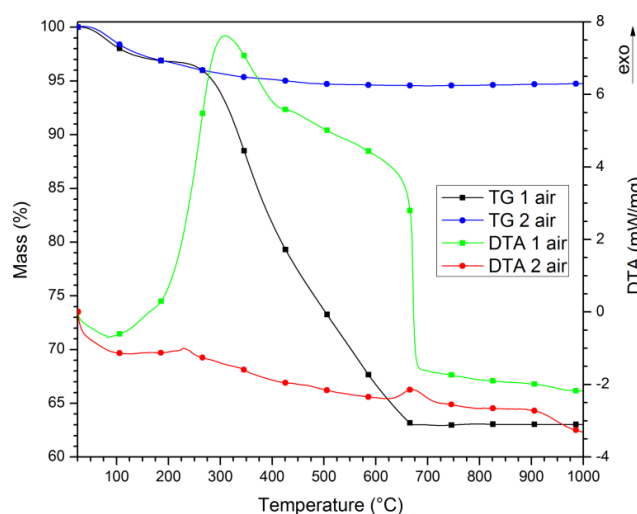
Fig. 74. TG-DTA curves of the powders, before (1) and after (2) the H_2O_2 treatment.
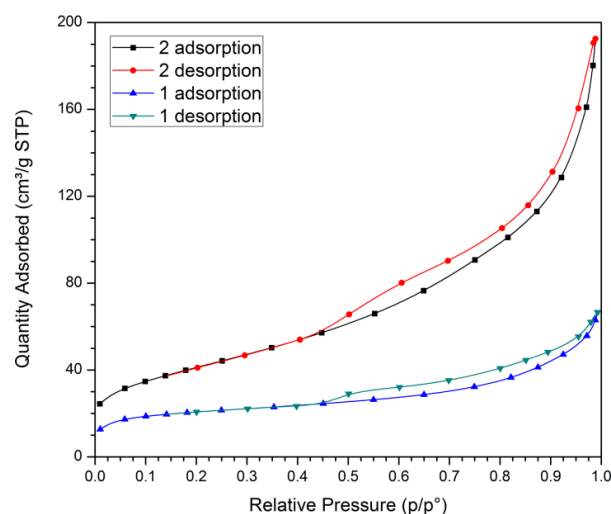
Fig. 75. Adsorption-desorption isotherms before (1) and after (2) the H_2O_2 treatment.

One can notice that this mass loss is very close to the carbon content of the sample (32.7 %), determined by CNH elemental analysis. Above 200 °C, the sample treated with H_2O_2 (sample 2) exhibits a negligible mass loss, which is in excellent agreement with the insignificant amount of carbon (0.4 %) determined by CNH elemental analysis. This behavior is another confirmation that the H_2O_2 treatment is a very effective procedure for carbon removal. The DTA curve of sample 2 shows an exothermic effect at 669 °C that is not accompanied by mass variation. Based on the literature data [262], this effect corresponds to γ-$Fe_2O_3 \rightarrow \alpha$-$Fe_2O_3$ transformation. Both samples exhibit type II isotherms with H3 hysteresis (Fig. 75).

BET surface area of sample 1 is 72.6 m^2/g (Table 18). However, 41 % of the BET surface area is the contribution of micropore area (29.8 m^2/g) and 59 % is the contribution of the external surface area (42.8 m^2/g). The high percentage of micropore area may be associated with the presence of residual carbon, which is a well-known microporous material. As a matter of fact, sample 1 has a micropore volume of $132.4 \cdot 10^{-4}$ cm^3/g. After the residual carbon was removed by H_2O_2 treatment (sample 2) the micropore volume decreased to $9.7 \cdot 10^{-4}$ cm^3/g whilst the BET surface area increased dramatically to 149.0 m^2/g (Table 18).

Table 18. Characteristics of γ-Fe_2O_3 powders, before (1) and after (2) the treatment with H_2O_2.

No.	BET surface area (m^2/g)	Micropore area (m^2/g)	External surface area (m^2/g)	Pore volume $\cdot 10^2$ (cm^3/g)	Micropore volume $\cdot 10^4$ (cm^3/g)
1.	72.6	29.8	42.8	8.1	132.4
2.	149.0	5.5	143.5	30.6	9.7

Moreover, in this case the micropore area has a contribution of just 3.7 % (5.5 m^2/g) to the BET surface area while the external surface area has a contribution of 96.3 % (144.5 m^2/g). The increase of the BET surface area of the sample treated with H_2O_2 is closely related to the removal of residual carbon. As the carbon impurities are eliminated, new pores are created, so that the pore volume increases from $8.1 \cdot 10^{-2}$ cm^3/g (sample 1) to $30.6 \cdot 10^{-2}$ cm^3/g (sample 2) (Table 18). With respect to other synthesis methods [247,252,259-261,263,265,269], one may notice that the BET surface area of γ-Fe_2O_3 nanoparticles prepared by solution combustion synthesis [29], followed by the H_2O_2 treatment, is among the largest reported values (Table 19).

Table 19. The BET surface area of γ-Fe_2O_3 powders prepared by various methods.

Reference no.	Synthesis method	BET surface area (m^2/g)
This study [29]	combustion synthesis	149.0
[269]	combustion synthesis	120
[247]	coprecipitation	31
[252]	co-precipitation	30.7
[260]	coprecipitation	73.8
[261]	coprecipitation	81.6
[265]	flame spray pyrolysis	102.8
[263]	thermal decomposition	119.0
[259]	coprecipitation	168.7

SEM images of samples 1 and 2 indicate that the H_2O_2 treatment does not promote any significant changes in terms of particle size and morphology (Fig. 76). In both samples, but

especially in the case of sample 2, clusters of individual γ-Fe_2O_3 round shaped particles can be observed. The size of these particles estimated from SEM images is $\approx$ 12 nm, which is quite close to the particle size estimated from Mössbauer parameters (Table 17).
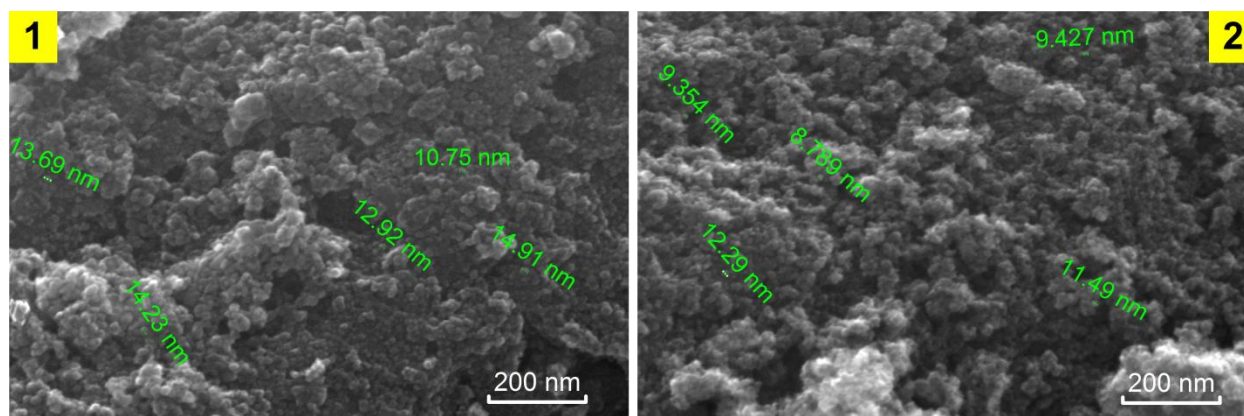
Fig. 76. SEM images of the two powders, before (1) and after (2) the H_2O_2 treatment.

Magnetic hysteresis loops recorded at room temperature are shown in Fig. 77. Remanent magnetization (M_R) and coercivity (H_C) of both samples are very close to 0, suggesting that the two powders are superparamagnetic. The superparamagnetic character of samples 1 and 2 is consistent with the small particle size and the Mössbauer measurements, which confirmed the presence of Fe^{3+} into the γ-Fe_2O_3 superparamagnetic structure (Fig. 71).
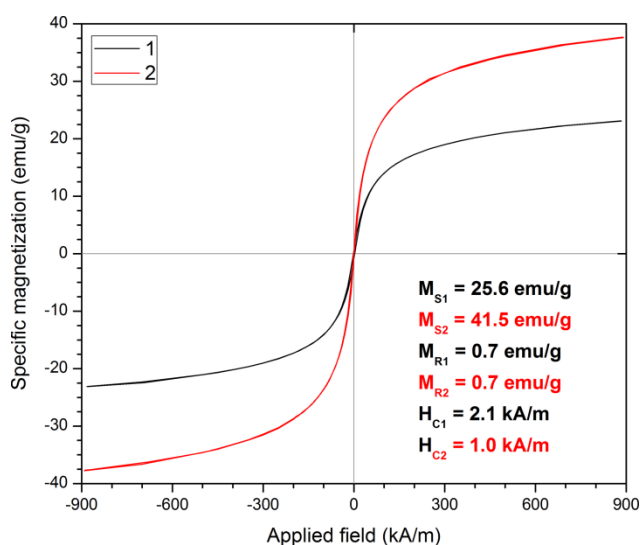
Fig. 77. Magnetic hysteresis loops before (1) and after (2) the H_2O_2 treatment.
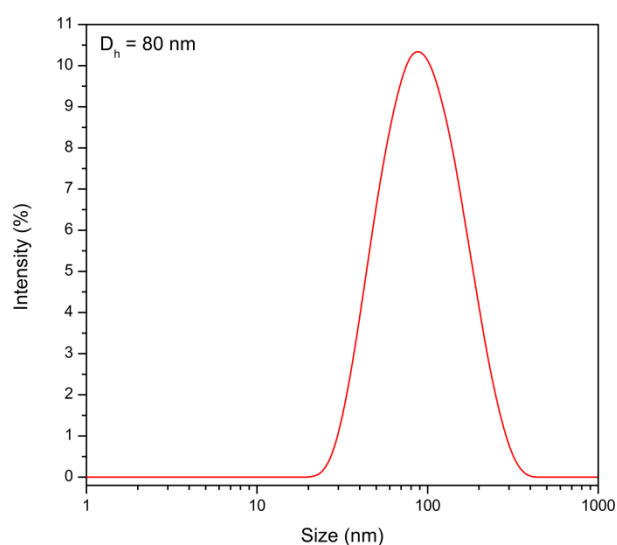
Fig. 78. The intensity distribution of particle size of the saline solution based colloidal suspension of γ-Fe_2O_3 nanoparticles.

At the same time, magnetic hysteresis loops indicate that none of the samples reach the saturation magnetization. Consequently, the saturation magnetization (M_S) was computed by plotting M versus 1/H, followed by the extrapolation of the magnetic curve at the magnitude of M when $1/H \rightarrow 0$. After the residual carbon was removed by H_2O_2 oxidation, the saturation magnetization increased from 25.6 emu/g to 41.5 emu/g. Due to the very small particle size the saturation magnetization of sample 2 is lower than the one of bulk γ-Fe_2O_3 [246,276].

After applying a double layer of oleic acid, γ-Fe$_2$O$_3$ nanoparticles treated with H$_2$O$_2$ (sample 2) have been easily dispersed in saline solution, leading to a stable colloidal suspension. At 25 °C, the dynamic laser scattering analysis revealed that the colloidal suspension has a single population of γ-Fe$_2$O$_3$ particles (Fig. 78). The intensity distribution of the particle size suggests that the γ-Fe$_2$O$_3$ nanoparticles covered with a double layer of oleic acid have a hydrodynamic diameter of 80 nm. The SEM image recorded on a dried droplet of colloidal suspension shows individual non-aggregated γ-Fe$_2$O$_3$ nanoparticles having a spherical shape (Fig. 79).
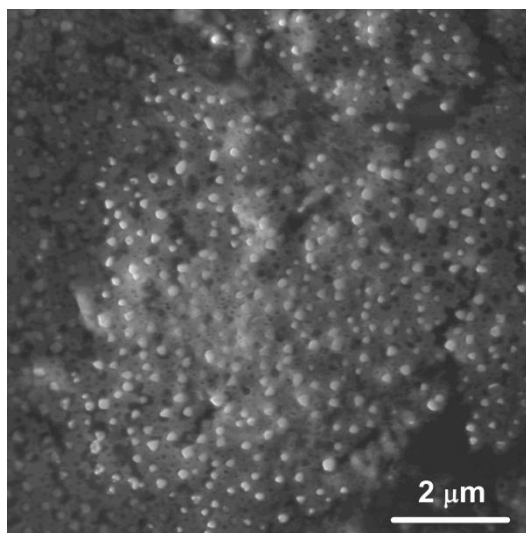
Fig. 79. SEM image of γ-Fe$_2$O$_3$ nanoparticles coated with a double layer of oleic acid.

Key findings

✓ The smoldering combustion reaction between iron nitrate and glucose generates a black powder containing γ-Fe$_2$O$_3$ and residual carbon.

✓ The H$_2$O$_2$ treatment of this powder leads to carbon removal by chemical oxidation: the carbon content decreases from 32.7 % to 0.4 % and the color of the sample changes from black to reddish brown.

✓ After the carbon removal by H$_2$O$_2$ treatment, the BET surface area of γ-Fe$_2$O$_3$ increases dramatically from 72.6 m^2/g to 149.0 m^2/g.

✓ SEM analysis revealed that the resulted γ-Fe$_2$O$_3$ particles have a round shape and an average size of 12 nm. γ-Fe$_2$O$_3$ crystallite size calculated from XRD patterns was 5 nm. The resulted γ-Fe$_2$O$_3$ nanoparticles exhibit a superparamagnetic behavior and a saturation magnetization of 41.5 emu/g.

✓ In addition to the removal of residual carbon, the H$_2$O$_2$ treatment also ensures the sterilization of γ-Fe$_2$O$_3$ particles, which is a key requirement in the field of biomedical applications.

✓ γ-Fe$_2$O$_3$ particles coated with a double layer of oleic acid were dispersed in saline solution, leading to a stable colloidal suspension of non-aggregated nanoparticles. DLS measurements indicated a unimodal distribution of γ-Fe$_2$O$_3$ nanoparticles and a hydrodynamic diameter of 80 nm.

2.2. Carrier evolution and development plan

The development of a successful professional carrier in the academic field mainly depends on the performances achieved by the candidate on two major plans, namely the *scientific research plan* and the *teaching plan*. Consequently, the candidate for a teaching position at the university must have the intrinsic ability to combine the research skills (the ability to come up with original ideas and solutions, creativity, thoroughness, convincing presentation of results etc.) with the teaching skills (pedagogic tact, the ability to make him-self understood, professionalism). Considering the rhythm of ISI articles publishing and the evolution of the citation number, the short-term objective in my carrier is to obtain the title of professor.

In the framework of the scientific research plan, the enhancement of the research activity is a top priority, in agreement with the status of Politehnica University of Timisoara, which is a university focused on advanced research and education. From this point of view, attracting new funds required for conducting research activities will be one of the most important directions. Therefore I intent to submit several funding applications within the upcoming national (PN III) and international (Horizon 2020) call for proposals.

For instance, on December 2014 I submitted a project proposal (*Combustion synthesis of smart near-infrared reflective nanopigments for heat reflective (cool) coatings*, project registration code PN-II-RU-TE-2014-4-1587) within the Research Projects for Young Research Teams RU-TE-2014 competition.

The experience gained as a principal investigator (see the CV) or member of the implementation team indicate that I am able to elaborate successful project applications, starting from an original idea, rigorously planned objectives, plausible results, a competent and competitive team, risk management and appropriate dimensioning of the budget. In order to increase the success rate of a project application the key idea must be properly crystallized and the elaboration of the project proposals should be made in advance.

The following section briefly describes some of my future research directions:

- *Combustion synthesis of oxide (nano)powders with magnetic properties (magnetite, maghemite, ferrites).* Currently there is a great number of papers reporting the properties and the potential uses of these materials in biomedical applications (cancer therapy, hypothermia treatment, targeted drug delivery, NMR contrast agents etc.) but also in the technical field (automotive and building suspensions, magnetic inks and paper). In most of these papers, the magnetic (nano)powders are obtained by co-precipitation, so that the preparation of these materials by combustion synthesis is a less explored subject. From this point of view it will be interesting to investigate the influence of various factors (e.g. fuel type, fuel proportion, working atmosphere) on the properties of the resulting powder. Moreover, an important aspect that should be studied concerns the behavior of the combustion-synthesized materials in various biological media (biocompatibility). Secondly, it would be interesting to look at the use of these (nano)powders as adsorbent materials. The possibility of developing new composite materials (which would combine magnetic properties, adsorbent capacity and antimicrobial properties), for waste water treatment applications will be also considered.

- *Combustion synthesis of long afterglow phosphor materials (several hours)* is one of the top priorities, since many useful applications (road signs and markings, micro crack/microdefect revealing, decorative paints and coatings, enamels and glazes, etc.) rely on oxide materials which exhibit long phosphorescence, such as lanthanide-doped alkaline-earth metal aluminates. Generally, the luminescent properties are highly depending on the crystallite size, which means

that for the same chemical composition, the emission duration (afterglow) is longer in the case of larger crystallites. Given the remarkable advantages of the combustion synthesis (high temperature developed during the combustion reaction, energy efficiency, high reaction rate, possibility to control the reaction atmosphere), this method would be very adequate for the preparation of such materials. In addition, the concept of using fuel mixtures could be extremely useful in the preparation of such phosphor materials, because would facilitate the formation of the desired phase directly from the combustion process without any further heat treatment.

- *Combustion synthesis of apatite and hydroxyapatite*. Currently apatite and hydroxyapatite are commonly used materials for bone implants (facial reconstruction, prosthetic eye). Due to the large volume of gases released during the combustion reaction, the combustion-synthesized powders present a particular morphology, which is characterized by the presence of many interconnected pores, which resembles to a sponge or a coral. Such a morphology, which is preserved to a certain extent after sintering, is very beneficial and desirable for apatite or hydroxyapatite implants, as it facilitates the vascularization. In addition, this type of microarchitecture, consisting of interconnected pores, promotes cell growth contributing to the implant osseointegration and acceptance.

Currently, the existing research infrastructure at Politehnica University of Timisoara allows the implementation of these research topics. However, the interdisciplinary nature of the research areas mentioned above requires the development of a network which must include specialists in other fields. For example, in the case of phosphor materials, their luminescent properties will be measured in collaboration with the Romanian Academy – Timisoara branch, and their effective testing can be done at Azur company. In the case of biomedical applications, the collaboration with other specialists from the faculties of medicine from Arad (Vasile Goldis Western University of Arad, The Faculty of Medicine, Pharmacy and Dental Medicine) and Timisoara (Victor Babes University of Medicine and Pharmacy) is envisaged. Within the same framework of cooperation, in addition to the local collaboration it is necessary to develop collaborative relationships with other experts from abroad, mainly European Union countries (Hungary, France, Italy etc.). One way of achieving this goal is to attend some of the most renowned international conferences in the field: ECerS, E-MRS, CIMTEC etc. The development of collaborative relationships with partners from the European Union is mainly intended to build a competitive international team with real chances of success in the future international competitions. Regarding the publishing rate as well the quality of journals selected for results dissemination the self-imposed standard is to publish on average annually at least 3 articles in ISI-ranked journals, with an impact factor higher than 2.

As far as the teaching plan is concerned, one of the major objectives is to update the content of the courses (E.g. Composite materials), according to the labor market demands and the latest results reported in the literature. In order to increase the efficiency of course teaching, a special attention will be paid to the laboratory activity, which will consist of individual and team practical works. These practical works to be carried out during the laboratory activities will be selected based on the fact that they should be equally relevant, interesting, attractive, but also designed to open the students' appetite for these subjects. For example, at the Composite Materials laboratory students will have the opportunity to design, obtain, characterize and test two different types of composite materials, namely: corundum / spinel ceramic matrix composites (having excellent mechanical properties) and magnetite / carbon composites (having outstanding adsorbent properties).

In order to facilitate but also to improve the teacher-student communication a greater importance should be paid to the use of modern digital teaching techniques. Since "*a picture is worth a thousand words*", the interactive presentation of the courses will be accompanied by suggestive images and schemes. Similarly, students are encouraged to discuss during the laboratory activity their experimental results and to defend their point of view. Course notes and practical work reports will be posted on the faculty website (www.chim.upt.ro).

As a future PhD supervisor I intend to continue the investigations on the potential of combustion synthesis in the preparation of metal oxide (nano)particles. Currently, the available BSc and MSc research topics (Ex.: combustion synthesis of magnetic nanopowders, combustion synthesis of magnetite / carbon composites, preparation of phosphor materials based on rare-earth doped alkaline-earth aluminates via combustion synthesis, smart thermoreflective nanopigments prepared by combustion synthesis) have a high potential to generate results that can be reported by publication in ISI journals with high impact factor.

2.3. References

[1]   K.C. Patil, M.S. Hegde, T. Rattan, S.T. Aruna, Chemistry of Nanocrystalline Oxide Materials. Combustion Synyhesis, Properties and Applications. World Scientific, 2008.

[2]   S. Ekambaram, K.C. Patil, M. Maaza, Synthesis of lamp phosphors: facile combustion approach. J. Alloys Compd. 393 (2005) 81–92.

[3]   J.J. Kingsley, K.C. Patil, A novel combustion process for the synthesis of fine particle α-alumina and related oxide materials, Mater. Lett. 6 427–432 (1988).

[4]   S.T. Aruna, A.S. Mukasyan, Combustion synthesis and nanomaterials. Curr. Opin. Solid St. M. 12 (2008) 44–50.

[5]   K.C. Patil, S.T. Aruna, T. Mimani, Combustion synthesis: an update. Curr. Opin. Solid St. M. 6 (2002) 507–512.

[6]   K.C. Patil, S.T. Aruna, S. Ekambaram, Combustion synthesis. Curr. Opin. Solid St. M. 2 (1997) 158–165.

[7]   **R. Ianoş**, I. Lazău, C. Păcurariu, P. Barvinschi, Peculiarities of $CaO \cdot 6Al_2O_3$ formation by using low-temperature combustion synthesis. Eur. J. Inorg. Chem. 6 (2008) 925–930.

[8]   **R. Ianoş**, P. Barvinschi, Characterization of $Mg_{1-x}Ni_xAl_2O_4$ solid solutions prepared by combustion synthesis. J. Eur. Ceram. Soc. 31 (2011) 739–743.

[9]   **R. Ianoş**, R. Lazău, P. Barvinschi, Synthesis of $Mg_{1-x}Co_xAl_2O_4$ blue pigments via combustion route. Adv. Powder Technol. 22 (2011) 396–400.

[10]   **R. Ianoş**, I. Lazău, C. Păcurariu, Metal nitrate/fuel mixture reactivity and its influence on the solution combustion synthesis of γ-$LiAlO_2$. J. Therm Anal. Calorim. 97 (2009) 209–214.

[11]   **R. Ianoş**, I. Lazău, C. Păcurariu, The influence of combustion synthesis conditions on the α-Al_2O_3 powder preparation. J. Mater. Sci. 44 (2009) 1016–1023.

[12]   **R. Ianoş**, I. Lazău, C. Păcurariu, Solution combustion synthesis of α-cordierite. J. Alloys Compd. 480 (2009) 702–705.

[13]   **R. Ianoş**, R. Lazău, Combustion synthesis, characterization and sintering behavior of magnesium aluminate ($MgAl_2O_4$) powders. Mater. Chem. Phys. 115 (2009) 645–648.

[14]   **R. Ianoş**, I. Lazău, C. Păcurariu, P. Barvinschi, Fuel mixture approach for solution combustion synthesis of $Ca_3Al_2O_6$ powders. Cem. Concr. Res. 39 (2009) 566–572.

[15]   **R. Ianoş**, I. Lazău, C. Păcurariu, P. Barvinschi, Solution combustion synthesis of $MgAl_2O_4$ using fuel mixtures. Mater. Res. Bull. 43 (2008) 3408–3415.

[16]   **R. Ianoş**, C. Păcurariu, I. Lazău, S. Ianoşev, Z. Ecsedi, R. Lazău, P. Barvinschi, Comparative study regarding the formation of $La_{1-x}Sr_xCrO_3$ perovskite using unconventional synthesis methods, J. Therm. Anal. Calorim. 94 (2008) 343–348.

[17]   **R. Ianoş**, An efficient solution for the single-step synthesis of $4CaO \cdot Al_2O_3 \cdot Fe_2O_3$ powders. J. Mater. Res. 24 (2009) 245–252.

[18]   I. Lazău, M. Suba, C. Păcurariu, **R. Ianoş**, R. Băbuță, Combustion Synthesis of $Ca_2(Fe_{1-x}Al_x)_2O_5$ Solid Solutions. Rom. J. Mater. 39 (2009) 315–325.

[19]   **R. Ianoş**, R. Băbuță, R. Lazău, Characteristics of Y_2O_3 powders prepared by solution combustion synthesis in the light of a new thermodynamic approach. Ceram. Int. 40 (2014) 12207–12211.

[20]   **R. Ianoş**, I. Lazău, C. Păcurariu, P. Barvinschi, Application of new organic fuels in the direct $MgAl_2O_4$ combustion synthesis. Eur. J. Inorg. Chem. 6 (2008) 931–938.

[21]   I. Lazău, C. Păcurariu, **R. Ianoş**, Z. Ecsedi, S. Ianoşev, Particular aspects of oxide powders synthesis using unconventional methods. Rom. J. Mater. 37 (2007) 185–197.

[22]   I. Lazău, C. Păcurariu, Z. Ecsedi, **R. Ianoş**, Peculiarities of ceramic powders synthesis using the combustion method. Rev. Roum. Chim. 50 (2005) 919–927.

[23]   **R Ianoş**, R Lazău, S Borcănescu, R Băbuţă, Single-step combustion synthesis of $LaAlO_3$ powders and their sintering behavior. Ceram. Int. 40 (2014) 7561–7565.

[24]   **R. Ianoş**, R. Lazău, R.C. Boruntea, Solution combustion synthesis of bluish-green $BaAl_2O_4$: Eu^{2+}, Dy^{3+} phosphors. Ceram. Int. 41 (2015) 3186–3190.

[25]   **R. Ianoş**, P. Barvinschi, Solution combustion synthesis of calcium zirconate, $CaZrO_3$, powders. J. Solid State Chem. 183 (2010) 491–496.

[26]   **R. Ianoş**, S. Borcănescu, R. Lazău, Large surface area $ZnAl_2O_4$ powders prepared by a modified combustion technique. Chem. Eng. J. 240 (2014) 260–263.

[27]   **R. Ianoş**, A. Tăculescu, C. Păcurariu, I. Lazău, Solution combustion synthesis and characterization of magnetite, Fe_3O_4, nanopowders. J. Amer. Ceram. Soc. 95 (2012) 2236–2240.

[28]   **R. Ianoş**, C. Păcurariu, G. Mihoc, Magnetite/carbon nanocomposites prepared by an innovative combustion synthesis technique – Excellent adsorbent materials. Ceram. Int. 40 (2014) 13649-13657.

[29]   **R. Ianoş**, E.A. Tăculescu (Moacă), C. Păcurariu, D. Niznansky, γ-Fe_2O_3 nanoparticles prepared by combustion synthesis, followed by chemical oxidation of residual carbon with H_2O_2. Mater. Chem. Phys. 148 (2014) 705–711.

[30]   **R. Ianoş**, M. Bosca, R. Lazău, Fine tuning of $CoFe_2O_4$ properties prepared by solution combustion synthesis. Ceram. Int. 40 (2014) 10223–10229.

[31]   **R. Ianoş,** Highly sinterable cobalt ferrite particles prepared by a modified solution combustion synthesis. Mater. Lett. 135 (2014) 24–26.

[32]   **R. Ianoş**, R. Lazău, I. Lazău, C. Păcurariu, Chemical oxidation of residual carbon from $ZnAl_2O_4$ powders prepared by combustion synthesis. J. Eur. Ceram. Soc. 32 (2012) 1605–1611.

[33]   E. Taspinar, A.C. Tas, Low-Temperature Chemical Synthesis of Lanthanum Monoaluminate, J. Amer. Ceram. Soc. 80 (1997) 133–141.

[34]   M.V. Cabañas, C.V. Ragel, F. Conde, J.M. Gonzáleaz-Calbet, M. Vallet-Regí, $LaAlO_3$ thin films deposited on Si(100) and MgO(100) substrates, Solid State Ionics101-103 (1997) 191–195.

[35]   S.-K. Hong, J.-G. Kim, H.-J. Kim, H.-W. Cho, S.-K. Yu, J.-H. Ahn, J.-H. Joo, G.-W. Hong, H.-G. Lee, Preparation of high Jc YBCO films on LAO by spray pyrolysis process using nitrate precursors, Physica C 463-465 (2007) 536–539.

[36]   J.Y. Park, G.M. Choi, Electrical conductivity of Sr and Mg doped $LaAlO_3$, Solid State Ionics154-155 (2002) 535–540.

[37]   D. Hreniak, W. Strek, P. Deren, A. Bednarkiewicz, A. Lukowiak, Synthesis and luminescence properties of Eu^{3+}-doped $LaAlO_3$ nanocrystals, J. Alloys Compd. 408-412 (2006) 828–830.

[38]   P.J. Deren, R. Mahiou, Spectroscopic characterization of $LaAlO_3$ crystal doped with Er^{3+} ions, Opt. Mat. 29 (2007) 766–772.

[39]   S.N. Koc, F. Oksuzoemer, E. Yasar, S. Akturk, M.A. Gurkaynak, Effect of sol-gel modifications on formation and morphology of nanocrystalline lanthanum aluminate, Mater. Res. Bull. 41 (2006) 2291–2297.

[40]   D. Lybye, F.W. Poulsen, M. Mogensen, Conductivity of A- and B-site doped $LaAlO_3$, $LaGaO_3$, $LaScO_3$ and $LaInO_3$ perovskites, Solid State Ionics128 (2000) 91–103.

[41]   S.K. Behera, P.K. Sahu, S.K. Pratihar, S. Bhattacharyya, Low temperature synthesis of spherical lanthanum aluminate nanoparticles, Mater. Lett. 58 (2004) 3710–3715.

[42]   R. Spinicci, P. Marini, S. De Rossi, M. Faticanti, P. Porta, Oxidative coupling of methane on $LaAlO_3$ perovskites partially substituted with alkali or alkali-earth ions, J. Molec. Catal. A Chem. 176 (2001) 253–265.

[43]   M. Kakihana, T. Okubo, Low temperature powder synthesis of $LaAlO_3$ through in situ polymerization route utilizing citric acid and ethylene glycol, J. Alloys Compd. 266 (1998) 129–133.

[44]   N.E. Bogdanchikova, S. Fuentes, M. Avalos-Borja, M.H. Farías, A. Boronin, G. Díaz, Structural properties of Pd catalysts supported on Al_2O_3-La_2O_3 prepared by sol-gel method, Appl. Catal. B Environ. 17 (1998) 221–231.

[45]   M. Chroma, J. Pinkas, I. Pakutinskiene, A. Beganskiene, A. Kareiva, Processing and characterization of sol-gel fabricated mixed metal aluminates, Ceram. Int. 31 (2005) 1123–1130.

[46]   F. Matteucci, M. Dondi, G. Cruciani, G. Baldi, A. Barzanti, Colouring Mechanism of Red Ceramic Pigments Based on Perovskite Structure, Key Eng. Mater. 264-268 (2004) 1549–1552.

[47]   C. Kuo, C. Wang, T. Chen, G. Chen, I. Hung, C. Shih, K. Fung, Low temperature synthesis of nanocrystalline lanthanum monoaluminate powders by chemical coprecipitation, J. Alloys Compd. 440 (2007) 367–374.

[48]   P.K. Sahu, S.K. Behera, S.K. Pratihar, S. Bhattacharyya, Low temperature synthesis of microwave dielectric $LaAlO_3$ nanoparticles: effect of chloride on phase evolution and morphology, Ceram. Int. 30 (2004) 1231–1235.

[49]   W. Li, M.W. Zhuo, J.L. Shi, Synthesizing nano $LaAlO_3$ powders via coprecipitation method, Mater. Lett. 58 (2004) 365–368.

[50]   Y. Xu, G. Huang, H. Long, Synthesis of lanthanum aluminate via the ethylenediaminetetraacetic acid gel route, Ceram. Int. 29 (2003) 837–840.

[51]   D. Zhou, G. Huang, X. Chen, J. Xu, S. Gong, Synthesis of $LaAlO_3$ via ethylenediaminetetraacetic acid precursor, Mater. Chem. Phys. 84 (2004) 33–36.

[52]   A.K. Adak, P. Pramanik, Synthesis and characterization of lanthanum aluminate powder at relatively low temperature, Mater. Lett. 30 (1997) 269–273.

[53]   Z. Li, S. Zhang, W.E. Lee, Molten salt synthesis of $LaAlO_3$ powder at low temperatures, J. Eur. Ceram. Soc. 27 (2007) 3201–3205.

[54]   Z. Tian, H. Yu, Z. Wang, Combustion synthesis and characterization of nanocrystalline $LaAlO_3$ powders, Mater. Chem. Phys. 106 (2007) 126–129.

[55]   A. Dhahri, K. Horchani-Naifer, F. Enrichi, M. Ferid, Combustion synthesis and photoluminescence of Eu^{3+} doped $LaAlO_3$ nanophosphor, Opt. Mater. 34 (2013) 1742–1746.

[56]   E.V. Galuskin, V.M. Gazeev, T. Armbruster, A.E. Zadov, I.O. Galuskina, N.N. Pertsev, P. Dzierżanowski, M. Kadiyski, A.G. Gyrbanov, R. Wrzalik, A. Winiarski, Lakargiite

CaZrO$_3$: A new mineral of the perovskite group from the North Caucasus, Kabardino-Balkaria, Russia. Am. Mineral. 93 (2008) 1903–1910.

[57]   G. Róg, M. Dudek, A. Kozlowska-Róg, M. Bućko, Calcium zirconate: preparation, properties and application to the solid oxide galvanic cells. Electrochim. Acta 47 (2002) 4523–4529.

[58]   N.L. Ross, T.D. Chaplin, Compressibility of CaZrO$_3$ perovskite: Comparison with Ca-oxide perovskites. J. Solid State Chem. 172 (2003) 123–126.

[59]   M. Pollet, S. Marinel, Copper electrodes multilayer ceramic capacitors. J. Mater. Sci. 39 (2004) 1943–1958.

[60]   M. Dudek, E. Drożdż-Cieśla, Some observations on synthesis and electrolytic properties of nonstoichiometric calcium zirconate. J. Alloy. Compd. 475 (2009) 846–854.

[61]   H. Zhang, X. Fu, S. Niu, Q. Xin, Blue luminescence of nanocrystalline CaZrO$_3$:Tm phosphors synthesized by a modified Pechini sol-gel method. J. Lumin. 128 (2008) 1348–1352.

[62]   **R. Ianoş**, R. Lazău, Chromium-doped calcium zirconate - A potential red shade pigment: Preparation, characterization and testing. Dyes and Pigments 105 (2014) 152–156.

[63]   C. Cano, M.I. Osendi, M. Belmonte, P. Mirazo, Effect of the type of flame on the microstructure of CaZrO$_3$ combustion flame sprayed coatings. Surf. Coat. Technol. 201 (2006) 3307–3313.

[64]   H. Wang, M. Wang, W. Zhang, N. Zhao, W. Wei, Y. Sun, Synthesis of dimethyl carbonate from propylene carbonate and methanol using CaO-ZrO$_2$ solid solutions as highly stable catalysis. Catal. Today 115 (2006) 107–110.

[65]   S.S.A. Azimov, D.D. Gulamova, S.K. Suleimanov, Production of calcium zirconate in a solar furnace. Refract. Ind. Ceram. 23 (1982) 42–43.

[66]   C.C. Wang, W.H. Chen, S.A. Akbar, High-temperature a.c. electrical behavior of polycrystalline calcium zirconate. J. Mater. Sci. 32 (1997) 2305–2312.

[67]   S.C. Hwang, G.M. Choi, The mixed ionic and electronic conductivity of CaZrO$_3$ with cation nonstoichiometry and oxygen partial pressure. Solid State Ionics 179 (2008) 1042–1045.

[68]   I.E. Gonenli, A.C. Tas, Chemical Synthesis of Pure and Gd-doped CaZrO$_3$ Powders. J. Eur. Ceram. Soc. 19 (1999) 2563–2567.

[69]   C.S. Prasanth, H.P. Kumar, R. Pazhani, S. Solomon, J.K. Thomas, Synthesis, characterization and microwave dielectric properties of nanocrystalline CaZrO$_3$ ceramics. J. Alloy. Compd. 464 (2008) 306–309.

[70]   T. Yu, C.H. Chen, X.F. Chen, W. Zhu, R.G. Krishnan, Fabrication and characterization of perovskite CaZrO$_3$ oxide thin films. Ceram. Int. 30 (2004) 1279–1282.

[71]   J.G. Speight in: Lange's Handbook of Chemistry, sixteenth ed., McGraw-Hill 2005.

[72]   B.S.B. Reddy, I. Mal, S. Tewari, K. Das, S. Das, Aqueous Combustion Synthesis and Characterization of Nanosized Tetragonal Zirconia Single Crystals. Metall. Mater. Trans. A 38A (2007) 1786–1793.

[73]   O. Knacke, O. Kubaschewski, K. Hesselmann, Thermochemical Properties of Inorganic Substances, 2nd ed. (Springer-Verlag 1991).

[74]   M.J. Zawadzki, J. Wrzyszcz, Hydrothermal synthesis of nanoporous zinc aluminate with high surface area. Mater. Res. Bull. 35 (2000) 109–114.

[75] A. Edelstein, R.C. Cammarata, Nanomaterials: Synthesis, Properties and Applications, Institute of Physics Publishing, Bristol and Philadelphia, 1996.

[76] N.J. Van der Laag, M.D. Snel, P.C.M.M. Magustin, G. With, Structural, elastic, thermophysical and dielectric properties of zinc aluminate ($ZnAl_2O_4$). J. Eur. Ceram. Soc. 24 (2004) 2417–2424.

[77] A.R. Phani, M. Passacantando, S. Santucci, Synthesis and characterization of zinc aluminum oxide thin films by sol-gel technique. Mater. Chem. Phys. 68 (2001) 66–71.

[78] A. Flura, F. Can, X. Courtois, S. Royer, D. Duprez, High-surface-area zinc aluminate supported silver catalysts for low-temperature SCR of NO with ethanol. Appl. Catal. B: Environmental 126 (2012) 275–289.

[79] H. Grabowska, W. Mista, J. Trawczynski, J. Wrzyszcz, M. Zawadzki, Thermal stability of platinum supported zinc aluminate combustion catalysts. Pol. J. Chem. 75 (2001) 1561–1568.

[80] L.M. Chen, X.M. Sun, Y.N. Liu, K.B. Zhou, Y.D. Li, Porous $ZnAl_2O_4$ synthesized by a modified citrate technique. J. Alloys Compd. 376 (2004) 257–261.

[81] C.O. Arean, B.S. Sintes, G.T. Palomino, C.M. Carbonell, P.E. Scalona, S.J.B. Parra, Preparation and characterization of spinel-type high-surface-area Al_2O_3-$ZnAl_2O_4$ mixed-metal oxides by an alkoxide route. Microporous Mater. 8 (1997) 187–192.

[82] Z.Z. Chen, E.W. Shi, Y.Q. Zheng, W.J. Li, B. Xiao, J.Y. Zhuang, L.A. Tang, Particle size control and dependence on precursor pH: synthesis uniform submicrometer zinc aluminate particles. J. Am. Ceram. Soc. 88 (2005) 127–133.

[83] Z. Chen, E. Shi, Y. Zheng, W. Li, N. Wu, W. Zhong, Synthesis of mono-dispersed $ZnAl_2O_4$ powders under hydrothermal conditions. Mater. Lett. 56 (2002) 601–605.

[84] M. Zawadzki, J. Wryzyszcz, Hydrothermal synthesis of nanoporous zinc aluminate with high surface area. Mater. Res. Bull. 35 (2000) 108–114.

[85] M. Zawadzki, Synthesis of nanosized and microporous zinc aluminate spinel by microwave assisted hydrothermal method (microwave hydrothermal synthesis of $ZnAl_2O_4$). Solid State Sci. 8 (2006) 14–18.

[86] M.A. Valenzuela, P. Bosch, G. Aguilar-rios, A. Montoya, I. Schifter, Comparison between sol–gel, coprecipitation and wet mixing synthesis of $ZnAl_2O_4$. J. Sol–Gel Sci. Technol. 8 (1997) 107–110.

[87] S. Mathr, M. Veith, M.H. Haoshen, N. Lecerj, V. Huch, Single source sol-gel synthesis of nanocrystalline $ZnAl_2O_4$: structural and optical properties. J. Am. Ceram. Soc. 84 (2001) 1921–1928.

[88] X. Wei, D. Chen, Synthesis and characterization of nanosized zinc aluminate spinel by sol–gel technique. Mater. Lett. 60 (2006) 823–827.

[89] C.T. Alves, A. Oliveira, S.A.V. Carneiro, A.G. Silva, H.M.C. Andrade, S.A.B. Vieira de Melo, E.A. Torres, Transesterification of waste frying oil using a zinc aluminate catalyst. Fuel Process. Technol. 106 (2013) 102–107.

[90] D. Dhak, P. Pramanik, Particle size comparison of soft-chemically prepared transition metal (Co, Ni, Cu, Zn) aluminate spinels. J. Am. Ceram. Soc. 89 (2006) 1014–1021.

[91] M.A. Valenzuela, J.P. Jacobs, P. Bosch, S. Reijne, B. Zapata, H.H. Brongersma, The influence of the preparation method on the surface structure of $ZnAl_2O_4$. Appl. Catal. A Gen. 148 (1997) 315–324.

[92]   C.C. Hwang, T.Y. Wu, Combustion synthesis of nanocrystalline ZnO powders using zinc nitrate and glycine as reactants—influence of reactant composition. J. Mater. Sci. 39 (2004) 6111–6115.

[93]   **R. Ianoş**, I. Lazău, C. Păcurariu, P. Sfîrloagă, Aqueous combustion synthesis and characterization of ZnO powders. Mater. Chem. Phys. 129 (2011) 881–886.

[94]   K.S.W. Sing, D.H. Everett, R.A.W. Haul, L. Moscou, R.A. Pierotti, J. Rouquérol, T. Siemieniewska, Reporting physysorption data for gas/solid systems with specials reference to the determination of surface area and porosity. Pure & App. Chem. 57 (1985) 603–619.

[95]   S. Farhadi, S. Panahandehjoo, Spinel-type zinc aluminate ($ZnAl_2O_4$) nanoparticles prepared by the co-precipitation method: A novel, green and recyclable heterogeneous catalyst for the acetylation of amines, alcohols and phenols under solvent-free conditions. Appl. Catal. A Gen. 382 (2010) 293–302.

[96]   Y. Xingbin, C. Jiangtao, X. Qunji, M. Philippe, Synthesis and magnetic properties of $CoFe_2O_4$ nanoparticles confined within mesoporous silica. Micropor. Mesopor. Mat. 135 (2010) 137–142.

[97]   W. Jing, D. Tong, L. Yulong, Y. Caiqin, Z. Wenhong, Synthesis and characterization of $CoFe_2O_4$ magnetic particles prepared by co-precipitation method: Effect of mixture procedures of initial solution. J. Alloys Compd. 450 (2008) 532–539.

[98]   L. Xing-Hua, X. Cai-Ling, H. Xiang-Hua, Q. Liang, W. Tao, L. Fa-Shen, Synthesis and Magnetic Properties of Nearly Monodisperse $CoFe_2O_4$ Nanoparticles Through a Simple Hydrothermal Condition. Nanoscale. Res. Lett. 5 (2010) 1039–1044.

[99]   Z. Shusen, M. Dongxu, Preparation of $CoFe_2O_4$ Nanocrystallites by Solvothermal Process and Its Catalytic Activity on the Thermal Decomposition of Ammonium Perchlorate. J. Nanomater. (2010) article ID 842816:1–5.

[100] K. Nermin, B. Abdülhadi, K. Yüksel, S.T. Muhammet, Microwave-assisted combustion synthesis of $CoFe_2O_4$ with urea, and its magnetic characterization. Scr. Mater. 57 (2007) 441–444.

[101] A.B. Salunkhe, V.M. Khot, N.D. Thorat, M.R. Phadatare, C.I. Satish, D.S. Dhawale, S.H. Pawar, Polyvinil alcohol functionalized cobalt ferrite nanoparticles for biomedical applications. Appl. Surf. Sci. 264 (2013) 598–604.

[102] L. Chao, A.J. Rondinone, Z.J. Zhang, Synthesis of magnetic spinel ferrite $CoFe_2O_4$ nanoparticles from ferric salt and characterization of the size-dependent superparamagnetic properties. Pure Appl. Chem. 72 (2000) 37–45.

[103] J. Unyong, T. Xiaowei, W. Yong, Y. Hong, X. Younan, Superparamagnetic Colloids: Controlled Synthesis and Niche Applications. Adv. Mater. 19 (2007) 33–60.

[104] V.L. Calero-DdelC, C. Rinaldi, Synthesis and magnetic characterization of cobalt-substituted ferrite ($Co_xFe_{3-x}O_4$) nanoparticles. J. Magn. Magn. Mater. 314 (2007) 60–67.

[105] S.H. Xiao, W.F. Jiang, L.Y. Li, X. Li, Low-temperature auto-combustion synthesis and magnetic properties of cobalt ferrite nanopowder. Mater. Chem. Phys. 106 (2007) 82–87.

[106] S.Y. Zhao, D.K. Lee, C.W. Kim, H.G. Cha, Y.H. Kim, Y.S. Kang, Synthesis of Magnetic Nanoparticles of Fe_3O_4 and $CoFe_2O_4$ and Their Surface Modification by Surfactant Adsorption. Bull. Korean Chem. Soc. 27 (2006) 237–242.

[107] P. Pulišová, J. Kováč, A. Voigt, P. Raschman, Structure and magnetic properties of Co and Ni nano-ferrites prepared by a two step direct microemulsions synthesis. J. Magn. Magn. Mater. 341 (2013) 93–99.

[108] C. Chifiriuc, V. Lazăr, C. Bleotu, I. Călugărescu, A.M. Grumezescu, D.E. Mihăiescu, D.E. Mogoşanu, A.S. Buteică, E. Buteică, Bacterial Adherence to the Cellular and Inert Substrate in the Precense of $CoFe_2O_4$ and Fe_3O_4 /Oleic Acid – Core/Shell. Dig. J. Nanomater. Bios. 6 (2011) 37–42.

[109] K.V.P.M. Shafi, A. Gedanken, Sonochemical Preparation and Size-Dependent Properties of Nanostructured $CoFe_2O_4$ Particles. Chem. Mater. 10 (1998) 3445–3450.

[110] T. Meron, Y. Rosenberg, Y. Lereah, G. Markovich, Synthesis and assembly of high-quality cobalt ferrite nanocrystals prepared by a modified sol–gel technique. J. Magn. Magn. Mater. 292 (2005) 11–16.

[111] R.N. Panda, J.C. Shih, T.S. Chin, Magnetic properties of nano-crystalline Gd- or Pr-substituted $CoFe_2O_4$ synthesized by the citrate precursor technique. J. Magn. Magn. Mater. 257 (2003) 79–86.

[112] A. Sutka, G. Mezinskis, Sol–gel auto-combustion synthesis of spinel-type ferrite nanomaterials. Front. Mater. Sci. 6 (2012) 128–141.

[113] A.B. Salunkhe, V.M. Khot, M.R. Phadatare, S.H. Pawar, Combustion synthesis of cobalt ferrite nanoparticles—Influence of fuel to oxidizer ratio. J. Alloys Compd. 514 (2012) 91–96.

[114] U. Kurtan, R. Topkaya, A. Baykal, M.S. Toprak, Temperature dependent magnetic properties of $CoFe_2O_4$/CTAB nanocomposite synthesized by sol–gel auto-combustion technique. Ceram. Int. 39 (2013) 6551–6558.

[115] B.G. Toksha, S.E. Shirsath, S.M. Patange, K.M. Jadhav, Structural investigations and magnetic properties of cobalt ferrite nanoparticles prepared by sol–gel auto combustion method. Solid State Commun. 147 (2008) 479–483.

[116] K. Maaz, A. Mumtaz, S.K. Hasanaina, A. Ceylan, Synthesis and magnetic properties of cobalt ferrite ($CoFe_2O_4$) nanoparticles prepared by wet chemical route. J. Magn. Magn. Mater. 308 (2007) 289–295.

[117] Z. Karimi, L. Karimi, H. Shokrollahi, Nano-magnetic particles used in biomedicine: Core and coating materials. Mater. Sci. Eng. C 33 (2013) 2465–2475.

[118] I. Sharifi, Shokrollahi H., Amiri S. Ferrite-based magnetic nanofluids used in hyperthermia applications. J. Magn. Magn. Mater. 324 (2012) 903–915.

[119] S.P. Rwei, L.Y. Wang, P.W. Yang, Synthesis and magnetorheology study of iron oxide and iron cobalt oxide suspensions. J. Nanomater. (2013) 612894.

[120] K.K. Mohaideen, P.A. Joy, High magnetostriction and coupling coefficient for sintered cobalt ferrite derived from superparamagnetic nanoparticles. Appl. Phys. Lett. 101 (2012) 072405.

[121] S.D. Bhame, P.A. Joy, Effect of sintering conditions and microstructure on the magnetostrictive properties of cobalt ferrite. J. Am. Ceram. Soc. 91 (2008) 1976–1980.

[122] I.C. Nlebedim, J.E. Snyder, A.J. Moses, D.C. Jiles, Dependence of the magnetic and magnetoelastic properties of cobalt ferrite on processing parameters. J. Magn. Magn. Mater. 322 (2010) 3938–3942.

[123] G.Y. Kim, J.H. Jeon, M.H. Kim, D. Suvorov, S.Y. Choi, Microstructural development of cobalt ferrite ceramics and its influence on magnetic properties. Met. Mater. Int. 19 (2013) 1209–1213.

[124] D. Biswal, B.N. Peeples, C. Peeples, A.K. Pradhan, Tuning of magnetic properties in cobalt ferrite by varying Fe^{+2} and Co^{+2} molar ratios. J. Magn. Magn. Mater. 345 (2013) 1–6.

[125] M. Sajjia, M. Oubaha, M. Hasanuzzaman, A.G. Olabi, Developments of cobalt ferrite nanoparticles prepared by the sol-gel process. Ceram. Int. 40 (2014) 1147–1154.

[126] S.B. Waje, M. Hashim, W.D.W. Yusoff, Z. Abbas, X-ray diffraction studies on crystallite size evolution of $CoFe_2O_4$ nanoparticles prepared using mechanical alloying and sintering. Appl. Surf. Sci. 256 (2010) 3122–3127.

[127] K.K. Mohaideen, P.A. Joy, Studies on the effect of sintering conditions on the magnetostriction characteristics of cobalt ferrite derived from nanocrystalline powders. J. Eur. Ceram. Soc. 34 (2014) 677–686.

[128] S.D. Bhame, P.A. Joy, Enhanced magnetostrictive properties of $CoFe_2O_4$ synthesized by an autocombustion method. Sens. Actuators A 137 (2007) 256–261.

[129] A. Rafferty, T. Prescott, D. Brabazon, Sintering behaviour of cobalt ferrite ceramic. Ceram. Int. 34 (2008) 15–21.

[130] I.C. Nlebedim, N. Ranvah, P.I. Williams, Y. Melikhov, F. Anayi, J.E. Snyder, A.J. Moses, D.C. Jiles, Influence of vacuum sintering on microstructure and magnetic properties of magnetostrictive cobalt ferrite. J. Magn. Magn. Mater. 321 (2009) 2528–2532.

[131] M.P.G. Sandoval, A.M. Beesley, M.M. Yoshida, L.F. Cobas, J.A.M. Aquino, Comparative study of the microstructural and magnetic properties of spinel ferrites obtained by co-precipitation. J. Alloys Compd. 369 (2004) 190–194.

[132] F. Huixia, C. Baiyi, Z. Deyi, Z. Jianqiang, T. Lin, Preparation and characterization of the cobalt ferrite nano-particles by reverse coprecipitation. J. Magn. Magn. Mater. 356 (2014) 68–72.

[133] Y. Qu, H. Yang, N. Yang, Y. Fan, H. Zhu, G. Zou, The effect of reaction temperature on the particle size, structure and magnetic properties of coprecipitated $CoFe_2O_4$ nanoparticles. Mater. Lett. 60 (2006) 3548–3552.

[134] R.W. McCallum, K.W. Dennis, D.C. Jiles, J.E. Snyder, Y.H. Chen, Composite magnetostrictive materials for advanced automotive magnetomechanical sensors. Low Temp. Phys. 27 (2001) 266–274.

[135] Y. Ghen, J.E. Snyder, C.R. Schwichtenberg, K.W. Dennis, R.W. McCallum, D.C. Jiles, Metal-bonded Co-Ferrite Composites for Magnetostrictive Torque Sensor Applications. IEEE Trans. Magn. 35 (1999) 3652–3654.

[136] N. Stepova, O. Kushka, Colloid removal from aqua media via magnetite-based reagent. Chem. Chem. Technol. 5 (2011) 155–160.

[137] T.E. Babutina, N.V. Boshitska, O.A. Ivashchenko, A.O. Perekosn, V.Z. Voinash, I.V. Uvarova, Nanosized iron and iron oxide powders promising for medicine. Powder Metall. Met. Ceram. 48 (2009) 365–370.

[138] L. Vékás, Ferrofluids and magnetorheological fluids. Adv. Sci. Tech. 54 (2008) 127–136.

[139] S. Asuha, B. Suyala, S. Zhao, Porous structure and Cr(VI) removal abilities of Fe_3O_4 prepared from Fe-urea complex. Mater. Chem. Phys. 129 (2011) 483–487.

[140] J.T. Mayo, C.Yavuz, S. Yean, L. Cong, H. Shipley, W. Yu, J. Falkner, A. Kan, M. Tomson, V.L. Colvin, The effect of nanocrystalline magnetite size on arsenic removal. Sci. Technol. Adv. Mater. 8 (2007) 71–75.

[141] T.K. Indira, P.K. Lakshmi, Magnetic nanoparticles – a review. Int. J. Pharm. Sci. Nanotech. 3 (2010) 1035–1042.

[142] J.C. Aphesteguy, S.E. Jacobo, N.N. Schegoleva, G.V. Kurlyandskaya, New route for preparation and characterization of magnetite nanoparticles. Arabian J. Chem., 4 (2011) 235–237.

[143] S. Wu, A. Sun, F. Zhai, J. Wang, W. Xu, Q. Zhang, A.A. Volinsky, Fe_3O_4 magnetic nanoparticles synthesis from tailings by ultrasonic chemical co-precipitation. Mater. Lett. 65 (2011) 1882–1884.

[144] J.C. Aphesteguy, S.E. Jacobo, N.N. Schegoleva, G.V. Kurlyandskaya, Characterization of nanosized spinel ferrite powders synthesized by coprecipitation and autocombustion method. J. Alloys Compd. 495 (2010) 509–512.

[145] I. Negkov, T. Merodiiska, L. Slavov, R.E. Vandenberghe, Y. Kusano, J. Takada, Surface oxidation, size and shape of nano-sized magnetite obtained by co-precipitation. J. Magn. Magn. Mater. 300 (2006) 358–367.

[146] J. Xu, H. Yang, W. Fu, K. Du, Y. Sui, J. Chen, Y. Zeng, M. Li, G. Zou, Preparation and magnetic properties of magnetite nanoparticles by sol-gel method. J. Magn. Magn. Mater. 309 (2007) 307–311.

[147] S. Liu, F. Lu, R. Xing, J. Zhu, Structural effects of Fe_3O_4 nanocrystals on peroxidase-like activity. Chem. Eur. J. 17 (2011) 620–625.

[148] S. Asuha, B. Suyala, X. Siqintana, S. Zhao, Direct synthesis of Fe_3O_4 nanopowder by thermal decomposition of Fe-urea complex and its properties. J. Alloys Compd. 509 (2011) 2870–2873.

[149] J. Topfer, A. Angermann, Nanocrystalline magnetite and Mn-Zn ferrite particles via the polyol process: synthesis and magnetic properties. Mater. Chem. Phys. 129 (2011) 337–342.

[150] L. Chen, Z. Lin, C. Zhao, Y. Zheng, Y. Zhou, H. Peng, Direct synthesis and characterization of mesoporous Fe_3O_4 through pyrolysis of ferric nitrate-ethylene glycol gel. J. Alloys Compd. 509 (2011) L1–L5.

[151] X. Liu, Y. Guo, Y. Wang, J. Ren, Y. Wang, Y. Guo, Y. Guo, G. Lu, Y. Wang, Z. Zhang, Direct synthesis of mesoporous Fe_3O_4 through citric acid-assisted solid thermal decomposition. J. Mater. Sci. 45 (2010) 906–910.

[152] R. Strobel, S.E. Pratsinis, Direct synthesis of maghemite, magnetite and wustite nanoparticles by flame spray pyrolysis. Adv. Powder Technol. 20 (2009) 190–194.

[153] P. Hu, S. Zhang, H. Wang, D. Pan, J. Tian, Z. Tang, A.A. Volinsky, Heat treatment effects on Fe_3O_4 nanoparticles structure and magnetic properties prepared by carbothermal reduction. J. Alloys Compd. 509 (2011) 2316–2319.

[154] A.S. Mukasyan, P. Dinka, Novel approaches to solution-combustion synthesis of nanomaterials. Int. J. Self Propag. High Temp. Synth. 16 (2007) 23–35.

[155] J. Toniolo, A.S. Takimi, M.J. Andrade, R. Bonadiman, C.P. Bergmann, Synthesis by the solution combustion process and magnetic properties of iron oxide (Fe_3O_4 and α-Fe_2O_3) particles. J. Mater. Sci. 42 (2007) 4785–4791.

[156] K. Deshpande, M. Nersesyan, A. Mukasyan, A. Varma, Novel ferromagnetic iron oxide nanopowders. Ind. Eng. Chem. Res. 44 (2005) 6196–6199.

[157] K. Wieczorek-Ciurowa, A.J. Kozak, The thermal decomposition of $Fe(NO_3)_3 \cdot 9H_2O$. J. Therm. Anal. Calorim. 58 (1999) 647–651.

[158] J.P. Sandaers, P.K. Gallagher, Kinetics of the oxidation of magnetite using simultaneous TG/DSC. J. Therm. Anal. Calorim. 72 (2003) 777–789.

[159] M. Descostes, F. Mercier, N. Thromat, C. Beaucaire, M. Gautier-Soyer, Use of XPS in the determination of chemical environment and oxidation state of iron and sulfur samples: constitution of a data basis in binding energies for Fe and S reference compounds and applications to the evidence of surface species of an oxidized pyrite in a carbonate medium. Appl. Surf. Sci. 165 (2000) 288–302.

[160] G. Bhargava, I. Gouzman, C.M. Chun, T.A. Ramanarayanan, S.L. Bernasek, Characterization of the native surface thin film on pure polycrystalline iron: A high resolution XPS and TEM study. Appl. Surf. Sci. 253 (2007) 4322–4329.

[161] V. Păunescu, F.M. Bojin, O.I. Gavriliuc, E.A. Tăculescu, **R. Ianoş**, V.L. Ordodi, V.F. Iman, C.A. Tatu, Enucleation: A possible mechanism of cancer cell death. J. Cell. Mol. Med. 18 (2014) 962–965.

[162] G. Mihoc, **R. Ianoş**, C. Păcurariu, I. Lazău, Combustion synthesis of some iron oxides used as adsorbents for phenol and p-chlorophenol removal from wastewater. J. Therm. Anal. Calorim. 112 (2013) 391–397.

[163] C. Păcurariu, G. Mihoc, A. Popa, S.G. Muntean, **R. Ianoş**, Adsorption of phenol and p-chlorophenol from aqueous solutions on poly (styrene-co-divinylbenzene) functionalized materials. Chem. Eng. J. 222 (2013) 218–227.

[164] G. Mihoc, **R. Ianoş**, C. Păcurariu, Adsorption of phenol and p-chlorophenol from aqueous solutions by magnetic nanopowder. Water Sci. Technol. 69 (2014) 385–391.

[165] O. Paşka, **R. Ianoş**, C. Păcurariu, A. Brădeanu, Magnetic nanopowder as effective adsorbent for the removal of Congo Red from aqueous solution. Water Sci. Technol. 69 (2014) 1234–1240.

[166] M. Megharaj, B. Ramakrishnan, K. Venkateswarlu, N. Sethunathan, R. Naidu, Bioremediation approaches for organic pollutants: A critical perspective. Environ. Int. 37 (2011) 1362–1375.

[167] I. Ali, M. Asim, T.A. Khan, Low cost adsorbents for the removal of organic pollutants from wastewater. J. Environ. Manage. 113 (2012) 170–183.

[168] I. Oller, S. Malato, J.A. Sánchez-Pérez, Combination of Advanced Oxidation Processes and biological treatments for wastewater decontamination—A review. Sci. Total Environ. 409 (2011) 4141–4166.

[169] A.K. Verma, R.R. Dash, P. Bhunia, A review on chemical coagulation/flocculation technologies for removal of color from textile wastewaters. J. Environ. Manage. 93 (2012) 154–168.

[170] H. Kusic, N. Koprivanac, A.L. Bozic, Environmental aspects on the photodegradation of reactive triazine dyes in aqueous media. J. Photochem. Photobiol. A 252 (2013) 131–144.

[171] J.H. Al-Rifai, H. Khabbaz, A.I. Schäfer, Removal of pharmaceuticals and endocrine disrupting compounds in a water recycling process using reverse osmosis systems. Separ. Purif. Technol. 77 (2011) 60–67.

[172] W. Park, E. Jang, M.J. Lee, S. Yu, T.H. Kim, Combination of ion exchange system and biological reactors for simultaneous removal of ammonia and organics. J. Environ. Manage. 92 (2011) 1148-1153.

[173] G. Muthuraman, T.T. Teng, C.P. Leh, I. Norli, Extraction and recovery of methylene blue from industrial wastewater using benzoic acid as an extractant. J. Hazard. Mater. 163 (2009) 363–369.

[174] J. Huang, X. Jin, S. Deng, Phenol adsorption on an N-methylacetamide-modified hypercrosslinked resin from aqueous solutions. Chem. Eng. J. 192 (2012) 192–200.

[175] N.A. Khan, Z. Hasan, S.H. Jhung, Adsorptive removal of hazardous materials using metal-organic frameworks (MOFs): A review. J. Hazard. Mater. 244–245 (2013) 444–456.

[176] M.L. Soto, A. Moure, H. Domínguez, J.C. Parajó, Recovery, concentration and purification of phenolic compounds by adsorption: A review. J. Food. Eng. 105 (2011) 1–27.

[177] A. Bhatnagar, A.K. Minocha, Conventional and non-conventional adsorbents for removal of pollutants from water – A review. Indian J. Chem. Techn. 13 (2006) 203–217.

[178] C. Moreno-Castilla, Adsorption of organic molecules from aqueous solutions on carbon materials. Carbon 42 (2004) 83–94.

[179] L. Damjanović, V. Rakić, V. Rac, D. Stošić, A. Auroux, The investigation of phenol removal from aqueous solutions by zeolites as solid adsorbents. J. Hazard. Mater. 184 (2010) 477–484.

[180] T. Undabeytia, S. Nir, T. Sánchez-Verdejo, J. Villaverde, C. Maqueda, E. Morillo, A clay–vesicle system for water purification from organic pollutants. Water. Res. 42 (2008) 1211–1219.

[181] G. Qin, Y. Yao, W. Wei, T. Zhang, Preparation of hydrophobic granular silica aerogels and adsorption of phenol from water. Appl. Surf. Sci. 280 (2013) 806–811.

[182] V.V. Panic, Z.P. Madzarevic, T. Volkov-Husovic, S.J. Velickovic, Poly(methacrylic acid) based hydrogel as sorbents for removal of cationic dye basic yellow 28: Kinetics, equilibrium study and image analysis. Chem. Eng. J. 217 (2013) 192–204.

[183] H. Sun, L. Cao, L. Lu, Magnetite/Reduced Graphene Oxide Nanocomposites: One Step Solvothermal Synthesis and Use as a Novel Platform for Removal of Dye Pollutants. Nano. Res. 4 (2011) 550–562.

[184] S.C.N. Tang, I.M.C. Lo, Magnetic nanoparticles: Essential factors for sustainable environmental applications. Water Res. 47 (2013) 2613–2632.

[185] P. Xu, G.M. Zeng, D.L. Huang, C.L. Feng, S. Hu, M.H. Zhao, C. Lai, Z. Wei, C. Huang, D.X. Xie, Z.F. Liu, Use of iron oxide nanomaterials in wastewater treatment: A review. Sci. Total Environ. 424 (2012) 1–10.

[186] A.B. Cundy, L. Hopkinson, R.L.D. Whitby, Use of iron-based technologies in contaminated land and groundwater remediation: A review. Sci. Total Environ. 400 (2008) 42–51.

[187] R.D. Ambashta, M. Sillanpää, Water purification using magnetic assistance: A review. J. Hazard. Mater. 180 (2010) 38–49.

[188] J.L. Gong, B. Wang, G.M. Zeng, C.P. Yang, C.G. Niu, Q.Y. Niu, W.J. Zhou, Y. Liang, Removal of cationic dyes from aqueous solution using magnetic multi-wall carbon nanotube nanocomposite as adsorbent. J. Hazard. Mater. 164 (2009) 1517–1522.

[189] L. Ai, C. Zhang, F. Liao, Y. Wang, M. Li, L. Meng, J. Jiang, Removal of methylene blue from aqueous solution with magnetite loaded multi-wall carbon nanotube: Kinetic, isotherm and mechanism analysis. J. Hazard. Mater. 198 (2011) 282–290.

[190] L. Fan, C. Luo, X. Li, F. Lu, H. Qiu, M. Sun, Fabrication of novel magnetic chitosan grafted with graphene oxide to enhance adsorption properties for methyl blue. J. Hazard. Mater. 215–216 (2012) 272–279.

[191] J. Qiu, Q. Li, Z. Wang, Y. Sun, H. Zhang, CVD synthesis of coal-gas-derived carbon nanotubes and nanocapsules containing magnetic iron carbide and oxide. Carbon 44 (2006) 2565–2568.

[192] B. Xu, J. Guo, X. Wang, X. Liu, H. Ichinose, Synthesis of carbon nanocapsules containing Fe, Ni or Co by arc discharge in aqueous solution. Carbon 44 (2006) 2631–2634.

[193] M. Bystrzejewski, K. Pyrzyńska, A. Huczko, H. Lange, Carbon-encapsulated magnetic nanoparticles as separable and mobile sorbents of heavy metal ions from aqueous solutions. Carbon 47 (2009) 1189–1206.

[194] Y. Lu, Z. Zhu,Z. Liu, Carbon-encapsulated Fe nanoparticles from detonation-induced pyrolysis of ferrocene. Carbon 43 (2005) 369–374.

[195] L. Ai, C. Zhang, Z. Chen, Removal of methylene blue from aqueous solution by a solvothermal-synthesized graphene/magnetite composite. J. Hazard. Mater. 192 (2011) 1515–1524.

[196] S. Bai, X. Shen, X. Zhong, Y. Liu, G. Zhu, X. Xu, K. Chen, One-pot solvothermal preparation of magnetic reduced graphene oxide-ferrite hybrids for organic dye removal. Carbon 50 (2012) 2337–2346.

[197] A.S. Mukasyan, P. Epstein, P. Dinka, Solution combustion synthesis of nanomaterials. P. Combust. Inst. 31 (2007) 1789–1795.

[198] P. Dinka, A.S. Mukasyan, In Situ Preparation of the Supported Catalysts by Solution Combustion Synthesis. J. Phys. Chem., 109 (2005), 21627–21633.

[199] S.L. González-Cortés, F.E. Imbert, Fundamentals, properties and applications of solid catalysts prepared by solution combustion synthesis (SCS). Appl. Catal. A-Gen. 452 (2013) 117–131.

[200] H.C. Liese, Mineralogical notes. An infrared absorption analysis of magnetite. Am. Mineral. 52 (1967) 1198–1205.

[201] T. Theophanides, Infrared spectroscopy – Materials science, engineering and technology. In Tech, Rijeka, 2012.

[202] N. Du, Y. Xu, H. Zhang, C. Zhai, D. Yang, Selective Synthesis of Fe_2O_3 and Fe_3O_4 Nanowires Via a Single Precursor: A General Method for Metal Oxide Nanowires. Nanoscale Res. Lett. 5 (2010) 1295–1300.

[203] T. Ru-Ling, W. Keng-Tung, W. Feng-Chin, J. Ruey-Shin, Kinetic studies on the adsorption of phenol, 4-chlorophenol, and 2,4-dichlorophenol from water using activated carbons. J. Environ. Manage. 91 (2010) 2208–2214.

[204] O. Hamdaoui, E. Naffrechoux, Modeling of adsorption isotherms of phenol and chlorophenols onto granular activated carbon Part I. Two-parameter models and equations allowing determination of thermodynamic parameters. J. Hazard. Mater. 147 (2007) 381–394.

[205] O. Hamdaoui, E. Naffrechoux, Modeling of adsorption isotherms of phenol and chlorophenols onto granular activated carbon Part II. Models with more than two parameters. J. Hazard. Mater. 147 (2007) 401–411.

[206] A. Dabrowski, P. Podkoscielny, Z. Hubicki, M. Barczak, Adsorption of phenolic compounds by activated carbon – a critical review. Chemosphere 58 (2005) 1049–1070.

[207] M.W. Jung, K.H. Ahn, Y. Lee, K.P. Kim, J.S. Rhee, J.T. Park, K. Paeng, Adsorption characteristics of phenol and chlorophenols on granular activated carbons(GAC). Microchem. J. 70 (2001) 123–131.

[208] M.A. Lephoto, O.M. Ntwaeaborwa, S.S. Pitale, H.C. Swart, J.R. Botha, B.M. Mothudi, Synthesis and characterization of $BaAl_2O_4$:Eu^{2+} co-doped with different rare earth ions. Physica B 407 (2012) 1603–1606.

[209] F.B. Dejene, M.A. Kebede, M. Redi-Abshiro, B.V. Kgarebe, Structural and photoluminescence properties of Dy^{3+} co-doped and Eu^{2+} activated MAl_2O_4 (M = Ba,Ca, Sr) nanophosphors. Opt. Mater. 35 (2013) 1927–1931.

[210] Z. Qiu, Y. Zhou, M. Lu, A. Zhang, Q. Ma, Combustion synthesis of long-persistent luminescent MAl_2O_4: Eu^{2+}, R^{3+} (M = Sr, Ba, Ca, R = Dy, Nd and La) nanoparticles and luminescence mechanism research. Acta Mater. 55 (2007) 2615–2620.

[211] J.S. Kim, P.E. Jeon, J.C. Choi, H.L. Park, S.I. Mho, G.C. Kim, Warm-white-light emitting diode utilizing a single-phase full-color $Ba_3MgSi_2O_8$: Eu^{2+}, Mn^{2+} phosphor. Appl. Phys. Lett. 84 (2004) 2931–2933.

[212] C.-N. Xu, X.-G. Zheng, M. Akiyama, K. Nonaka, T. Watanabe, Dynamic visualization of stress distribution by mechanoluminescence image. Appl. Phys. Lett. 76 (2000) 179–181.

[213] K. Van den Eeckhout, P.F. Smet, D. Peelman, Persistent luminescence in Eu^{2+}-doped compounds: a review. Materials 3 (2010) 2536–2566.

[214] R. Stefani, L.C.V. Rodrigues, C.A.A. Carvalho, M.C.F.C. Felinto, H.F. Brito, M. Lastusaari, J. Hölsä, Persistent luminescence of Eu^{2+} and Dy^{3+} doped barium aluminate $(BaAl_2O_4$:Eu^{2+},$Dy^{3+})$ materials. Opt. Mater. 31 (2009) 1815–1818.

[215] H.-S. Roh, I.-S. Cho, J.-S. An, C.M. Cho, T.H. Noh, D.K. Yim, D.-W. Kim, K.S. Hong, Enhanced photoluminescence property of Dy^{3+} co-doped $BaAl_2O_4$:Eu^{2+} green phosphors. Ceram. Int. 38 (2012) 443–447.

[216] J. Zhang, Q. Xiao, Y. Liu, Synthesis and characterization of needle-like $BaAl_2O_4$:Eu,Dy phosphor via hydrothermal-homogeneous precipitation method. J. Rare Earths 31 (2013) 342–346.

[217] D.-S. Xing, M.-L. Gong, X.-Q. Qiu, D.-J. Yang, K.-W. Cheah, A bluish green barium aluminate phosphor for PDP application. Mater. Lett. 60 (2006) 3217–3220.

[218] L.M. Annah, Luminescent properties of combustion synthesized $BaAl_2O_4$:Eu^{2+} and $(Ba_{1-x}Sr_x)Al_2O_4$:Eu^{2+} phosphors co-doped with different rare earth ions – PhD thesis. University of the Free State, South Africa, 2011.

[219] V. Singh, V. Natarajan, J.-J. Zhu, Studies on Eu doped Ba and Zn aluminate phosphors prepared by combustion synthesis. Opt. Mater. 29 (2007) 1447–1451.

[220] H.F. Brito, M.C.F.C. Felinto, J. Hölsä, T. Laamanen, M. Lastusaari, M. Malkamäki, P. Novák, L.C.V. Rodrigues, R. Stefani, DFT and synchrotron radiation study of Eu^{2+} doped $BaAl_2O_4$, Optical Materials Express 2 (2012) 420–431.

[221] B.M. Mothudi, O.M. Ntwaeaborwa, J.R. Botha, H.C. Swart, Photoluminescence and phosphorescence properties of $MAl_2O_4:Eu^{2+}$, Dy^{3+} (M=Ca, Ba, Sr) phosphors prepared at an initiating combustion temperature of 500 °C. Physica B 404 (2009) 4440–4444.

[222] L.C.V. Rodriguez, R. Stefani, H.F. Brito, M.C.F.C. Felinto, J. Hölöä, M. Lastusaari, T. Laamanen, M. Malkamäki, Thermoluminescence and synchrotron radiation studies on the persistent luminescence of $BaAl_2O_4:Eu^{2+},Dy^{3+}$. J. Solid State Chem. 183 (2010) 2365–2371.

[223] **R. Ianoş**, R. Lazău, R. Băbuţă, S. Borcănescu, C.R. Boruntea, Nanocrystalline $BaAl_2O_4$ powders prepared by aqueous combustion synthesis. Ceram. Int. 39 (2013) 2645–2650.

[224] F. Sun, J. Zhao, Blue-green $BaAl_2O_4:Eu^{2+},Dy^{3+}$ phosphors synthesized via combustion synthesis method assisted by microwave irradiation. J. Rare Earths 29 (2011) 326–329.

[225] M. Peng, G. Hong, Reduction from Eu^{3+} to Eu^{2+} in $BaAl_2O_4:Eu$ phosphor prepared in an oxidizing atmosphere and luminescent properties of $BaAl_2O_4:Eu$. J. Lumin. 127 (2007) 735–740.

[226] L. Zhang, L. Wang, Y. Zhu, Synthesis and performance of $BaAl_2O_4$ with a wide spectral range of optical absorption. Adv. Funct. Mater. 17 (2007) 3781–3790.

[227] F. Clabau, X. Rocquefelte, S. Jobic, P. Deniard, M.-H. Whangbo, A. Garcia, T. Le Mercier, On the phosphorescence mechanism in $SrAl_2O_4:Eu^{2+}$ and its codoped derivatives. Solid State Sci. 9 (2007) 608–612.

[228] X. Li, Z. Zhua, Q. Zhaoa, L. Wang, Photocatalytic degradation of gaseous toluene over $ZnAl_2O_4$ prepared by different methods: A comparative study. J. Hazard. Mater. 186 (2011) 2089–2096.

[229] X. Duan, D. Yuan, Z. Sun, C. Luan, D. Pan, D. Xu, M. Lv, Preparation of Co^{2+}-doped $ZnAl_2O_4$ nanoparticles by citrate sol–gel method. J. Alloy. Compd. 386 (2005) 311–314.

[230] D. Visinescu, B. Jurca, A. Ianculescu, O. Carp, Starch – A suitable fuel in new low-temperature combustion-based synthesis of zinc aluminate oxides. Polyhedron 30 (2011) 2824–2831.

[231] K.M.S. Viana, B.B. Dantas, N.A.S. Nogueira, J.M. Carp, N.L. Freitas, R.H.G.A. Kiminami, A.C.F.M. Costa, Influence of Fuel in the Synthesis of $ZnAl_2O_4$ Catalytic Supports by Combustion Reaction. Mater. Sci. Forum 660-661 (2010) 52–57.

[232] Y. Wu, X. Wang, Preparation and characterization of single-phase $α-Fe_2O_3$ nano-powders by Pechini sol–gel method. Mater. Lett. 65 (2011) 2062–2065.

[233] D. Silva, A. Abreu, M.R. Davolos, M. Rosaly, Determination of the local site occupancy of Eu^{3+} ions in $ZnAl_2O_4$ nanocrystalline powders. Opt. Mater. 33 (2011) 1226–1233.

[234] F. Davar, M. Salavati-Niasari, Synthesis and characterization of spinel-type zinc aluminate nanoparticles by a modified sol–gel method using new precursor. J. Alloy. Compd. 509 (2011) 2487–2492.

[235] S. Kurajica, E. Tkalcec, J. Sipusic, G. Matijasic, I. Brnardic, I. Simcic, Synthesis and characterization of nanocrystalline zinc aluminate spinel by sol–gel technique using modified alkoxide precursor. J. Sol-Gel Sci. Technol. 46 (2008) 152–160.

[236] A.A. Da Silva, G.A. de Souza, M.R. Davolos, Characterization of nanosized $ZnAl_2O_4$ spinel synthesized by the sol–gel method. J. Sol-Gel Sci. Technol. 49 (2009) 101–105.

[237] W. Xiuhua, C. Donghua, Synthesis and characterization of nanosized zinc aluminate spinel by sol–gel technique. Mater. Lett. 60 (2006) 823–827.

[238] A.K. Nikumbh, P.V. Adhyapak, Synthesis, properties and optimization of the rheological behaviors on alumina and zinc aluminate powders obtained from dicarboxylate precursors. Powder Technol. 202 (2010) 14–23.

[239] R.N. Das, A. Bandyopadhyay, S. Bose, Nanocrystalline α-Al$_2$O$_3$ Using Sucrose. J. Am. Ceram. Soc. 84 (2001) 2421–2423.

[240] R. Mikutta, M. Kleber, K. Kaiser, R. Jahn, Organic Matter Removal from Soils using Hydrogen Peroxide, Sodium Hypochlorite, and Disodium Peroxodisulfate. Soil Sci. Soc. Am. J. 69 (2005) 120–135.

[241] L.L. Bissey, J.L. Smith, R.J. Watts, Soil organic matter–hydrogen peroxide dynamics in the treatment of contaminated soils and groundwater using catalyzed H$_2$O$_2$ propagations (modified Fenton's reagent). Water Res. 40 (2006) 2477–2484.

[242] S. Laurent, D. Forge, M. Port, A. Roch, C. Robic, L.V. Elst, R.N. Muller, Magnetic iron oxide nanoparticles: Synthesis, stabilization, vectorization, physicochemical characterizations, and biological applications. Chem. Rev. 108 (2008) 2064–2110.

[243] M.D. Carvalho, F. Henriques, L.P. Ferreira, M. Godinho, M.M. Cruz, Iron oxide nanoparticles: the Influence of synthesis method and size on composition and magnetic properties. J. Solid State Chem. 201 (2013) 144–152.

[244] S.C.N. Tang, I M.C. Lo, Magnetic nanoparticles: Essential factors for sustainable environmental applications. Water Res. 47 (2013) 2613–2632.

[245] L.A. Mercante, W.W.M. Melo, M. Granada, H.E. Troiani, W.A.A. Macedo, J.D. Ardison, M.G.F. Vaz, M.A. Novak, Magnetic properties of nanoscale crystalline maghemite obtained by a new synthetic route. J. Magn. Magn. Mater. 324 (2012) 3029–3033.

[246] A. Millan, A. Urtizberea, N. J. O. Silva, F. Palacio, V. S. Amaral, E. Snoeck, V. Serin, Surface effects in maghemite nanoparticles. J. Magn. Magn. Mater. 312 (2007) L5–L9.

[247] E. Darezereshki, M. Ranjbar, F. Bakhtiari, One-step synthesis of maghemite (γ-Fe$_2$O$_3$) nano-particles by wet chemical method. J. Alloys Compd. 502 (2010) 257–260.

[248] U. Jeong, X. Teng, Y. Wang, H. Yang, Y. Xia, Superparamagnetic colloids: Controlled synthesis and niche applications. Adv. Mater. 19 (2007) 33–60.

[249] M.T.A. Elói, R.B. Azevedo, E.C.D. Lima, A.C.M. Pimenta, P.C. Morais, Birefringence and transmission electron microscopy of maghemite-based biocompatible magnetic fluids. J. Magn. Magn. Mater. 289 (2005) 168–170.

[250] A. Dyal, K. Loos, M. Noto, S.W. Chang, C. Spagnoli, K.V.P.M. Shafi, A. Ulman, M. Cowman, R.A. Gross, Activity of candida rugosa lipase immobilized on gamma-Fe$_2$O$_3$ magnetic nanoparticles. J. Am. Chem. Soc. 125 (2003) 1684–1685.

[251] S. He, Y. Feng, N. Gu, Y. Zhang, X. Lin, The effect of γ-Fe$_2$O$_3$ nanoparticles on Escherichia coli genome. Environ. Pollut. 159 (2011) 3468–3473.

[252] Y.H. Chen, Thermal properties of nanocrystalline goethite, magnetite, and maghemite. J. Alloys Compd. 553 (2013) 194–198.

[253] C. Păcurariu, E.A. Tăculescu (Moacă), **R. Ianoş**, O. Marinică, C.V. Mihali, V. Solociuc, Synthesis and characterization of γ-Fe$_2$O$_3$/SiO$_2$ composites as possible candidate for magnetic paper manufacture. Ceram. Int. 41 (2015) 1079–1085.

[254] K. Rudzka, J.L. Viotab, J.A. Muñoz-Gamez, A. Carazo, A. Ruiz-Extremera, Á.V. Delgado, Nanoengineering of doxorubicin delivery systems with functionalized maghemite nanoparticles. Colloids Surf. B. 111 (2013) 88– 96.

[255] K. Kluchova, R. Zboril, J. Tucek, M. Pecova, L. Zajoncova, I. Safarik, M. Mashlan, I. Markova, D. Jancik, M. Sebela, H. Bartonkova, V. Bellesi, P. Novak, D. Petridis, Superparamagnetic maghemite nanoparticles from solid-state synthesis − Their functionalization towards peroral MRI contrast agent and magnetic carrier for trypsin immobilization. Biomaterials 30 (2009) 2855–2863.

[256] P. Moroz, H. Pardoe, S.K. Jones, T.G.S. Pierre, S. Song, B.N. Gray, Arterial embolization hyperthermia: hepatic iron particle distribution and its potential determination by magnetic resonance imaging. Phys. Med. Biol. 47 (2002) 1591–1602.

[257] D. Baratella, M. Magro, G. Sinigaglia, R. Zboril, G. Salviulo, F. Vianello, A glucose biosensor based on surface active maghemite nanoparticles. Biosens. Bioelectron. 45 (2013) 13–18.

[258] A.K. Gupta, S. Wells, Surface-modified superparamagnetic nanoparticles for drug delivery: Preparation, characterization, and cytotoxicity studies. IEEE Trans. Nanobioscience 3 (2004) 66–73.

[259] S. Lin, D. Lu, Z. Liu, Removal of arsenic contaminants with magnetic γ-Fe$_2$O$_3$ nanoparticles. Chem. Eng. J. 211-212 (2012) 46–52.

[260] W. Jiang, M. Pelaez, D.D. Dionysiou, M.H. Entezari, D. Tsoutsou, K. O'Shea, Chromium(VI) removal by maghemite nanoparticles. Chem. Eng. J. 222 (2013) 527–533.

[261] A. Afkhami, M. Saber-Tehrani, H. Bagheri, Modified maghemite nanoparticles as an efficient adsorbent for removing some cationic dyes from aqueous solution. Desalination 263 (2010) 240–248.

[262] S.K. Sahoo, K. Agarwal, A.K. Singh, B.G. Polke, K.C. Raha, Characterization of γ- and α-Fe$_2$O$_3$ nano powders synthesized by emulsion precipitation-calcination route and rheological behaviour of α-Fe$_2$O$_3$. Int. J. Eng. Sci. Techn. 2 (2010) 118–126.

[263] S. Asuha, Y.M. Zhao, S. Zhao, W. Deligeer, Synthesis of mesoporous maghemite with high surface area and its adsorptive properties. Solid State Sci. 14 (2012) 833–839.

[264] Y. Leconte, S. Veintemillas-Verdaguer, M.P. Morales, R. Costo, I. Rodriguez, P. Bonville, B. Bouchet-Fabre, N. Herlin-Boime, Continuous production of water dispersible carbon-iron nanocomposites by laser pyrolysis: Application as MRI contrasts. J. Colloid Interface Sci. 313 (2007) 511–518.

[265] R. Strobel, S.E. Pratsinis, Direct synthesis of maghemite, magnetite and wustite nanoparticles by flame spray pyrolysis. Adv. Powder Technol. 20 (2009) 190–194.

[266] A.D. Abid, M. Kanematsu, T.M. Young, I.M. Kennedy, Arsenic removal from water using flame-synthesized iron oxide nanoparticles with variable oxidation states. Aerosol Sci. Technol. 47 (2013) 169–176.

[267] M.F. Silva, A.A.W. Hechenleitner, D.M.F. de Oliveira, M. Agüeros, R. Peñalva, J.M. Irache, E.A.G. Pineda, Optimization of maghemite-loaded PLGA nanospheres for biomedical applications. Eur. J. Pharm. Sci. 49 (2013) 343–351.

[268] P. Synek, O. Jašek, L. Zajíčková, B. David, V. Kudrle, N. Pizúrová, Plasmachemical synthesis of maghemite nanoparticles in atmospheric pressure microwave torch. Mater. Lett. 65 (2011) 982–984.

[269] K. Deshpande, A. Mukasyan, A. Varma, Direct synthesis of iron oxide nanopowders by the combustion approach: reaction mechanism and properties. Chem. Mater. 16 (2004) 4896–4904.

[270] C. Cannas, A. Ardu, D. Niznansky, D. Peddis, G. Piccaluga, A. Musinu, Simple and fast preparation of pure maghemite nanopowders through sol–gel self-combustion. J. Sol-Gel Sci. Technol. 60 (2011) 266–274.

[271] W. Kim, C.-Y. Suh, S.-W. Cho, K.-M. Roh, H. Kwon, K. Song, I.-J. Shon, A new method for the identification and quantification of magnetite–maghemite mixture using conventional X-ray diffraction technique. Talanta 94 (2012) 348–352.

[272] J. Torrent, V. Barrón, Diffuse reflectance spectroscopy of iron oxides, in: M. Dekker (Ed.), Encyclopedia of Surface and Colloid Science, Taylor & Francis, 2007, pp. 1438–1446.

[273] R.G.J. Strens, B. Wood, Diffuse reflectance spectra and optical properties of some iron and titanium oxides and oxyhydroxides. Mineral. Mag. 43 (1979) 347–354.

[274] D.M. Sherman, T.D. Waite, Electronic spectra of Fe^{3+} oxides and oxide hydroxides in the near IR to near UV. Am. Mineral. 70 (1985) 1262–1269.

[275] A.C. Scheinost, A. Chavernas, V. Barron, Torrent, Use and limitations of second-derivative diffuse reflectance spectroscopy in the visible to near-infrared range to identify and quantify Fe oxide minerals in soils. Clay. Clay Miner. 46 (1998) 528–536.

[276] M. Aliahmad, N.N. Moghaddam, Synthesis of maghemite (γ-Fe_2O_3) nanoparticles by thermal-decomposition of magnetite (Fe_3O_4) nanoparticles. Mater. Sci. Poland 31 (2013) 264–268.